Advancing Surface Plasmon Resonance Imaging Sensors through Neural Network-Aided Analysis of Lateral Signal Modulation for Robust Surface Sensing

Dissertation

zur Erlangung des Doktorgrades der Naturwissenschaften
(Dr. rer. nat.)
der Fakultät für Chemie und Pharmazie
der Universität Regensburg

vorgelegt von
Simon Jobst
aus Regensburg
im Jahr 2025

Die vorgelegte Dissertation entstand in der Zeit von Oktober 2018 bis März 2025 in Kooperation des Instituts für Analytische Chemie, Chemo- und Biosensorik der naturwissenschaftlichen Fakultät IV - Chemie und Pharmazie - der Universität Regensburg (UR)

und

des Sensorik-Applikationszentrums (SappZ) der Ostbayerischen Technischen Hochschule (OTH) Regensburg.

Die Arbeit wurde angeleitet von: Privatdozent Dr. Thomas Hirsch
Professor Dr. Rudolf Bierl

Das Promotionsgesuch wurde eingereicht am: 26.03.2025
Termin des Kolloquiums: 14.05.2025

Vorsitz des Prüfungsausschusses übernimmt Professor Dr. Tepner. Erstgutachter ist Privatdozent Dr. Hirsch, Zweitgutachter Professor Dr. Bierl und Drittprüfer ist Professor Dr. Wegener.

Ich möchte mich bei allen bedanken, die mich auf dem Wege der Promotion unterstützt und begleitet haben. Insbesondere gilt mein Dank Herrn PD Dr. Thomas Hirsch, der jederzeit (sei es sonn- oder feiertags oder spätabends) mit Rat und Tat zur Seite stand. Sowie Herrn Prof. Dr. Rudolf Bierl, ohne dessen Förderung und fachliche Unterstützung diese Arbeit nie entstanden wäre. Danke an die Arbeitsgruppen SPR und Photoakustik, sowie meinen Inselbewohner:innen, Korrektor:innen und Freundinnen und Freunden im SappZ. Ich bedanke mich ebenso bei meinen Kolleg:innen im vierten Stock an der analytischen Chemie. Schließlich möchte ich bei meiner Familie bedanken, die mich stetig und umfänglich unterstüzte.

Danke!

Everything makes sense a bit at a time. But when you try to think of it all at once, it comes out wrong.

(Terry Pratchett)

Contents

List of Figures

List of Tables

Person

Full name	Simon Konrad Jobst
E-Mail	simon.jobst@oth-regensburg.de

Education

since 10/2018	Doctorate at the University of Regensburg Faculty of Chemistry and Pharmacy, Institute of Analytical Chemistry, Chemosensors and Biosensors
03/2013–09/2015	Master deg. in "Applied Research in Engineering Sciences", M.Sc.
10/2009–03/2013	Bachelor deg. in "Sensor Technology and Chemical Analysis", B.Sc.

Employment

since 08/2017	Research assistant at the Sensorik-Applikationszentrum, OTH Regensburg Artificial Intelligence in Sensor Technologies
11/2017–04/2018	Development engineer, Semstec UG Measurement of beverage container thicknesses
05/2016–07/2017	Test Engineer, Brunel AG Development testing of medicinal equipment
05/2015–12/2015	Development engineer, Semstec UG Sensor Calibration Design
03/2013–04/2015	Research assistant at the Sensorik-Applikationszentrum, OTH Regensburg Ultrasound Sensing Development

Internships

01/2016–04/2016	Research assistant at the Ultrasound Group, NTNU Trondheim, Norway Development of a two-probe setup for 3D ultrasound imaging
03/2012–03/2013	Student assistant at the Sensorik-Applikationszentrum, OTH Regensburg Ultrasound Sensing Development
09/2011–02/2012	Student assistant at the Laser Analytics Group, Cambridge University, UK Automatisation for superresolution microscopy

Poster presentations

"Miniaturized SPR-Imaging Sensor"
Peter Hausler, Simon Jobst, Jakob Wolf, Rudolf Bierl
Presented at the *95th IUVSTA Workshop on Plasmonic Thin Films: Theory, Synthesis and Applications* in 2022 (Guimarães, Portugal)

"Environmental Monitoring with Semi-Selective Receptors and Surface Plasmon Resonance Imaging"
Simon Jobst, Peter Hausler, Elisabeth Moser, Patrick Recum, Laurin Hastreiter, Ángela Écija-Arenas, Rudolf Bierl, Thomas Hirsch
Presented at the *FACSS SCIX 2024* in 2024 (Raleigh, USA)

Oral presentation

"Bestimmung von Brechungsindex und Dicke dünner Schichten mittels Oberflächenplasmonenresonanz",
Simon Jobst, Thomas Hirsch, Rudolf Bierl
Presented at the *122. Jahrestagung der Deutschen Gesellschaft für angewandte Optik* in 2021 (Bremen, Germany)

Publications as secondary author

Detailed record see: .

"A Measure of Confidence of Artificial Neural Network Classifiers"
Andreas Gschossmann, Simon Jobst, Jürgen Mottok, Rudolf Bierl
Published in *ARCS 2019 Workshop Proceedings* in 2019, ISBN 978-3-8007-4957-7

"A deep learning system to transform cross-section spectra to varying environmental conditions"
Elisabeth Moser, Simon Jobst, Rudolf Bierl, Frank Jenko

Published in *Vibrational Spectroscopy Vol. 122* in 2022

"An Algorithmic Approach to Compute the Effect of Non-Radiative Relaxation Processes in Photoacoustic Spectroscopy"
Max Müller, Thomas Rück, Simon Jobst, Jonas Pangerl, Stefan Weigl, Rudolf Bierl, Frank-Michael Matysik
Published in *Photoacoustics Vol. 26* in 2022

"Digital Twin of a photoacoustic trace gas sensor for monitoring methane in complex gas compositions"
Thomas Rück, Max Müller, Simon Jobst, Stefan Weigl, Jonas Pangerl, Rudolf Bierl, Frank-Michael Matysik
Published in *Sensors & Actuactors: B. Chemical Vol. 378* in 2023

"A sub-ppbv-level Acetone and Ethanol Quantum Cascade Laser Based Photoacoustic Sensor - Characterization and Multi-Component Spectra Recording in Synthetic Breath"
Jonas Pangerl, Elisabeth Moser, Max Müller, Stefan Weigl, Simon Jobst, Thomas Rück, Rudolf Bierl, Frank-Michael Matysik
Published in *Photoacoustics Vol. 30* in 2023

"Comparison of photoacoustic spectroscopy and cavity ring-down spectroscopy for ambient methane monitoring at Hohenpeißenberg"
Max Müller, Stefan Weigl, Jennifer Müller-Williams, Matthias Lindauer, Thomas Rück, Simon Jobst, Rudolf Bierl, Frank-Michael Matysik
Published in *Atmospheric Measurement Techniques Vol. 16, Iss. 18* in 2023

"Kinetic cooling in mid-infrared methane photoacoustic spectroscopy: A quantitative analysis via digital twin verification"
Thomas Rück, Jonas Pangerl, Lukas Escher, Simon Jobst, Max Müller, Rudolf Bierl, Frank-Michael Matysik

Published in *Photoacoustics Vol. 40* in 2024

The authors' original publication

[P1]
Semi-Selective Array for the Classification of Purines with Surface Plasmon Resonance Imaging and Deep Learning Data Analysis

S. Jobst, P. Recum, Á. Écija-Arenas, E. Moser, R. Bierl and T. Hirsch
in *ACS Sensors*, Volume 8, Issue 9, pp. 3530–3537

Abstract In process analytics or environmental monitoring, the real-time recording of the composition of complex samples over a long period of time presents a great challenge. Promising solutions are label-free techniques such as surface plasmon resonance (SPR) spectroscopy. They are, however, often limited due to poor reversibility of analyte binding. In this work, we introduce how SPR imaging in combination with a semi-selective functional surface and smart data analysis can identify small and chemically similar molecules. Our sensor uses individual functional spots made from different ratios of graphene oxide and reduced graphene oxide, which generate a unique signal pattern depending on the analyte due to different binding affinities. These patterns allow four purine bases to be distinguished after classification using a convolutional neural network (CNN) at concentrations as low as $50\,\mu mol\,L^{-1}$. The validation and test set classification accuracies were constant across multiple measurements on multiple sensors using a standard CNN, which promises to serve as a future method for developing online sensors in complex mixtures.

Declaration of Collaboration

Most of the theoretical and experimental scientific work that is presented within this thesis was done independently by the author. In some cases, however, the practical implementation of concepts and the performance of measurements was carried out in collaboration with other researchers and individuals. In any case, assistance was guided and supervised by the author. In accordance with § 7 Abs. 2 Satz 3 of *Ordnung zum Erwerb des akademischen Grades eines Doktors der Naturwissenschaften (Dr. rer. nat.) an der Universität Regensburg vom 18. Juni 2009 (Änderungssatzung vom 18. Dezember 2023)*, this section gives a detailed declaration of those collaborations.

In chapter 2 2D-materials have been provided by Dr. Patrick Recum and oil mixtures have been prepared by Dr. Peter Hausler (section B.1.3).
The experiments in chapter 3 using a CNN-LSTM and vision transformers have been conducted by Lukas Bauer as supervised by the author (section 3.3.3). The experimental setup as shown in Figure B5 was designed and built by Dr. Peter Hausler.
In chapter 4 Raman measurements, as well as absorbance spectra were recorded and analysed by Dr. Patrick Recum. Reduced graphene oxide and graphene oxide and their mixtures were fabricated by Dr. Patrick Recum. Analyte solutions were also prepared by Dr. Recum. Surface plasmon resonance measurements were conducted by Dr. Patrick Recum, Dr. Ángela Écija-Arenas, and the author. All graphics were made "publication-ready" by Dr. Patrick Recum. Conceptualisation and methodology as well as manuscript writing were a joint effort of

all paper authors.
In chapter 5 2D materials were provided by Dr. Patrick Recum. The measurement for Figure 5.3 has been performed by Dr. Lukas Wunderlich. The measurement presented in Figure 5.4 was conducted by Laurin Hastreiter.

Chapter 1

Introduction

In recent years, the reports of anthropogenic residue in the environment, ground water, and food steadily increased*. Micro- and nanoplastics are practically ubiquitous in the ocean [1, 2], per- and polyfluoroalkyl substances (PFAS) bioaccumulate and are commonly found in food [3–5], and pesticides and drug residues can be documented in ground water [6, 7]. Most of these substances can be harmful to the environment or to humans. It is imperative that they are monitored adequately so that their risks can be properly assessed, major polluters can be identified, and the effectiveness of regulatory measures can be evaluated on a scientific basis.

The monitoring of small molecules at many measuring sites is only possible with appropriate sensor devices that are capable of reliable and cost-efficient pollutant detection. The specific requirements for a biosensor vary greatly depending on its application. While a device measuring pollutant content in sweat needs to be wearable, thin, and non-invasive, the same requirements do not necessarily apply for a device detecting milk adulteration. However, several key properties are essential for successful sensor implementation: sensitivity and specificity towards the target analyte, portability allowing on-site usage, minimal need for recalibration, minimal or no pre-conditioning of media (label-free), reusability, and high detection speed. A combination of all these properties is not trivial to achieve and feasibility also depends on the recognition element that is responsible for capturing the analyte of interest and the applied transducer that converts association of an analyte to a measurable signal.

Transferring a biosensor from a controlled laboratory setting to the complexities of the real world presents a unique set of challenges [8]. It is impractical to account for every possible cross-sensitivity when dealing with biological fluids such as saliva, blood, or sweat as well as complex media like wastewater and food. This can alter the sensor response which may reduce sensitivity or cause a baseline shift due to fouling of the sensor's recognition element [9]. The recognition element may also deteriorate, or change over time, leading to baseline drift and sensor response alterations [10, 11]. Especially in continuous monitoring, reversibility of the recognition element is crucial. To address this, non-specific receptors are often employed so that the analyte interacts with the sensing element but can be removed easily. This results in a sensor that is not specific via chemical recognition alone but relies on multivariate data and machine learning for analyte recovery [12]. Sensors susceptible to baseline drift and sensitivity variations, including those caused by manufacturing inconsistencies [13], require frequent recalibration. However, complex calibration routines are often impractical and undesirable, especially for sensors deployed in real-world settings [14]. Therefore, integrating multiple sensors into a system can prove beneficial [15]. This multimodal data approach, while offering enhanced robustness, requires sophisticated interpretation techniques.
Many of these difficulties in biosensor development can be overcome with the assistance of artificial intelligence (AI). Breiman [16] argued that traditional models, which attempt to replicate real-world systems with equations, can lead to over-

*"Your brain is full of microplastics: are they harming you?", nature; "PFAS pollution in European waters", European Environment Agency

simplification or even misinterpretations of data and their underlying generative principles. Machine learning takes a different approach: it finds a model that best fits observed data. While this may be more challenging to interpret, it can often provide a more accurate representation of how data is generated. Therefore, machine learning is crucial for advancing biosensor technologies and has been recognised as a vital tool in the field [17–19]. However, it is important to remember that not every problem requires an AI solution. The argument here is that machine learning can be a powerful asset for tackling challenges, especially those that arise when moving biosensor technologies beyond the laboratory setting.

With the introduction of commercial tools based on large language models (LLMs), often incorporated directly into commonly used software, it becomes increasingly likely that a transformation of the work environment and daily life is imminent. Deep learning has matured from a technology mostly used for research to a diverse method applied across various fields - from A(stronomy) to Z(ebrafish) [20, 21]. Specialised hardware enables on-site learning and inference, software and pre-trained models are plentiful, freely available and cover everything from data curation to visualisation. This stands in stark contrast to its use in biosensing, a field still dominated by traditional data processing methods. Indeed, there is a gap between used methodology in biosensing and state of the art in deep learning.
Although artificial intelligence and machine learning are widely used in biosensor research [17–19], it can be argued that deep learning is underutilised.
Solutions have been reported for many fields related to biosensing: drift compensation [22], dealing with cross-sensitivites [23], multimodal data approaches [24], and managing high-dimensional data [25]. There are also exciting areas of research that can be utilised in biosensing.
The transformation of data into semantic embeddings, i.e. lower-dimensional space, can provide insights into sensing mechanisms. Since molecular structure can be mapped to their properties as well as sensor data to molecular properties [26], it would be very interesting to map sensor data and molecule structure thus allowing inference of specific molecular properties from sensor data.
Physics-informed neural networks (PINNs) are universal function approximators that incorporate a set of ordinary or partial differential equations describing physical laws. This strong bias improves convergence for smaller datasets while retaining flexibility beyond simple curve fitting. There is ongoing research to model binding or adsorption kinetics with PINNs which enables prediction of association parameters from observed transient data [27].
The success of LLMs stems from their ability to infer the task at hand from a given prompt due to the vast amount of training data embedded within their weights. This means the model was not explicitly trained for a specific task (e.g. translation) but has the information available in its training data corpus. By providing a few examples of the task at hand, it is then able to perform the task comparably to a model specifically trained on the task. These so-called foundation models are transferred to different domains, for example to image segmentation [28], which allows the extraction of regions of interest from images in a few-shot or zero-shot manner making it easily applicable.

This work aims to leverage machine learning in several ways to enhance the analytical performance of a surface plasmon resonance sensor. Surface plasmon resonance imaging (SPRi) provides high-dimensional data with high sensitivity towards the surface, suitable for analysis with machine learning. In particular, this work aims to enable specific signal processing for a SPRi setup that uses divergent light to alter the surface plasmon resonance conditions across the surface. It is explored how this information can be used in an analytical context for sensor characterisation, development and to enable new sensing methods. Additionally, it is investigated how deep learning can be employed to help with the detection of small molecules using the SPRi sensor and non-specific receptor elements. In summary, methods to utilise a custom imaging-based surface plasmon resonance setup analytically are developed and evaluated.

References

[1] R. C. Thompson, Y. Olsen, R. P. Mitchell, A. Davis, S. J. Rowland, A. W. G. John, D. McGonigle, A. E. Russell, "Lost at Sea: Where Is All the Plastic?", *Science* **2004**, *304*, 838–838, DOI 10.1126/science.1094559 (cit. on p. 2).

[2] M. Cole, P. Lindeque, E. Fileman, C. Halsband, R. Goodhead, J. Moger, T. S. Galloway, "Microplastic Ingestion by Zooplankton", *Environmental Science & Technology* **2013**, *47*, 6646–6655, DOI 10.1021/es400663f (cit. on p. 2).

[3] European Food Safety Authority, "Results of the Monitoring of Perfluoroalkylated Substances in Food in the Period 2000 - 2009", *EFSA Journal* **2011**, *9*, DOI 10.2903/j.efsa.2011.2016 (cit. on p. 2).

[4] European Food Safety Authority, "Perfluoroalkylated Substances in Food: Occurrence and Dietary Exposure", *EFSA Journal* **2012**, *10*, DOI 10.2903/j.efsa.2012.2743 (cit. on p. 2).

[5] M. Bartolomé, A. Gallego-Picó, F. Cutanda, O. Huetos, M. Esteban, B. Pérez-Gómez, A. Castaño, "Perfluorinated Alkyl Substances in Spanish Adults: Geographical Distribution and Determinants of Exposure", *Science of The Total Environment* **2017**, *603–604*, 352–360, DOI 10.1016/j.scitotenv.2017.06.031 (cit. on p. 2).

[6] D. Van Stempvoort, J. Roy, J. Grabuski, S. Brown, G. Bickerton, E. Sverko, "An Artificial Sweetener and Pharmaceutical Compounds as Co-Tracers of Urban Wastewater in Groundwater", *Science of The Total Environment* **2013**, *461–462*, 348–359, DOI 10.1016/j.scitotenv.2013.05.001 (cit. on p. 2).

[7] N. M. Burri, R. Weatherl, C. Moeck, M. Schirmer, "A Review of Threats to Groundwater Quality in the Anthropocene", *Science of The Total Environment* **2019**, *684*, 136–154, DOI 10.1016/j.scitotenv.2019.05.236 (cit. on p. 2).

[8] J.-F. Masson, "Consideration of Sample Matrix Effects and "Biological" Noise in Optimizing the Limit of Detection of Biosensors", *ACS Sensors* **2020**, *5*, 3290–3292, DOI 10.1021/acssensors.0c02254 (cit. on p. 2).

[9] H. Vaisocherová, E. Brynda, J. Homola, "Functionalizable Low-Fouling Coatings for Label-Free Biosensing in Complex Biological Media: Advances and Applications", *Analytical and Bioanalytical Chemistry* **2015**, *407*, 3927–3953, DOI 10.1007/s00216-015-8606-5 (cit. on p. 2).

[10] Z. Kovacs, D. Szöllősi, J.-L. Z. Zaukuu, Z. Bodor, F. Vitális, B. Aouadi, V. Zsom-Muha, Z. Gillay, "Factors Influencing the Long-Term Stability of Electronic Tongue and Application of Improved Drift Correction Methods", *Biosensors* **2020**, *10*, 74, DOI 10.3390/bios10070074 (cit. on p. 2).

[11] M. Song, X. Lin, Z. Peng, S. Xu, L. Jin, X. Zheng, H. Luo, "Materials and Methods of Biosensor Interfaces With Stability", *Frontiers in Materials* **2021**, *7*, 583739, DOI 10.3389/fmats.2020.583739 (cit. on p. 2).

[12] K. E. Schackart, J.-Y. Yoon, "Machine Learning Enhances the Performance of Bioreceptor-Free Biosensors", *Sensors* **2021**, *21*, 5519, DOI 10.3390/s21165519 (cit. on p. 2).

[13] P. Ciosek, W. Wróblewski, "Sensor Arrays for Liquid Sensing – Electronic Tongue Systems", *The Analyst* **2007**, *132*, 963, DOI 10.1039/b705107g (cit. on p. 2).

[14] S. Campuzano, M. Pedrero, M. Gamella, V. Serafín, P. Yáñez-Sedeño, J. M. Pingarrón, "Beyond Sensitive and Selective Electrochemical Biosensors: Towards Continuous, Real-Time, Antibiofouling and Calibration-Free Devices", *Sensors* **2020**, *20*, 3376, DOI 10.3390/s20123376 (cit. on p. 2).

[15] S. S. Chu, H. A. Nguyen, J. Zhang, S. Tabassum, H. Cao, "Towards Multiplexed and Multimodal Biosensor Platforms in Real-Time Monitoring of Metabolic Disorders", *Sensors* **2022**, *22*, 5200, DOI 10.3390/s22145200 (cit. on p. 2).

[16] L. Breiman, "Statistical Modeling: The Two Cultures", *Statistical Science* **2001**, *16*, 199–215 (cit. on p. 2).

[17] S. S. Arya, S. B. Dias, H. F. Jelinek, L. J. Hadjileontiadis, A.-M. Pappa, "The Convergence of Traditional and Digital Biomarkers through AI-assisted Biosensing: A New Era in Translational Diagnostics?", *Biosensors and Bioelectronics* **2023**, *235*, 115387, DOI 10.1016/j.bios.2023.115387 (cit. on p. 3).

[18] F. Cui, Y. Yue, Y. Zhang, Z. Zhang, H. S. Zhou, "Advancing Biosensors with Machine Learning", *ACS Sensors* **2020**, *5*, 3346–3364, DOI 10.1021/acssensors.0c01424 (cit. on p. 3).

[19] L. B. Ayres, F. J. Gomez, J. R. Linton, M. F. Silva, C. D. Garcia, "Taking the Leap between Analytical Chemistry and Artificial Intelligence: A Tutorial Review", *Analytica Chimica Acta* **2021**, *1161*, 338403, DOI 10.1016/j.aca.2021.338403 (cit. on p. 3).

[20] R. Hausen, B. E. Robertson, "Morpheus: A Deep Learning Framework for the Pixel-level Analysis of Astronomical Image Data", *The Astrophysical Journal Supplement Series* **2020**, *248*, 20, DOI 10.3847/1538-4365/ab8868 (cit. on p. 3).

[21] O. Ishaq, S. K. Sadanandan, C. Wählby, "Deep Fish", *SLAS Discovery* **2017**, *22*, 102–107, DOI 10.1177/1087057116667894 (cit. on p. 3).

[22] J. M. Margarit-Taulé, M. Martín-Ezquerra, R. Escudé-Pujol, C. Jiménez-Jorquera, S.-C. Liu, "Cross-Compensation of FET Sensor Drift and Matrix Effects in the Industrial Continuous Monitoring of Ion Concentrations", *Sensors and Actuators B: Chemical* **2022**, *353*, 131123, DOI 10.1016/j.snb.2021.131123 (cit. on p. 3).

[23] C. Fang, H.-Y. Li, L. Li, H.-Y. Su, J. Tang, X. Bai, H. Liu, "Smart Electronic Nose Enabled by an All-Feature Olfactory Algorithm", *Advanced Intelligent Systems* **2022**, *4*, 2200074, DOI 10.1002/aisy.202200074 (cit. on p. 3).

[24] Y. Zhang, T. H. Tao, "Skin-Friendly Electronics for Acquiring Human Physiological Signatures", *Advanced Materials* **2019**, *31*, 1905767, DOI 10.1002/adma.201905767 (cit. on p. 3).

[25] Z. Ma, Q. Xie, P. Xie, F. Fan, X. Gao, J. Zhu, "HCTNet: A Hybrid ConvNet-Transformer Network for Retinal Optical Coherence Tomography Image Classification", *Biosensors* **2022**, *12*, 542, DOI 10.3390/bios12070542 (cit. on p. 3).

[26] T. Debnath, S. Badreddine, P. Kumari, M. Spranger, "Comparing Molecular Representations, e-Nose Signals, and Other Featurization, for Learning to Smell Aroma Molecules", *PLOS ONE* **2023**, *18*, (Ed.: N. Q. K. Le), e0289881, DOI 10.1371/journal.pone.0289881 (cit. on p. 3).

[27] W. Ji, W. Qiu, Z. Shi, S. Pan, S. Deng, "Stiff-PINN: Physics-Informed Neural Network for Stiff Chemical Kinetics", *The Journal of Physical Chemistry A* **2021**, *125*, 8098–8106, DOI 10.1021/acs.jpca.1c05102 (cit. on p. 3).

[28] A. Kirillov et al., Segment Anything, **2023**, DOI 10.48550/ARXIV.2304.02643 (cit. on p. 3).

Chapter 2

Characterising Surface Plasmon Resonance Imaging for Biosensing

Surface plasmon resonance imaging (SPRi) has been extensively used in biosensor research for decades. It is crucial to characterise and optimise experimental conditions to generate meaningful and reliable results. Here, the conditions for optimal sensitivity of an SPR sensor to refractive index changes are reiterated and expanded towards a sensor with spatial information. The components of an SPRi sensor are characterised with regards to a biosensing application. This includes the SPR sensor surface, analyte transport, and recognition elements for analytes.

2.1 Introduction

In the late sixties Otto [1] and Kretschmann and Raether [2] independently described the excitation of surface plasmons by employing frustrated total reflection and total internal reflection, respectively. This allowed comprehensive explanation of a phenomenon observed as early as 1902 by Wood [3] who noticed alternating dark and light patterns when polarised light was reflected on a mirror with a grating. In 1983, Liedberg, Nylander, and Lundström first reported the use of surface plasmon resonance (SPR) sensing for biological applications and theorised that it could be valuable for measuring enzyme activity and hormone-receptor interactions [4]. Four years later, Yeatman and Ash described using surface plasmon resonance in combination with a camera to capture reflectance images in a Kretschmann-Raether setup [5]. The development of laterally resolved biosensing with very high sensitivity close to the sensor surface coincided with the rise of the CCD (charge-coupled device) sensors. Together with advances in computational power for digital signal processing of the camera images, this led to rapid and widespread adoption of surface plasmon resonance imaging (SPRi) in research.
In the following decades, SPRi was employed to image cells [6], monitor DNA hybridisation kinetics [7], characterise the biotin-streptavidin interaction [8], and track the spatial pattern of protein activity on a surface [9] utilising the lateral resolution provided by the image sensor. This spatial transducer was also exploited to introduce reference structures for correcting light intensity fluctuations [10] and for multiplexed measurements detecting multiple biomarkers in parallel [11].
SPRi was coupled with angular interrogation to determine optical properties over a large surface [12], wavelength variation for two-dimensional thin film quantification [13], phase imaging which provides higher sensitivity [14], and polarisation variation which can be used to determine layer parameters [15]. Thus, it has evolved into a standard tool for biosensing in biochemical research as well as health and environmental monitoring [16, 17].
Imaging-based SPR is a powerful technology allowing real-time, multiplexed, and label-free detection of biomolecules with potential for miniaturisation. The sensor surface can be used for the detection of multiple analytes but can also provide additional information on adsorbates or sensor state through spatial or temporal modulation of light wavelength or momentum.

This chapter provides a brief overview of SPR extending its definition to imaging and outlining its application in sensing. This sensor is then analysed in context of its application in a biosensing setup focussing on sensitivity. Furthermore, methods for enhancing its specificity are discussed.

2.2 Theory and Methods

Imaging instrumentation for surface plasmon resonance as a technique for biosensing is highly diverse.
O'Brien et al. [18] used a two-dimensional imaging sensor to modulate the incidence angle of light in one dimension while varying functionalisation in the other dimension. This information was used to track shifts in the resonance minimum due to binding. More commonly, angular scanning is achieved via a goniometer. Early studies recognised that proper referencing of the intensity is important for angular scanning devices [19]. More recently, instrumental setups using an acousto-optic deflector [20], or cylindrical lens arrays [21] for angular modulation in imaging have been applied.

In 1998, an interesting alternative to wide-field imaging emerged: microscope objective-based SPR (SPRM) which achieves angle-resolved SPRi with the help of a high numerical aperture (NA) lens [22]. In this approach a localised electric field in a microscopic region is generated by interfering surface plasmon polaritons. Another method uses an adjustable illumination axis offset in the back focal plane of the microscope objective relative to its axis to create different angles of incidence [23]. Microscopy enables very high spatial resolution due to the high NA which results in lateral resolution limits defined by the larger propagation length of surface plasmons rather than the Rayleigh criterion. SPRM has since gained traction and alternative setups have emerged utilising different methods to modulate the incident angle through a spatial light modulator [24] or enhance the signal-to-noise ratio of the microscope image by collecting the scattered light of biomolecules [25].

Wavelength modulation is a popular alternative to angular modulation for non-spatial detectors due to the high information content and the availability of spectrometers. In imaging wavelength information can be projected onto one sensor dimension effectively creating a 1D-image where every pixel holds wavelength information [26]. Seol Yuk et al. created a 2D image of a wavelength-interrogated sample by scanning the surface with a fiber-coupled spectrometer [27]. Since then various methods have been explored for direct wavelength modulated 2D imaging: acousto-optic tunable filters [28] or other monochromators [29], direct laser modulation [30], and using hyperspectral imagers [31].

In phase-based imaging the pronounced phase change during resonance is used to increase sensitivity. Phase measurement usually involves an interferometric configuration where the illumination is split before the interrogated surface and merged again before the detector. As a reference path both polarisations (p and s) were employed [32] as well as common-path interferometry was achieved using a

Wollaston prism [33]. The high resolution of these instruments comes with the cost of higher instrumental complexity.

As a deviation from the Kretschmann configuration, localised plasmon surface resonance (LSPR, [34]) has been employed in an imaging context often together with a microscope [35]. LSPR typically relies on the collection of wavelength information, which results in the application of spectrometers and different means of wavelength modulation, e.g. with a tunable filter [36].

Although numerous SPR imaging setups are used for biosensing [37–39], most of the intensity-based setups are variations of the setup schematically shown in Figure 2.1. Herein the base components can be reduced to a light source, a coupler with the sensor surface that is in contact with analyte solution, a flow cell, and a detector. The light source illuminating a planar sensor surface under total internal reflectance, ideally, is collimated, monochromatic, and polarised. The illuminated sensor surface has to be optimised for the task at hand by functionalisation of the surface via physical methods or chemical bonding of biomolecules. The analyte has to be transported to the sensor surface efficiently and predictably. The detector images the sensor surface with high spatial resolution and high dynamic range.

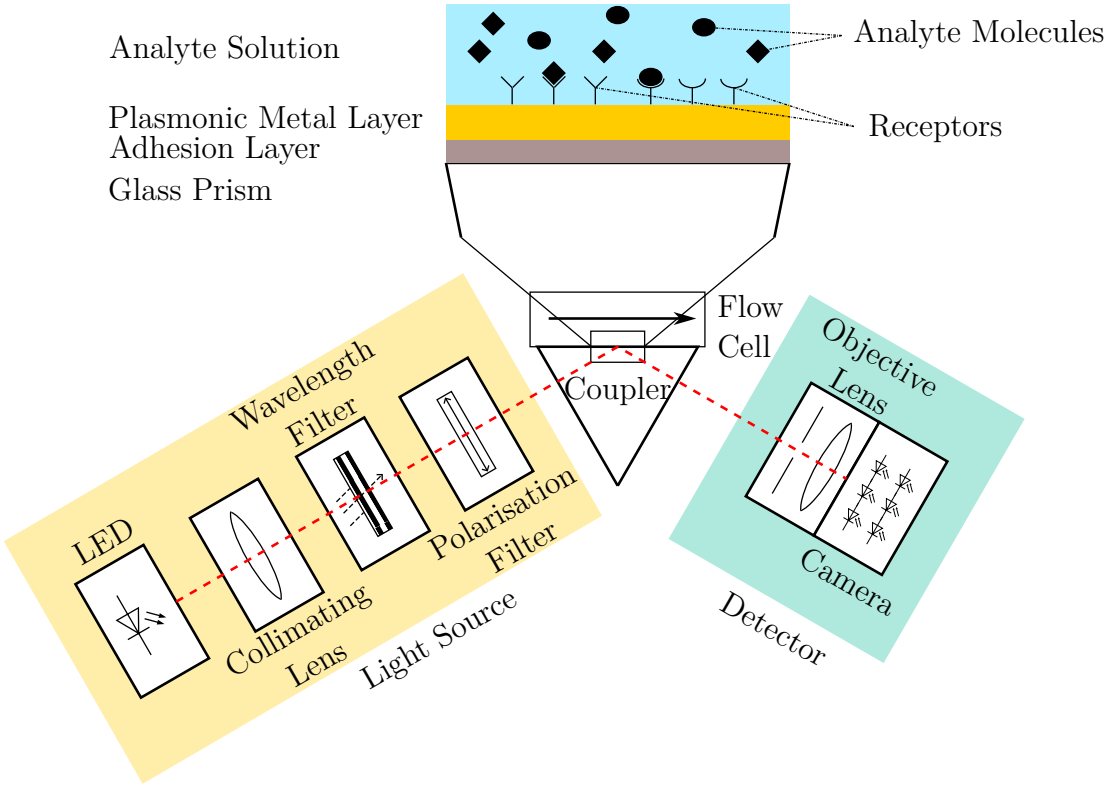

Fig. 2.1. SPRi sensor for biosensing with a collimated, polarised, and monochromatic light source, a prism coupler where the analyte is transported to the sensitive surface with immobilised receptor molecules by means of a flow cell. The reflected intensity is monitored with the help of a camera sensor.

Each sensor component must be carefully selected and their impact on the measured quantity has to be characterised. Within the scope of this work, the light source was treated as an entire component where only the output intensity distribution and the wavelength were considered. The coupler with the sensor surface is characterised in section 2.2.4, the flow cell in section 2.2.3.1 and the impact of the camera and the objective lens are discussed in section 2.2.2.
Experimentally, the system was tested with regards to its performance by analysing noise and by variation of optical configuration of the detector. Additionally, dispensing of 2D materials as receptors was optimised and examined with the help of plant oil. Those experiments are detailed in section B.1.

2.2.1 Surface Plasmon Resonance

A note on notation: Reflectance (R) represents the fraction of incident light power reflected from an interface. In this work the term reflectivity is used as a synonym. The reflection coefficients (r), which relate the amplitude of the reflected electromagnetic waves to the input amplitudes are complex quantities. The squared magnitude of the reflection coefficients yields the reflectivities. Refractive indices are generally denoted as n, in cases where the refractive index is a complex quantity, it becomes $\hat{n} = n + i\kappa$ where κ is called extinction coefficient. The refractive index is also related to the relative permittivity ϵ_r via $\hat{n}^2 \approx \hat{\epsilon}_r$ with the complex extinction coefficient $\hat{\epsilon}_r$ (for conducting, non-magnetic materials at optical frequencies) [40, p. 76].

Surface plasmon resonance is widely used in biosensing due to its high sensitivity to analyte changes close to the sensor surface. This high sensitivity is a result of an electromagnetic wave travelling parallel to a metal-dielectric interface probing into the dielectric in form of an evanescent wave. Under certain conditions this surface wave resonantly couples with an incident electromagnetic wave which means that slight changes in the dielectric can be observed in the reflected electromagnetic wave. SPR theory has been extensively studied and descriptions of generation and propagation of surface plasmon polaritons can be found in several textbooks [41–44]. However, a short summary of the most meaningful equations impacting this work is provided in this chapter.
It is well known, that in order to excite surface plasmons the energy and momentum of the exciting photons must match that of the surface plasmon on the metal interface. The momentum in particular cannot be matched with free-space photons, that is why coupling the photons through prisms or gratings is indispensable. Within this work, only Kretschmann-Raether type setups are used, where a glass prism is employed for coupling and the medium of interest is directly in vicinity of the metal surface on the prism [2].
For a derivation of the surface plasmon dispersion relation, see either section A.1 or the textbooks cited above for a more rigorous treatment. Since s-polarised light cannot excite surface plasmons, only p-polarised light is considered. For the purpose of this work, a three-layer system is assumed given by: a semi-infinite glass prism (1), a metal layer of thickness d (2) and a semi-infinite dielectric (3). The frame

of reference is chosen as indicated by Figure 2.2, the p-polarised wave is chosen to travel in x-direction, there is no electric field in the y-direction.

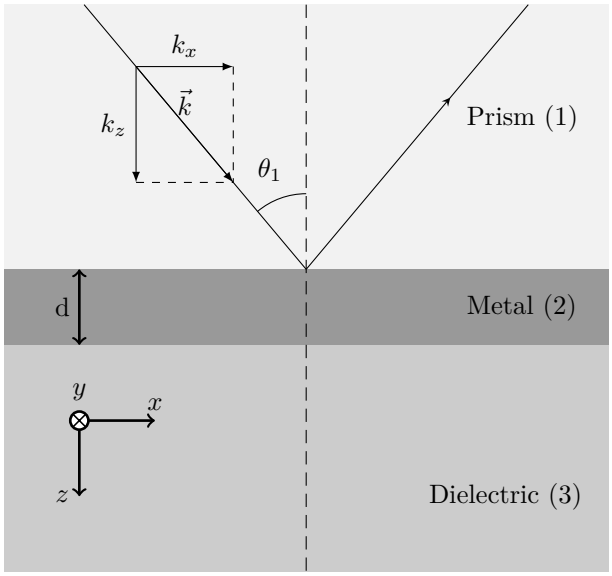

Fig. 2.2. Three-layer system of a glass prism, a metal thin film with thickness d and a dielectric. The wave vector of the incident wave and its components are sketched. The indicated coordinate system is used throughout the following equations.

The reflectivity of this system is given by [45]

$$R = |r^{\mathrm{p}}_{123}|^2 = \left|\frac{E^{\mathrm{p}}_{\mathrm{r}}}{E^{\mathrm{p}}_0}\right|^2 = \left|\frac{r^{\mathrm{p}}_{12} + r^{\mathrm{p}}_{23}\exp(2ik_{z2}d)}{1 + r^{\mathrm{p}}_{12}r^{\mathrm{p}}_{23}\exp(2ik_{z2}d)}\right|^2. \tag{2.1}$$

The reflectivity is the magnitude of the ratio of reflected electric field E_{r} to incident electric field E_0, which is dependent on the reflection coefficients for the transitions of prism to metal (r_{12}) and metal to dielectric (r_{23}). $k_{\mathrm{z}2}$ is the wave vector in z-direction in the metal and d is the thickness of the metal film.
Using Snell's law and the geometry of the wave vector, k_{z2} can be rewritten as

$$k_{z2} = \frac{2\pi}{\lambda}\sqrt{\hat{\epsilon}_2 - n_1^2\sin^2\theta_1}, \tag{2.2}$$

with the wavelength of light λ, the (complex) relative permittivity of the metal $\hat{\epsilon}_2$, the (real) refractive index of the prism n_1, and the incidence angle θ_1. Similarly, the reflection coefficients for the interfaces prism-metal and metal-dielectric are given by the Fresnel equation:

$$r^p_{ik} = \frac{\hat{n}_k\cos\theta_i - \hat{n}_i\cos\theta_k}{\hat{n}_k\cos\theta_i + \hat{n}_i\cos\theta_k}. \tag{2.3}$$

With these equations, an angle of incident-dependent reflectivity can be calculated for known refractive indices of the three phases and a defined thickness of the metal film (Figure 2.3). When the conditions for the excitation of surface plasmons are met,

i.e. energy and momentum of incident light matches that of the surface plasmons, a dip of the reflected intensity of p-polarised light can be observed above the angle of total internal reflection (TIR). This is a result of the incident light coupling with surface plasmon modes (see Equation A.4).

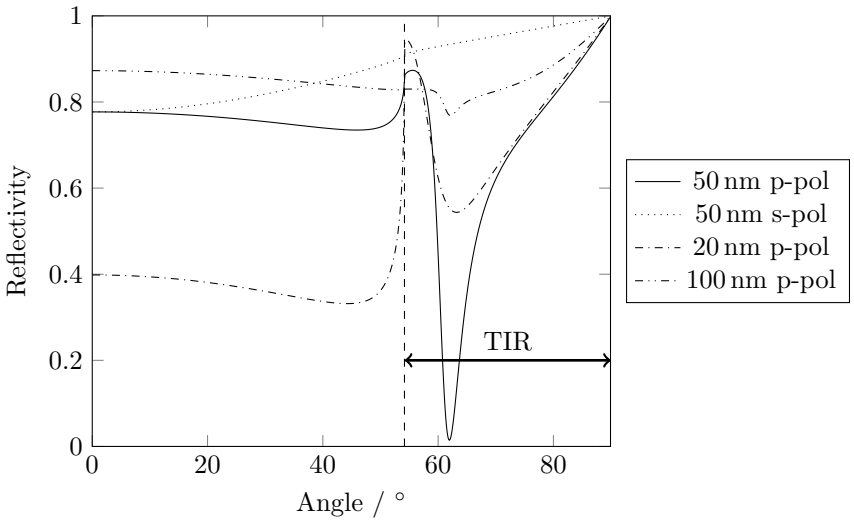

Fig. 2.3. Reflectivity for different gold thicknesses at a wavelength of 660 nm and 25 °C, a prism refractive index of 1.6418, metal refractive index of $0.2843+i3.3825$, and water as dielectric ($n^{25} = 1.3310$). Since the reflectivity is dropping above the critical angle for total internal reflection (TIR), this mode of operation is called attenuated total reflection (ATR). The resonance is highly dependent on the metal thickness and s-polarised light is unaffected.

The efficiency of this coupling is strongly dependent on the refractive indices and thicknesses of the layers, as well as the light wavelength and incident angle. This dependency is utilised for sensing of the dielectric. Physically, the light wave reflects at the prism-metal interface but partially penetrates the thin metal film as an exponentially decaying wave. This decaying wave can excite surface plasmons on the metal-dielectric interface, which are electron oscillations on the metal surface. These oscillations, in turn, generate an electromagnetic field that radiates back into the metal film, interfering destructively. Under ideal coupling, the reflected beam vanishes.

There are several ways of exploiting the reflectance change through spatial or temporal modulation of light wavelength or momentum. Typically, in a sensor setup the medium of interest is the dielectric itself or, more commonly, surface adsorption or binding of an analyte from the dielectric. Both result in a change in refractive index of the dielectric which result in altered resonance conditions. The change can be detected in several ways, e.g., by tracking the angle of the reflection minimum or the reflected intensity directly. In this work, a simple approach was used: tracking the intensity of the reflected light under fixed conditions (angle and wavelength). In Figure 2.4 this approach is illustrated: the reflectivity is recorded at a fixed angle, that is chosen so the slope is maximised. On changes in refractive index the reflection

changes, for small Δn_{di} a linear relationship between refractive index and reflectance can be found. Similarly, reflectivity changes when biomolecules adsorb to the sensor surface, which can be modelled as a thin layer on top of the gold surface with a refractive index distinct from that of water. Depending on noise of the measurement miniscule changes, which are in the 1×10^{-7} RIU (refractive index units) range or at sub-molecule scale can be detected which highlights the high sensitivity at the surface [46, 47].

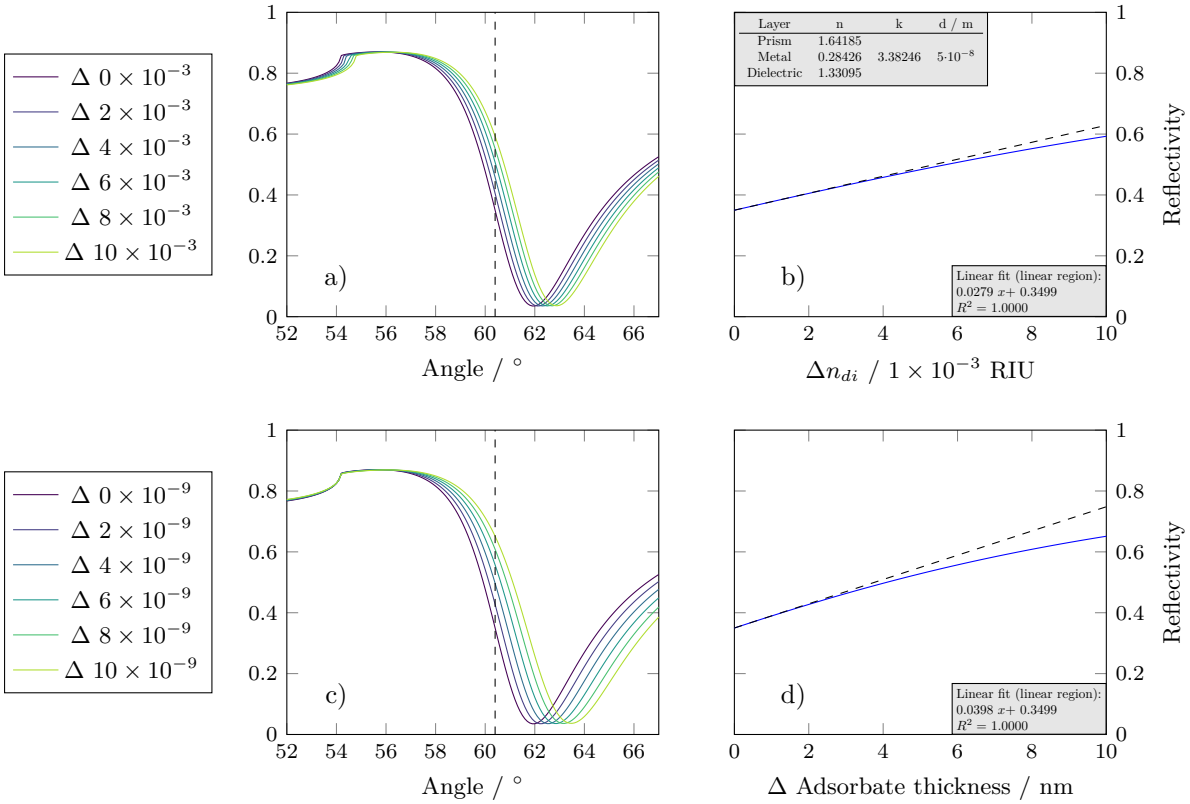

Fig. 2.4. Angle-dependent reflectivity for different changes in refractive index (a) and thicknesses of an adsorbing molecule layer in nanometers (c). The dashed lines in (a) and (c) mark the angle of maximum sensitivity at which the reflectivity for the graphs on the right is extracted. Intensity-based readout of a change in refractive index of the dielectric (b) and thickness of layer of adsorbing molecules with a refractive index of 1.5 [48] (d) at 660 nm and 25 °C. The dashed lines shows the linear fit for a change of 1×10^{-3} RIU and 1 nm respectively.

When observing only the reflected light intensity, it is impossible to discriminate a change of refractive index in the dielectric from adsorption of a target analyte to the sensor surface. This distinction can be made when there are multiple responses from several sites on the sensor surface featuring different modifications that, e.g. block binding of an analyte or irreversibly bind to the ligand so that it remains bound after replacing the dielectric. A spatial sensor allows parallel detection of such sites which enables fast and accurate determination of the quantities of interest.

2.2.2 Surface Plasmon Resonance Imaging

In SPR imaging, a spatial detector such as a CCD camera captures the reflected light. This allows tracking of the laterally resolved reflectivity of the surface. The responses from the surface can be used to spatially average the intensity in order to reduce noise, or to track the intensity of several functional surface reactions in parallel [37], which can be exploited to compare the observed intensity of an analyte interaction with a reference area to eliminate intensity fluctuations, temperature effects or bulk refractive index changes [49–51]. To observe independent interactions on the sensor surface, the probed sites must be farther apart than the propagation length of the surface plasmons. Surface plasmons travel parallel to the interface meaning they have a non-zero propagation length and therefore affect the captured image. As a result, the surface plasmons limit the lateral resolution of the sensor. The observed image is the convolution of the imaged object, the point spread function (PSF) of the optical system, and the decay function of the surface plasmon [52–54]. If two independent events on the surface are to be observed, the two sites should be farther apart than the surface plasmon propagation length.
The propagation length of the surface plasmon is inversely proportional to the imaginary part of the wave vector travelling along the surface,

$$L_x = \frac{1}{2\mathfrak{Im}(k_x)} \tag{2.4}$$

with k_x defined in Equation A.2.
For gold, this translates to a distance of a few micrometers, which can affect the spatial resolution of a sensor. In Figure 2.5 several wavelength dependent quantities for gold are depicted, similar to Figure 3 in [54]. While the propagation length increases with the wavelength, the sensitivity does, too (Figure 2.5 a and e). For SPRi the consequence is that there is a trade-off between lateral resolution and refractive index sensitivity. It is interesting to note that the refractive index sensitivity of a bulk change (Figure 2.5 e) increases with the wavelength, while sensitivity to a thickness increase of an adsorption layer on top of the gold surface plateaus at higher wavelengths (Figure 2.5 f). This analysis suggests an optimal wavelength for surface-bound sensing. This is due to the fact that the electric field penetrates deeper into the medium (Figure 2.5 b) which limits its sensitivity towards surface effects. The sensitivity can be understood as a percentage change in intensity as reflectivity is directly proportional to the observed intensity (disregarding the PSF).
For a point reflector on a homogeneous surface illuminated with a collimated light source in lossless space, the intensity at the detector can be written as:

$$I(x, y) = (R(x) * \mathrm{PSF}(x, y)) \cdot I_0(x, y) \tag{2.5}$$

where $R(x)$ is the reflectivity along the propagation of the surface plasmon, $\mathrm{PSF}(x, y)$ is the point spread function of the optical system and $I_0(x, y)$ is the input intensity. Lateral resolution consequently depends on the imaging setup, including prism base angle and refractive index, objective lens and aperture as well as their positioning relative to the sensor. The setup is ideally designed to achieve a field of view (FOV)

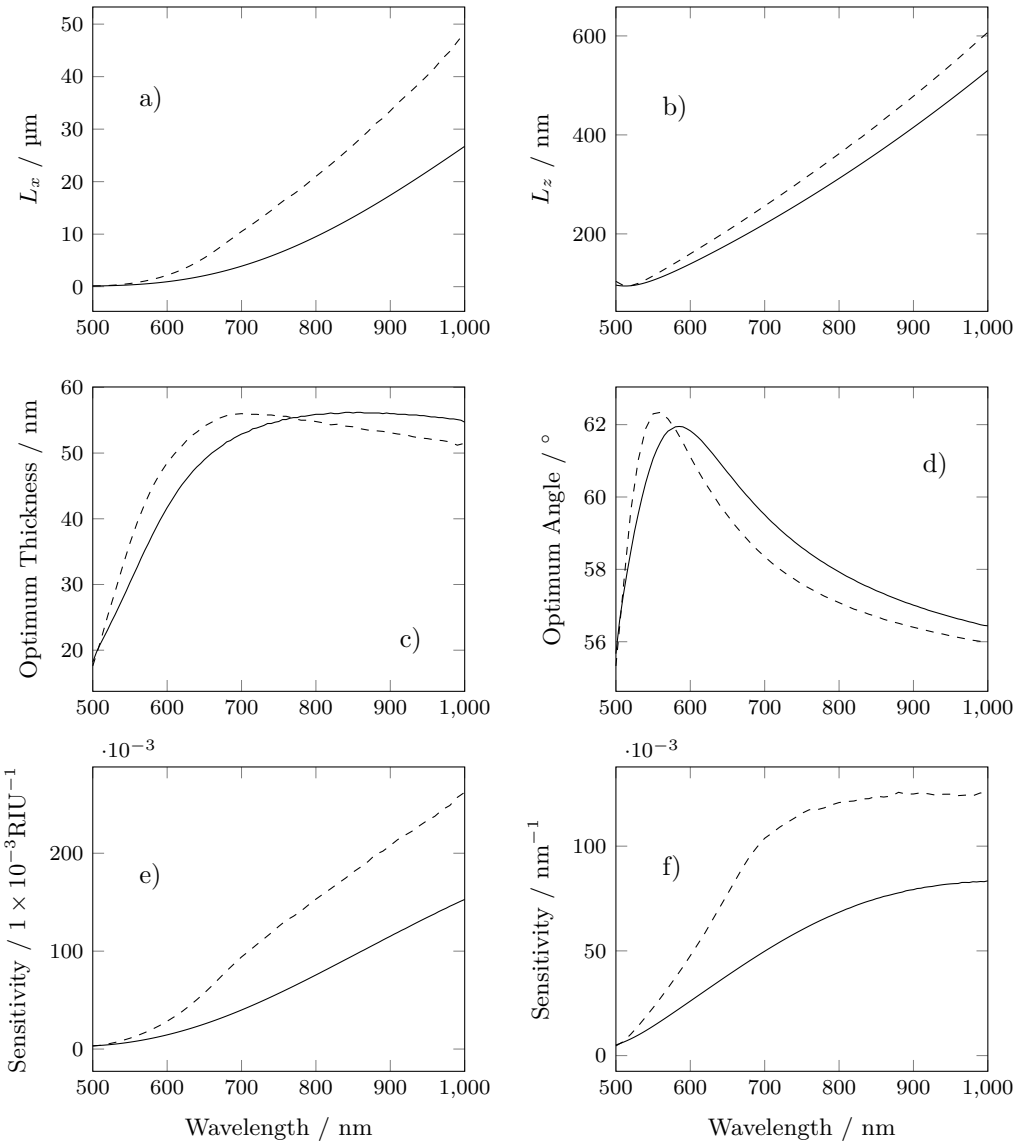

Fig. 2.5. Wavelength dependent lateral propagation length (a) and penetration depth (b) of the electric field; optimum thickness of the gold film (c), i.e. thickness with which the maximum sensitivity (highest slope of the SPR curve) is reached; optimum angle of incidence for intensity-based readout (d); reflectivity sensitivity towards bulk refractive index changes (e); reflectivity change on thickness change of an adsorption layer with refractive index 1.5 on top of the gold surface (f). Graphs are based on numerical simulation and inspired by [54]. Solid lines represent gold refractive indices modelled after Lorentz-Drude, and dashed curves represent gold refractive indices after [55]. Glass is modelled after Sellmeier equations (section A.2) for Schott SF2 section C.2, and the dielectric is water which is modelled after [56]. The adhesion layer for gold on glass, which is frequently chromium, generally decreases the sensitivity and is omitted here. All calculations at a temperature of 25 °C.

to capture the entire sensor surface and a depth of field (DOF) that enables focused imaging of the tilted surface with respect to the optical axis. To optimise lateral resolution, one has to illuminate the surface so that the main ray is perpendicular to the prism surface and place the detector perpendicular to the optical axis. According to the Scheimpflug principle this results in a tilted image plane with regard to the detector Figure 2.6.

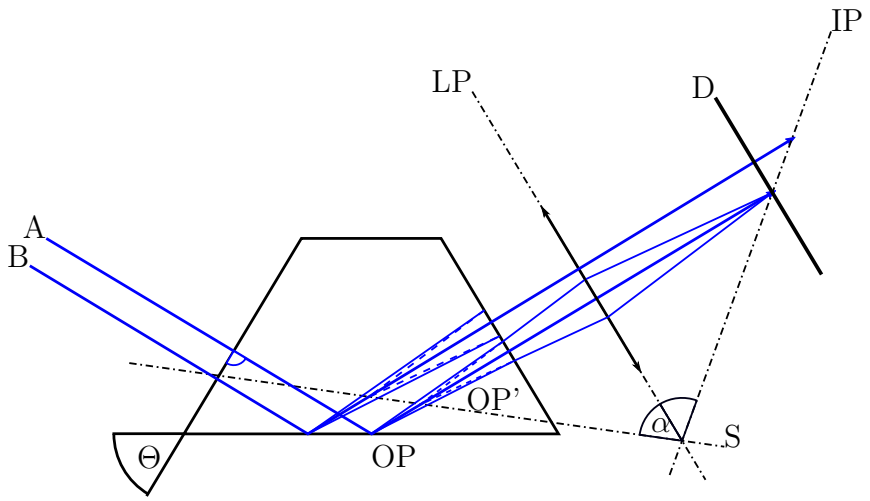

Fig. 2.6. When light rays (A and B) perpendicular to the prism surface with prism base angle Θ are reflected on the sensor surface, these reflections are not perfectly specular resulting in a virtual object plane OP'. This plane (and also the object plane for that matter) is not parallel to the lens plane (LP) which means that the image plane (IP) is not parallel to the lens plane either. LP, OP' and IP intersect in a point S and OP' and IP are tilted in the same angle α with regard to the LP. α for a specular reflection is identical to the prism base angle. The detector D, however, is placed parallel to the LP, which results in only a strip being in focus at once. Diffuse reflected light of ray B is only depicted until the prism-air interface; this is to show construction of the virtual image plane without overloading the image.

Alternatively, the detector can be positioned parallel to the image plane to maximise FOV while retaining maximum lateral resolution. This, however, results in rather steep angles of incidence on the prism [54]. It was therefore chosen to limit the aperture of the objective lens to increase the DOF, which reduces the lateral resolution but allows using a simple optical setup (as sketched in Figure 2.6). The desired mode of operation of the SPRi system defines which optical components should be used. When imaging a large tilted surface (i.e. $1\,\mathrm{cm}^2$ and larger) with regard to the detector, DOF should be high but lateral resolution can be limited since on a large surface more functional spots can be realised than on a smaller surface. The impact of an aperture reduction was characterised, with results presented in section B.1.2.

2.2.3 Recognition Elements

To maximise utility of a two-dimensional detector beyond redundancy, spatial modulation of reflectivity must be employed. This can be achieved using recognition elements for analytes of interest. There are different types of interactions which are generally classified by their binding energy. The metal surface is prone to non-specific adsorption, which is typically unwanted in biosensing and hence commonly blocked using self-assembled monolayers (SAM) of thiolated hydrocarbon chains which strongly bind to gold. This is one of the main reasons why gold is widely used as thin-film metal in plasmonics, as its surface chemistry with thiols is well-characterised and diverse [57].

2.2.3.1 Analyte Transport

The analyte of interest must be transported to the specific recognition elements on the sensor surface. The exact interaction mechanism is not considered here as transport and binding is the focus. Herein, the analysis is limited to pseudo-first order kinetics. For a more rigorous approach, see, most notably, the works of Squires et al. and Saftics et al. [58, 59] as well as several textbooks [42, 44, 60].

Let us first assume a system where a sensor surface is exposed to an analyte that binds to specific binding sites on that surface. Let us also assume a well-mixed system which means the concentration of the analyte at the surface (c_s) is the same as in the medium which holds the analyte (c_0), i.e. $c_\mathrm{s} = c_0$ and assume an infinite supply of analyte ($c_0 = \text{const.}$). Binding sites are independent and distinct from one another and per site only one analyte molecule may bind (Langmuir adsorption [61]):

$$A_\mathrm{S} + B \underset{k_\mathrm{a}}{\overset{k_\mathrm{d}}{\rightleftharpoons}} AB. \tag{2.6}$$

The adsorbate A_S may bind to the binding site B with a rate constant k_a and desorption is characterised by k_d. The time-dependent adsorption process can be written as,

$$\frac{\mathrm{d}b}{\mathrm{d}t} = k_\mathrm{a} c_\mathrm{s} (b_\mathrm{m} - b) - k_\mathrm{d} b \tag{2.7}$$

where b is the time-dependent number of adsorbates per unit area, b_m is the maximum number of analytes per unit area and c_s is the (surface) concentration of the analyte molecule $[A_\mathrm{S}]$. Assuming a well-mixed system, it can be written:

$$\frac{b(t)}{b_\mathrm{m}} = \frac{1}{1 + K_\mathrm{D}/c_0} \left(1 - e^{(-k_\mathrm{a} c_0 + k_\mathrm{d})t}\right) \tag{2.8}$$

with the dissociation constant $K_\mathrm{D} = k_\mathrm{d}/k_\mathrm{a}$. For $t \to \infty$ the exponential vanishes and a fraction of bound molecules which is dependent on the ratio of K_D and c_0 remains. With known kinetic constants and analyte concentration, it is also possible

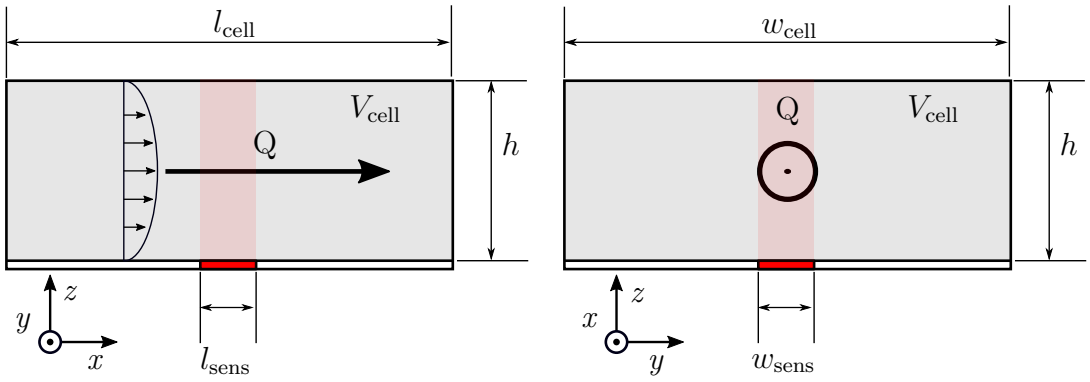

Fig. 2.7. Flow cell geometry and parabolic flow profile developing with laminar flow.

to calculate the time τ_Θ until the steady state – the state of balanced ad- and desorption so the number of bound molecules is constant – is reached:

$$\tau_\Theta = -\frac{-\ln(1-\Theta)}{k_\mathrm{a} c_0 + k_\mathrm{d}} \tag{2.9}$$

where Θ is the fraction of equilibrium. Steady state concentration analysis can be used to calculate the dissociation constant when recording the sensor response at different concentrations. The concentration has to be set at values around the dissociation constant ($c_0 = K_\mathrm{D}$ relates to 50 % occupied binding sites) in order to generate meaningful results when analysing steady-state concentration series.

A well-mixed system is rarely achieved in practice. More generally, the analyte is transported to the recognition element, e.g. with the help of a pump that moves liquid through a flow cell. A flow cell with a rectangular cross-section ($w_{\text{cell}} \times h$) is assumed, where fluid enters at $x = 0$ and leaves at $x = l_{\text{cell}}$ with volume flow Q. The sensing area where recognition elements are placed with a surface density b_m is characterised by its length and width (Figure 2.7). Due to the dimensions (i.e. h in the range of 1×10^{-4} m to 1×10^{-3} m) and the volume flow (less than 1 mL/min) in aqueous solutions laminar flow develops in the cell. The sensing area shall be far enough from the inlet so that the laminar profile has fully developed.
Consequently the flow rate is zero at the bottom and top of the flow cell ($z = 0$, $z = h$) and reaches its maximum at $z = h/2$. Thus, analyte transport to the surface by laminar flow is zero for these conditions. Due to the introduced concentration non-uniformity, diffusion becomes the main driving force of analyte transport.
The analyte concentration then becomes a spatiotemporal quantity depending on diffusion and convection (we assume diffusion in y-direction to be negligible)

$$\frac{\partial c(t,x,z)}{\partial t} = D\left(\frac{\partial^2 c(t,x,z)}{\partial x^2} + \frac{\partial^2 c(t,x,z)}{\partial z^2}\right) - u_x(z)\frac{\partial c(t,x,z)}{\partial x} \tag{2.10}$$

with the flow velocity profile of the fluid $u_x(z)$ and the diffusion coefficient D. This equation can be solved numerically. The boundary condition at $z = 0$ of this partial

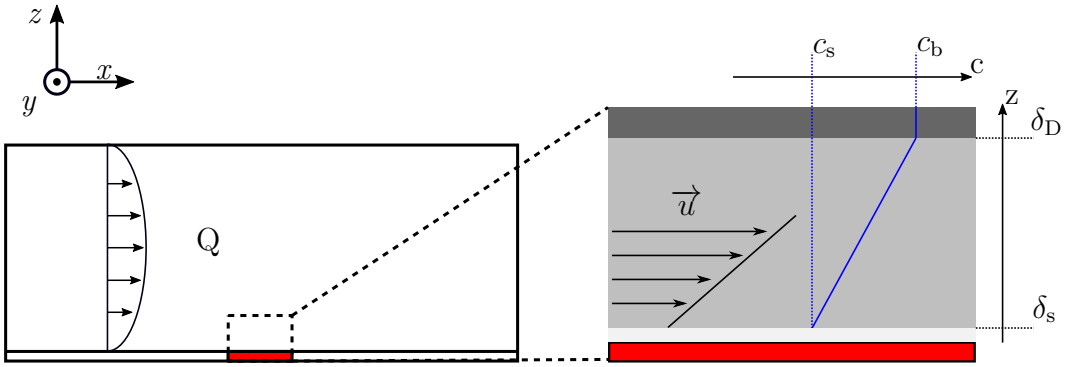

Fig. 2.8. Assumptions of the two compartment model for the DBL: close to the sensor surface a linear flow profile can be assumed; at a distance δ_D from the sensor surface, the analyte concentration is equal to the bulk concentration and varies linearly with distance to the surface.

differential equation (PDE) depends on the rate equation for first-order kinetics (Equation 2.7) but modified by the time and space-dependent quantities for bound molecules and available binding sites.
It is, however, possible to derive simpler analytical models for this system when isolating flow and diffusion into a two-compartment model. In this model the concentration far from the surface is considered constant while close to the surface a diffusion boundary layer (DBL) is formed as a constant concentration gradient between bulk and surface is formed. The height of the DBL depends on the ratio between convection and diffusion (see Figure 2.8).
This results in an effectively two-step process for adsorption

$$A_B \xrightarrow{k_m} A_S + B \underset{k_a}{\overset{k_d}{\rightleftharpoons}} AB \tag{2.11}$$

where k_m is the kinetic constant for mass transport of the bulk analyte A_B to the surface A_S. The rate equation for the surface concentration becomes

$$\frac{dc_s}{dt} = \frac{1}{\delta_D/2}\left(k_m(c_b - c_s) - k_a c_s(b_m - b) + k_d b\right) \tag{2.12}$$

with the DBL thickness δ_D. If the surface concentration is in steady state, c_s can be found to

$$c_s = \frac{c_b k_m + k_d b}{k_a(b_m - b) + k_m} \tag{2.13}$$

which together with Equation 2.7 gives

$$\frac{db}{dt} = \frac{k_a}{1 + (b_m - b)k_a/k_m} c_b(b_m - b) - \frac{k_d}{1 + (b_m - b)k_a/k_m} b. \tag{2.14}$$

This equation can be analysed similarly to Equation 2.7 by substituting $k_f = k_a/(1 + (b_m - b)k_a/k_m)$ and $k_r = k_d/(1 + (b_m - b)k_a/k_m)$. At $(b_m - b)k_a/k_m \ll 1$ transport is much faster than binding and the kinetics are reaction dominated, i.e.

$k_f \approx k_a$ and $k_r \approx k_d$.
When the velocity profile close to the sensor surface is linear (Figure 2.8), diffusion in the direction of flow is neglected, and the surface concentration is zero, hence it is a perfect sink, Equation 2.10 can be simplified and solved to give an expression for k_m [62]

$$k_\mathrm{m} = \frac{D}{\delta_\mathrm{D}} = 0.67 \left(\frac{w u_\mathrm{max}}{Dhx}\right)^{(1/3)} D \tag{2.15}$$

with the DBL thickness δ_D, the dimensions of the surface with receptors (as indicated in Figure 2.7) and the maximum flow velocity u_max. This can be expressed as an average $\overline{k_\mathrm{m}}$ by integrating over x from 0 to l and normalising with l [63]

$$\overline{k_m} = 0.98 \left(\frac{D}{h}\right)^{(2/3)} \left(\frac{Q}{0.3wl}\right)^{(1/3)}. \tag{2.16}$$

According to Equation 2.15 the size of the DBL is dependent on the geometry of the flow cell and the volume flow of the medium but has an important effect on the kinetics of the system which is why the flow has to be chosen carefully for every experiment. A small DBL leads to shorter diffusion times and thus faster response but can also mean that molecules cannot bind before they get swept away. For a fixed flow, higher k_a result in a faster steady state but may lead to transport-limitation as the molecules are bound as soon as they arrive at the surface (see Figure 2.9).

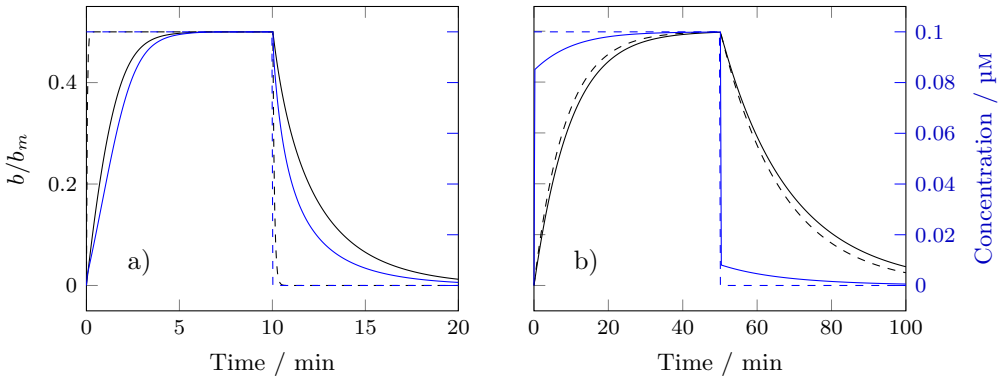

Fig. 2.9. Fraction of bound molecules over time when a step-like concentration change (dashed blue lines) is introduced in a well-mixed system (black dashed lines) and a convection-diffusion system (black solid lines). Surface concentration is depicted as a blue solid line. The system in a) is diffusion bound ($(b_\mathrm{m} - b)k_\mathrm{a}/k_\mathrm{m} > 1$), the main limitation for steady state to be reached is the surface concentration; the case in b) is calculated with the same flow parameters but different kinetic constants of the binding reaction so that $(b_\mathrm{m} - b)k_\mathrm{a}/k_\mathrm{m} < 1$ which means that the system is reaction-limited. Note that the system in b) takes longer to reach steady state; $c_\mathrm{b}/K_\mathrm{D} = 1$ so steady state fractional coverage will be 0.5 (calc. from Equation 2.7, Equation 2.12 and Equation 2.14 for: a 1 mm by 1 mm sensor spot in a 0.5 mm high flow cell with $Q = 100\,\mu\mathrm{L/min}$, $D = 1 \times 10^{-11}\,\mathrm{m^2\,s^{-1}}$ and a receptor density of $1 \times 10^{13}\,\mathrm{m^{-2}}$; a) $k_\mathrm{a} = 2 \times 10^6\,\mathrm{M^{-1}\,s^{-1}}$; b) $k_\mathrm{a} = 1 \times 10^4\,\mathrm{M^{-1}\,s^{-1}}$).

With very low bulk concentrations the diffusive flux will be lower, which means that it takes a long time for surface concentration equilibrium to be reached. Similarly, this affects the time until surface reaction equilibrium is reached. A sensor with area A has a number of $N_\mathrm{R} = b_\mathrm{m}A$ receptors, where the number of bound receptors in equilibrium is dependent on Equation 2.8:

$$\frac{b_\mathrm{eq}}{b_\mathrm{m}} = \frac{1}{1 + K_\mathrm{D}/c_0} \tag{2.17}$$

When $K_\mathrm{D} \gg c_0$, this becomes $b_\mathrm{eq} \approx b_\mathrm{m}c_0/K_\mathrm{D}$ and thus $b_\mathrm{eq} \ll b_\mathrm{m}$. The number of bound receptor spots becomes $N_\mathrm{R}^\mathrm{b} \approx b_\mathrm{eq}A$ and for at least one molecule to be bound the concentration has to be larger than:

$$c_\mathrm{min} = \frac{K_\mathrm{D}}{b_\mathrm{m}A}. \tag{2.18}$$

For $Q \to 0$, the two compartment model is no longer valid and diffusion becomes the sole transport mechanism to the surface. There is no general closed-form solution for diffusion-limited binding but numerical methods allow calculation of diffusion-bound surface coverage. The DBL expands $\propto \sqrt{Dt}$ which means that analyte transport becomes increasingly slow and can significantly impact the observed kinetics.
In conclusion, analyte concentration, flow and the dimensions of the flow cell are important parameters for the observation of an interaction with specific kinetic parameters. They not only affect the exact shape of the time-dependent amount of bound molecules but the time to reach steady state. When equilibrium is assumed even though the sensor has not reached steady state, incorrect kinetic parameters may be adopted which leads to measurements at a non-ideal operating point or even incorrect conclusions, entirely [60, 64, 65].

2.2.3.2 Interaction Types

From an SPR sensing perspective the ideal recognition element attaches irreversibly to the metal surface, is impermeable to suppress unwanted binding of the medium with the metal surface, and is thin enough to avoid perturbing the SPR response. Additionally, the recognition element has to reversibly and quickly bind to the analyte. Reversibility is a somewhat arbitrary term, since it depends on the time frame and energy of a regeneration step, e.g. a washing step without analyte, or a change in temperature.
Here, binding energy is expressed in quantities of kT (product of Boltzmann constant and temperature) so that environmental thermal energy is accounted for.
Apart from chemical reactions leading to covalent bonds, specific bonds do not have to be strong bonds (in terms of energy), but a specific bond is selective in its partners. Specificity is achieved by compatible arrangement of interaction sites (between receptor and analyte). A range of interactions can occur in a biosensor. Coulomb interactions involve charged partners and are relatively long-range and high energy (up to 200 kT). The Van der Waals interaction, which is the sum of Keesom

(dipole-dipole), Debye (dipole-induced dipole) and London dispersion (instantaneous dipole) interactions, has much lower energy ($\approx 1\,\mathrm{kT}$) and shorter range. In aqueous media, hydrogen bonds (at around $5 - 10\,\mathrm{kT}$) and hydrophobic interactions are also significant. The latter are very difficult to quantify since they are a result of the environment rather than an attraction due to charge distribution [66, pp. 80 sqq.][44, p. 174]. A hydrophobic surface can result in strongly bound hydrophobic molecules in aqueous media, as the molecule can be expelled from the aqueous phase and deform to bind irreversibly when in contact with the surface.
The energy of the bond determines its lifetime and can be approximately computed with the Bell equation [67, p. 619]:

$$t_0 = \tau_0 \mathrm{e}^{-w_0/kT} \tag{2.19}$$

with the binding energy w_0 and the mean collision time τ_0. Since the lifetime increases exponentially with lower binding energy (by definition the binding energy for these interactions is negative), an energy of $50\,\mathrm{kT}$ may lead to a bond stable for years while $10\,\mathrm{kT}$ has a lifetime in the microsecond range [67, p. 601]. Under the assumption of additive effects, several weak interactions can therefore facilitate specific and reversible binding. Smaller molecules occupy less sites contributing to association, which generally results in lower binding affinity.

Receptor density and sensing area both decrease the minimum detectable concentration. Consequently, if the dissociation constant is high, higher receptor density can compensate that to a degree (Equation 2.18). The association constant, however, should be high to minimise the time to equilibrium (see Equation 2.9), as those receptor sites need to be filled. It is a compromise between high energy interactions that result in fast association but very long lifetime bonds and low energy binding which results in quickly regenerating surface but lower association constants and therefore a longer time to reach equilibrium.

2.2.3.3 Receptors and 2D Materials

Direct adsorption on the metal surface of the SPR sensor may lead to unwanted non-specific binding which translates to noise. Self-assembly of organic sulfide monolayers on gold allows reduction of such non-specific interactions by tailoring the sulfide towards the analyte matrix [68]. However, self-assembled monolayers (SAMs) can degrade over time depending on their end group functionalisation and the environment they are used in [69]. Polyethylene glycol (PEG) is another frequently used agent to block proteins from non-specific binding to the surface [70]. Carboxymethylated dextran hydrogel layers were popularised as early as 1990 and are still used in commercial systems. They can extend considerably into the volume of the evanescent field. The hydrogel itself is functionalised and the analyte diffuses into the hydrogel and binds to positions in the dextran layer [71]. Polymeric hydrogels have the benefit of high surface areas which means that more analyte can be immobilised in the sensitive volume of the sensor. However, as the analyte has to move through the dextran layer, the observed kinetics may be affected significantly by the movement

through the polymer.
The method of blocking non-specific binding depends on the analyte of interest and the expected interferences. For large analytes (cells, viruses, particles), large polymeric layers may be inappropriate. In a protein-rich matrix, PEG functionalisation may be the most efficient way of blocking their binding [72]. The blocked surface can be functionalised to allow specific association of the analyte molecule to the receptor surface. Antibodies, peptides, nucleotides, aptamers, and many more biomolecules can be immobilised using, e.g. the biotin-streptavidin interaction, EDC-NHS chemistry, and click chemistry [44, p. 240].

Within this work, primarily less specific interactions were employed. The principle of cross-reactive receptors was exploited in chapter 4, where an array of semi-specific interactions was used to create a "fingerprint" specific for the investigated analytes where several semi-selective receptors bind weakly to the analytes. This has the benefit of high reversibility of the surface due to less strong interactions but requires several different receptors.
The high surface to volume ratio, stability, functionalisation potential, and diverse interaction pathways of 2D materials have attracted increasing attention in the SPR community, particularly due to their ultrathin structure. Graphene as a prime example consists of sp^2 hybridised carbon with a long range conjugated π electron system. This π system allows for interactions (π-π, H-π, cation-π, anion-π) which are combinations of the effects mentioned above (electrostatic, Van der Waals and hydrogen bonds, [73]). Additionally, defects in graphene present more diverse interactions (H-bonding and electrostatic) and enable more specific modifications to the edges of the graphene flakes. Starting from graphene oxide (GO), which is a high-defect, negatively charged precursor for graphene, reduction leads to more pristine graphene with less defects and can be tuned with specific reduction agents to create functionalised GO (fGO) [74, 75]. In order to take advantage of the spatial detector used in SPRi, different functional groups have to be immobilised on the sensor surface. This can be done, e.g. by microstamping, using microfluidics, and with the help of microspotters [44, p. 244]. A selection of 2D materials was investigated for fabricating a receptor array with the help of a dispenser and tested against different plant oils in section B.1.3.

2.2.4 Modelling

Modelling the sensor response provides insight into the physical and chemical processes involved in the sensing mechanism, the foundation of which has been explored in section 2.2.1. Additionally, a model can significantly enhance confidence in measurement results which is important for any sensing application. This section discusses the parameters affecting a model for the reflectivity of the SPR sensor.

Tab. 2.1. Real and imaginary parts of the refractive index of gold from several sources, using simulation via Lorentz Drude (LD) modelling, and via an ellipsometric measurement (with data selected for 660 nm and 730 nm as indicated).

n(660)	k(660)	n(730)	k(730)	Au sample	Literature
0.149	3.746	0.127	4.4	thick film	[78]
0.169	3.876	0.153	4.56	53 nm on Si	[55]
0.154	3.642	0.119	4.3	44 nm on SiO_2	[79]
0.284	3.382	0.244	3.96	Lorentz Drude	[80]
0.53	3.207	0.519	3.76	53 nm	measured

2.2.4.1 Parameter contributions

SPR surface reflectivity depends on several parameters. These parameters can be categorised according to their variability in the context of a measurement: some parameters are fixed (refractive index of the prism), some parameters change across different sensor batches (thickness of the gold layer), while others are variable with time (temperature).
Given their importance, a brief introduction of the parameters involved in SPR signal generation is provided:

Refractive index of the prism: Two different glass types SF2 and N-SF6 (Schott, Germany) were used throughout this work. These glasses are characterised by the supplier. Their refractive index can be calculated dependent on the wavelength and temperature with the help of the temperature dependent Sellmeier equation (section A.2).

Refractive index of adhesive layer: Herein, chromium is used as an adhesive layer for gold. Sensors where the vapour deposition was performed by CreaVac (CreaVac, Germany), instead have a nickle-chromium alloy adhesive. The refractive index of this alloy is unknown, a range of refractive indices for chromium can be found in literature [76, 77].

Thickness of adhesive layer: The thickness of the adhesive layer should be as thin as possible due to the high imaginary part of the chromium-based material which dampens surface plasmon resonance. The thickness thus adversely affects the sensitivity of the sensor.

Refractive index of gold: The refractive index of thinly evaporated gold is not a fixed quantity. It depends on gold purity and evaporation parameters as well as the surface quality (see Table 2.1).

Thickness of gold: The thickness of the gold layer influences the resonator quality. An optimum thickness for a specific wavelength and fixed refractive index can be computed (see Figure 2.5) and is typically close to 50 nm.

Tab. 2.2. Change in parameters to alter reflectivity by the same amount as a 1×10^{-5} bulk refractive index change.

n_{Cr}	k_{Cr}	t_{Cr} nm	n_{Au} 1×10^{-3}	k_{Au} 1×10^{-3}	t_{Au} nm	n_{glass} 1×10^{-3}	λ nm	T K
−0.279	0.041	0.05	−0.646	−0.349	0.061	−0.014	−0.045	−0.096

Refractive index of the bulk medium: This is the dielectric medium in contact with the sensor surface. Within this work, mostly aqueous media are used which can be described by an empirical equation for water relating temperature, wavelength and refractive index [56].

Wavelength: The wavelength of light reflected from the SPR surface influences almost every parameter in the stack, making its effect more challenging to quantify directly. Here, only the effect on prism refractive index, metal refractive indices and dielectric medium is considered.

Temperature: The temperature affects refractive indices and the thickness of all layers. Since thickness changes are in the order of $1 \times 10^{-6}\,\%\,\mathrm{K}^{-1}$ for metals, they can be neglected. Refractive index changes due to temperature are only calculated for the prism and the dielectric material.

The reflectivity contributions of the parameters are compared as follows: pre-defined parameters are used to calculate the reflectivity, the reflectivity change generated by changing the bulk refractive index by 1×10^{-5} RIU is then determined. Finally, the equivalent change needed for every parameter to generate the same reflectivity change is computed. The result of this analysis is summarised in Table 2.2.
While any change in the refractive index and thickness of the metal layers alter the measured reflectivity significantly, these parameters do not change during a measurement within a limited time frame. However, the two parameters wavelength and temperature affect the refractive indices of every component and thus have to be stabilised. The temperature of the sensor is consequently controlled with the help of a thermoelectric cooler. The wavelength stability is specific to the employed light source. Typically, a wavelength filter is used to stabilise the output wavelength as the reflectivity change is the weighted integral of reflectivities of the filtered output spectrum. The LED specifications (section C.5) and wavelength filter transmission spectrum (Thorlabs FBH730-10) reduce the effect due to peak wavelength shift so that a variation of more than 1 nm is needed to alter the reflectivity significantly (at $\Delta\lambda_{\mathrm{peak}} \approx 0.1\,\mathrm{nm\,K}^{-1}$). To further minimise the impact of the LED wavelength variation, the LED was temperature controlled with a thermoelectric cooler.

2.2.4.2 Sensitivity towards analyte molecules

To estimate the signal deflection caused by an analyte molecule in solution in contact with an SPR sensor, the following approach can be used. In accordance with later

chapters, let us assume a small analyte molecule with $150\,\mathrm{g\,mol^{-1}}$ and a density of $1.6\,\mathrm{g\,L^{-1}}$. The bulk refractive index change can be approximated with the refractive index of its constituents (n_i) and the Lorenz-Lorentz equation [81, 82]:

$$\frac{n^2-1}{n^2+2} = \sum_i \Phi_i \frac{n_i^2-1}{n_i^2+2} \tag{2.20}$$

with the volume share

$$\Phi_i = \frac{V_i}{V}.$$

For organic molecules a refractive index of 1.6 was assumed ([48, 83]).
A bulk refractive index change of approximately 1×10^{-6} is calculated for a concentration of 50 µM of the small molecule which is not easily resolvable (for a 14-bit camera, compare Figure 2.10 a). A reliably resolvable change would be an order of magnitude higher, which can be achieved via a receptor element that increases the concentration of the analyte at the surface with respect to the volume concentration. When molecules are assumed spheric, with individual binding spots, and non-attaching to each other, the height of the binding layer can be approximated to

$$V_{\mathrm{molec}} = \frac{M}{\rho N_{\mathrm{A}}} \tag{2.21a}$$

$$h_{\mathrm{molec}} = \sqrt[3]{\frac{3V_{\mathrm{molec}}}{4\pi}} \tag{2.21b}$$

with binding layer density ρ and molecular mass M. Within this adsorption layer, a change in refractive index of close to 4×10^{-3} RIU (Figure 2.10 b) has to be generated to equal a bulk change of 1×10^{-5} RIU. This relates to a volume concentration of 2 % (solving Equation 2.20 for Φ_{analyte}) and, hence, a necessary receptor density of $4.7 \times 10^{12}\,\mathrm{cm^{-2}}$ (which is a high density of receptor spots [58]). The receptor density is:

$$b_{\mathrm{m}} = \frac{V_{\mathrm{s}} \Phi_{\mathrm{analyte}}}{A_{\mathrm{s}}}$$

with the surface volume V_{s} of the sensor in which molecules may adsorb and the sensor area A_{s}. This analysis illustrates, why SPR is more often used for larger molecules which induce a greater change in reflectivity or in combination with a hydrogel that fills a larger volume in which analyte molecules can agglomerate.
The approach to assume spherical molecules constituting an adsorbing layer reveals that it is almost equivalent to "dilute" an analyte within an adsorption layer by increasing the volume and adjusting the concentration within this layer (Figure 2.10 b).

Within this text, linearisation of the electric field was dismissed in favour of the more exact numerical approach. The consequence is that the resulting characteristics are harder to represent analytically. For a more analytical approach, the interested reader is referred to [84]. Modelling of the sensor response is discussed in more detail in chapter 3.

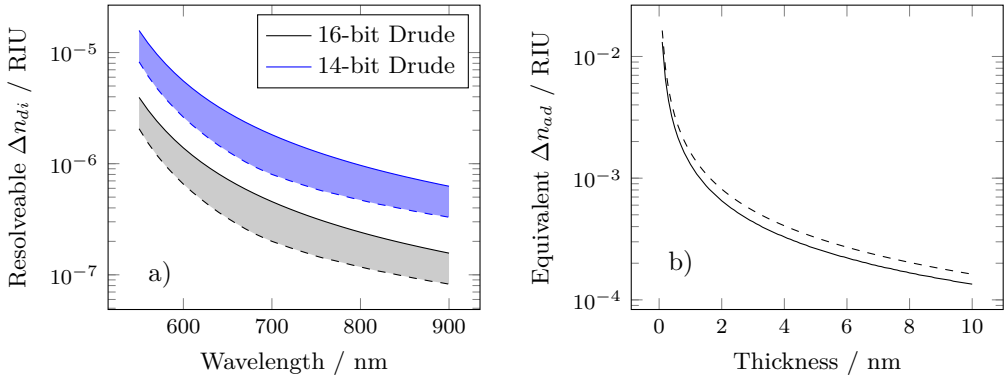

Fig. 2.10. Resolvable change in refractive index with a 14-bit and 16-bit detector (a). The shaded areas are bound by the sensitivity calculated with the parameters for gold according to the Lorentz-Drude model (solid) and after [55] (dashed) and represent the approximate range where the minimum resolvable change resides (for Schott SF2 glass and aqueous media). Note that neither the upper, nor the lower boundary should be understood as definite limits. In (b) the refractive index change needed to generate an equivalent reflectivity change as a bulk refractive index change of 1×10^{-5} RIU (solid line) is visualised when an adsorption layer with varying thickness is added instead. The dashed line represents the refractive index change caused by an adsorbate with fixed concentration when increasing the volume according to the thickness.

2.3 Conclusion

Within this chapter the necessary conditions for SPRi based on a prism-based setup and using widefield imaging were explored. Optimum conditions for sensitivity, lateral and refractive index resolution were surveyed. The importance of flow conditions and the impact of recognition elements towards analyte sensing was discussed. The sensitivity of the resonance condition due to changes close to the sensor surface was highlighted and it was shown that analytes have to be accumulated at the surface in order to resolve changes due to low molecular weight molecule adsorption. Additionally, the instrumental setup used throughout this work was characterised in terms of its intensity and lateral resolution. Dispensing of 2D materials was optimised with regards to layer thickness in the context of SPR imaging.

References

[1] A. Otto, “Excitation of Nonradiative Surface Plasma Waves in Silver by the Method of Frustrated Total Reflection”, *Zeitschrift für Physik A Hadrons and nuclei* **1968**, *216*, 398–410, DOI 10.1007/BF01391532 (cit. on p. 8).

[2] E. Kretschmann, H. Raether, "Notizen: Radiative Decay of Non Radiative Surface Plasmons Excited by Light", *Zeitschrift für Naturforschung A* **1968**, *23*, 2135–2136, DOI 10.1515/zna-1968-1247 (cit. on pp. 8, 11).

[3] R. Wood, "XLII. *On a Remarkable Case of Uneven Distribution of Light in a Diffraction Grating Spectrum*", *The London Edinburgh and Dublin Philosophical Magazine and Journal of Science* **1902**, *4*, 396–402, DOI 10.1080/14786440209462857 (cit. on p. 8).

[4] B. Liedberg, C. Nylander, I. Lunström, "Surface Plasmon Resonance for Gas Detection and Biosensing", *Sensors and Actuators* **1983**, *4*, 299–304, DOI 10.1016/0250-6874(83)85036-7 (cit. on p. 8).

[5] E. Yeatman, E. Ash, "Surface Plasmon Microscopy", *Electronics Letters* **1987**, *23*, 1091, DOI 10.1049/el:19870762 (cit. on p. 8).

[6] K.-F. Giebel, C. Bechinger, S. Herminghaus, M. Riedel, P. Leiderer, U. Weiland, M. Bastmeyer, "Imaging of Cell/Substrate Contacts of Living Cells with Surface Plasmon Resonance Microscopy", *Biophysical Journal* **1999**, *76*, 509–516, DOI 10.1016/S0006-3495(99)77219-X (cit. on p. 8).

[7] A. J. Thiel, A. G. Frutos, C. E. Jordan, R. M. Corn, L. M. Smith, "In Situ Surface Plasmon Resonance Imaging Detection of DNA Hybridization to Oligonucleotide Arrays on Gold Surfaces", *Analytical Chemistry* **1997**, *69*, 4948–4956, DOI 10.1021/ac9708001 (cit. on p. 8).

[8] L. Haeussling, H. Ringsdorf, F. J. Schmitt, W. Knoll, "Biotin-Functionalized Self-Assembled Monolayers on Gold: Surface Plasmon Optical Studies of Specific Recognition Reactions", *Langmuir* **1991**, *7*, 1837–1840, DOI 10.1021/la00057a001 (cit. on p. 8).

[9] S. Heyse, O. P. Ernst, Z. Dienes, K. P. Hofmann, H. Vogel, "Incorporation of Rhodopsin in Laterally Structured Supported Membranes: Observation of Transducin Activation with Spatially and Time-Resolved Surface Plasmon Resonance", *Biochemistry* **1998**, *37*, 507–522, DOI 10.1021/bi971564r (cit. on p. 8).

[10] M. Piliarik, J. Homola, "Self-Referencing SPR Imaging for Most Demanding High-Throughput Screening Applications", *Sensors and Actuators B: Chemical* **2008**, *134*, 353–355, DOI 10.1016/j.snb.2008.06.011 (cit. on p. 8).

[11] H. J. Lee, D. Nedelkov, R. M. Corn, "Surface Plasmon Resonance Imaging Measurements of Antibody Arrays for the Multiplexed Detection of Low Molecular Weight Protein Biomarkers", *Analytical Chemistry* **2006**, *78*, 6504–6510, DOI 10.1021/ac060881d (cit. on p. 8).

[12] J. A. Ruemmele, M. S. Golden, Y. Gao, E. M. Cornelius, M. E. Anderson, L. Postelnicu, R. M. Georgiadis, "Quantitative Surface Plasmon Resonance Imaging: A Simple Approach to Automated Angle Scanning", *Analytical Chemistry* **2008**, *80*, 4752–4756, DOI 10.1021/ac702544q (cit. on p. 8).

[13] Z. Liu, J. Wu, C. Cai, B. Yang, Z.-m. Qi, "Flexible Hyperspectral Surface Plasmon Resonance Microscopy", *Nature Communications* **2022**, *13*, 6475, DOI 10.1038/s41467-022-34196-7 (cit. on p. 8).

[14] P. Nikitin, A. Grigorenko, A. Beloglazov, M. Valeiko, A. Savchuk, O. Savchuk, G. Steiner, C. Kuhne, A. Huebner, R. Salzer, "Surface Plasmon Resonance Interferometry for Micro-Array Biosensing", *Sensors and Actuators A: Physical* **2000**, *85*, 189–193, DOI 10.1016/S0924-4247(00)00386-1 (cit. on p. 8).

[15] C.-Y. Han, C.-W. Luo, "An Ellipsometric Surface Plasmon Resonance System for Quantitatively Determining the Normal of a Sensor Surface and Multi-Channel Measurement", *Optics Communications* **2013**, *294*, 8–12, DOI 10.1016/j.optcom.2012.11.055 (cit. on p. 8).

[16] D. Wang, J. Loo, J. Chen, Y. Yam, S.-C. Chen, H. He, S. Kong, H. Ho, "Recent Advances in Surface Plasmon Resonance Imaging Sensors", *Sensors* **2019**, *19*, 1266, DOI 10.3390/s19061266 (cit. on p. 8).

[17] M. Bocková, J. Slabý, T. Špringer, J. Homola, "Advances in Surface Plasmon Resonance Imaging and Microscopy and Their Biological Applications", *Annual Review of Analytical Chemistry* **2019**, *12*, 151–176, DOI 10.1146/annurev-anchem-061318-115106 (cit. on p. 8).

[18] M. J. O'Brien, V. H. Pérez-Luna, S. Brueck, G. P. López, "A Surface Plasmon Resonance Array Biosensor Based on Spectroscopic Imaging", *Biosensors and Bioelectronics* **2001**, *16*, 97–108, DOI 10.1016/S0956-5663(00)00137-8 (cit. on p. 9).

[19] L. K. Wolf, D. E. Fullenkamp, R. M. Georgiadis, "Quantitative Angle-Resolved SPR Imaging of DNA-DNA and DNA-Drug Kinetics", *Journal of the American Chemical Society* **2005**, *127*, 17453–17459, DOI 10.1021/ja056422w (cit. on p. 9).

[20] G. D. VanWiggeren, M. A. Bynum, J. P. Ertel, S. Jefferson, K. M. Robotti, E. P. Thrush, D. M. Baney, K. P. Killeen, "A Novel Optical Method Providing for High-Sensitivity and High-Throughput Biomolecular Interaction Analysis", *Sensors and Actuators B: Chemical* **2007**, *127*, 341–349, DOI 10.1016/j.snb.2007.04.032 (cit. on p. 9).

[21] P. Zhang, L. Liu, Y. He, Z. Shen, J. Guo, Y. Ji, H. Ma, "Non-Scan and Real-Time Multichannel Angular Surface Plasmon Resonance Imaging Method", *Applied Optics* **2014**, *53*, 6037, DOI 10.1364/AO.53.006037 (cit. on p. 9).

[22] H. Kano, S. Mizuguchi, S. Kawata, "Excitation of Surface-Plasmon Polaritons by a Focused Laser Beam", *Journal of the Optical Society of America B* **1998**, *15*, 1381, DOI 10.1364/JOSAB.15.001381 (cit. on p. 9).

[23] B. Huang, F. Yu, R. N. Zare, "Surface Plasmon Resonance Imaging Using a High Numerical Aperture Microscope Objective", *Analytical Chemistry* **2007**, *79*, 2979–2983, DOI 10.1021/ac062284x (cit. on p. 9).

[24] H.-M. Tan, S. Pechprasarn, J. Zhang, M. C. Pitter, M. G. Somekh, "High Resolution Quantitative Angle-Scanning Widefield Surface Plasmon Microscopy", *Scientific Reports* **2016**, *6*, 20195, DOI 10.1038/srep20195 (cit. on p. 9).

[25] P. Zhang, G. Ma, W. Dong, Z. Wan, S. Wang, N. Tao, "Plasmonic Scattering Imaging of Single Proteins and Binding Kinetics", *Nature Methods* **2020**, *17*, 1010–1017, DOI 10.1038/s41592-020-0947-0 (cit. on p. 9).

[26] E. Fu, S. Ramsey, R. Thariani, P. Yager, "One-Dimensional Surface Plasmon Resonance Imaging System Using Wavelength Interrogation", *Review of Scientific Instruments* **2006**, *77*, 076106, DOI 10.1063/1.2227646 (cit. on p. 9).

[27] J. S. Yuk, H.-S. Kim, J.-W. Jung, S.-H. Jung, S.-J. Lee, W. J. Kim, J.-A. Han, Y.-M. Kim, K.-S. Ha, "Analysis of Protein Interactions on Protein Arrays by a Novel Spectral Surface Plasmon Resonance Imaging", *Biosensors and Bioelectronics* **2006**, *21*, 1521–1528, DOI 10.1016/j.bios.2005.07.009 (cit. on p. 9).

[28] Y. Zeng, L. Wang, S.-Y. Wu, J. He, J. Qu, X. Li, H.-P. Ho, D. Gu, B. Gao, Y. Shao, "Wavelength-Scanning SPR Imaging Sensors Based on an Acousto-Optic Tunable Filter and a White Light Laser", *Sensors* **2017**, *17*, 90, DOI 10.3390/s17010090 (cit. on p. 9).

[29] A. Sereda, J. Moreau, M. Canva, E. Maillart, "High Performance Multi-Spectral Interrogation for Surface Plasmon Resonance Imaging Sensors", *Biosensors and Bioelectronics* **2014**, *54*, 175–180, DOI 10.1016/j.bios.2013.10.049 (cit. on p. 9).

[30] S. Bak, G. H. Kim, H. Jang, J. Kim, J. Lee, C.-S. Kim, "Real-Time SPR Imaging Based on a Large Area Beam from a Wavelength-Swept Laser", *Optics Letters* **2018**, *43*, 5476, DOI 10.1364/OL.43.005476 (cit. on p. 9).

[31] Z. Liu, J. Wu, C. Cai, B. Yang, Z.-m. Qi, "Flexible Hyperspectral Surface Plasmon Resonance Microscopy", *Nature Communications* **2022**, *13*, 6475, DOI 10.1038/s41467-022-34196-7 (cit. on p. 9).

[32] P. Nikitin, A. Grigorenko, A. Beloglazov, M. Valeiko, A. Savchuk, O. Savchuk, G. Steiner, C. Kuhne, A. Huebner, R. Salzer, "Surface Plasmon Resonance Interferometry for Micro-Array Biosensing", *Sensors and Actuators A: Physical* **2000**, *85*, 189–193, DOI 10.1016/S0924-4247(00)00386-1 (cit. on p. 9).

[33] Y. Xinglong, W. Dingxin, W. Xing, D. Xiang, L. Wei, Z. Xinsheng, "A Surface Plasmon Resonance Imaging Interferometry for Protein Micro-Array Detection", *Sensors and Actuators B: Chemical* **2005**, *108*, 765–771, DOI 10.1016/j.snb.2004.12.089 (cit. on p. 10).

[34] T. R. Jensen, M. D. Malinsky, C. L. Haynes, R. P. Van Duyne, "Nanosphere Lithography: Tunable Localized Surface Plasmon Resonance Spectra of Silver Nanoparticles", *The Journal of Physical Chemistry B* **2000**, *104*, 10549–10556, DOI 10.1021/jp002435e (cit. on p. 10).

[35] A. Bonyár, "Label-Free Nucleic Acid Biosensing Using Nanomaterial-Based Localized Surface Plasmon Resonance Imaging: A Review", *ACS Applied Nano Materials* **2020**, *3*, 8506–8521, DOI 10.1021/acsanm.0c01457 (cit. on p. 10).

[36] J. M. Bingham, K. A. Willets, N. C. Shah, D. Q. Andrews, R. P. Van Duyne, "Localized Surface Plasmon Resonance Imaging: Simultaneous Single Nanoparticle Spectroscopy and Diffusional Dynamics", *The Journal of Physical Chemistry C* **2009**, *113*, 16839–16842, DOI 10.1021/jp907377h (cit. on p. 10).

[37] C. Campbell, G. Kim, "SPR Microscopy and Its Applications to High-Throughput Analyses of Biomolecular Binding Events and Their Kinetics", *Biomaterials* **2007**, *28*, 2380–2392, DOI 10.1016/j.biomaterials.2007.01.047 (cit. on pp. 10, 15).

[38] B. Wang, B. Park, "Immunoassay Biosensing of Foodborne Pathogens with Surface Plasmon Resonance Imaging: A Review", *Journal of Agricultural and Food Chemistry* **2020**, *68*, 12927–12939, DOI 10.1021/acs.jafc.0c02295 (cit. on p. 10).

[39] M. Puiu, C. Bala, "SPR and SPR Imaging: Recent Trends in Developing Nanodevices for Detection and Real-Time Monitoring of Biomolecular Events", *Sensors* **2016**, *16*, 870, DOI 10.3390/s16060870 (cit. on p. 10).

[40] E. Hecht, *Optics*, 5 ed/fifth edition, global edition, Pearson, Boston Columbus Indianapolis New York San Francisco Amsterdam Cape Town Dubai London Madrid Milan Munich, **2017** (cit. on p. 11).

[41] H. Raether, *Surface Plasmons on Smooth and Rough Surfaces and on Gratings*, Springer Berlin Heidelberg, Berlin, Heidelberg, **1988**, DOI 10.1007/BFb0048317 (cit. on p. 11).

[42] *Surface Plasmon Resonance Based Sensors*, (Ed.: J. Homola), Springer Berlin Heidelberg, Berlin, Heidelberg, **2006**, DOI 10.1007/b100321 (cit. on pp. 11, 18).

[43] S. A. Maier, *Plasmonics: Fundamentals and Applications*, Springer, New York, **2007** (cit. on p. 11).

[44] *Handbook of Surface Plasmon Resonance*, 2nd edition, (Ed.: R. B. M. Schasfoort), Royal Society of Chemistry, London, **2017** (cit. on pp. 11, 18, 23, 24).

[45] W. N. Hansen, "Electric Fields Produced by the Propagation of Plane Coherent Electromagnetic Radiation in a Stratified Medium", *Journal of the Optical Society of America* **1968**, *58*, 380, DOI 10.1364/JOSA.58.000380 (cit. on p. 12).

[46] M. Piliarik, J. Homola, "Surface Plasmon Resonance (SPR) Sensors: Approaching Their Limits?", *Optics Express* **2009**, *17*, 16505, DOI 10.1364/OE.17.016505 (cit. on p. 14).

[47] L. S. Jung, C. T. Campbell, T. M. Chinowsky, M. N. Mar, S. S. Yee, "Quantitative Interpretation of the Response of Surface Plasmon Resonance Sensors to Adsorbed Films", *Langmuir* **1998**, *14*, 5636–5648, DOI 10.1021/la971228b (cit. on p. 14).

[48] *Amino Acids and Serum Proteins*, (Ed.: J. A. Stekol), American Chemical Society, Washington, D.C., **1964**, DOI 10.1021/ba-1964-0044 (cit. on pp. 14, 27).

[49] H. J. Lee, T. T. Goodrich, R. M. Corn, "SPR Imaging Measurements of 1-D and 2-D DNA Microarrays Created from Microfluidic Channels on Gold Thin Films", *Analytical Chemistry* **2001**, *73*, 5525–5531, DOI 10.1021/ac010762s (cit. on p. 15).

[50] D. Boecker, A. Zybin, K. Niemax, C. Grunwald, V. M. Mirsky, "Noise Reduction by Multiple Referencing in Surface Plasmon Resonance Imaging", *Review of Scientific Instruments* **2008**, *79*, 023110, DOI 10.1063/1.2888527 (cit. on p. 15).

[51] M. Piliarik, M. Bocková, J. Homola, "Surface Plasmon Resonance Biosensor for Parallelized Detection of Protein Biomarkers in Diluted Blood Plasma", *Biosensors and Bioelectronics* **2010**, *26*, 1656–1661, DOI 10.1016/j.bios.2010.08.063 (cit. on p. 15).

[52] E. M. Yeatman, "Resolution and Sensitivity in Surface Plasmon Microscopy and Sensing", *Biosensors and Bioelectronics* **1996**, *11*, 635–649, DOI 10.1016/0956-5663(96)83298-2 (cit. on p. 15).

[53] C. E. H. Berger, R. P. H. Kooyman, J. Greve, "Resolution in Surface Plasmon Microscopy", *Review of Scientific Instruments* **1994**, *65*, 2829–2836, DOI 10.1063/1.1144623 (cit. on p. 15).

[54] L. Laplatine, L. Leroy, R. Calemczuk, D. Baganizi, P. N. Marche, Y. Roupioz, T. Livache, "Spatial Resolution in Prism-Based Surface Plasmon Resonance Microscopy", *Optics Express* **2014**, *22*, 22771, DOI 10.1364/OE.22.022771 (cit. on pp. 15–17).

[55] D. I. Yakubovsky, A. V. Arsenin, Y. V. Stebunov, D. Y. Fedyanin, V. S. Volkov, "Optical Constants and Structural Properties of Thin Gold Films", *Optics Express* **2017**, *25*, 25574, DOI 10.1364/OE.25.025574 (cit. on pp. 16, 25, 28).

[56] A. H. Harvey, J. S. Gallagher, J. M. H. L. Sengers, "Revised Formulation for the Refractive Index of Water and Steam as a Function of Wavelength, Temperature and Density", *Journal of Physical and Chemical Reference Data* **1998**, *27*, 761–774, DOI 10.1063/1.556029 (cit. on pp. 16, 26).

[57] E. Delamarche, B. Michel, H. A. Biebuyck, C. Gerber, "Golden Interfaces: The Surface of Self-Assembled Monolayers", *Advanced Materials* **1996**, *8*, 719–729, DOI 10.1002/adma.19960080903 (cit. on p. 18).

[58] T. M. Squires, R. J. Messinger, S. R. Manalis, "Making It Stick: Convection, Reaction and Diffusion in Surface-Based Biosensors", *Nature Biotechnology* **2008**, *26*, 417–426, DOI 10.1038/nbt1388 (cit. on pp. 18, 27).

[59] A. Saftics, S. Kurunczi, B. Peter, I. Szekacs, J. J. Ramsden, R. Horvath, "Data Evaluation for Surface-Sensitive Label-Free Methods to Obtain Real-Time Kinetic and Structural Information of Thin Films: A Practical Review with Related Software Packages", *Advances in Colloid and Interface Science* **2021**, *294*, 102431, DOI 10.1016/j.cis.2021.102431 (cit. on p. 18).

[60] P. Schuck, H. Zhao in *Surface Plasmon Resonance*, *Vol. 627*, (Eds.: N. J. Mol, M. J. E. Fischer), Humana Press, Totowa, NJ, **2010**, pp. 15–54, DOI 10.1007/978-1-60761-670-2_2 (cit. on pp. 18, 22).

[61] I. Langmuir, "The Adsoprtion of Gases on Plane Surfaces of Glass, Mica and Platinum.", *Journal of the American Chemical Society* **1918**, *40*, 1361–1403, DOI 10.1021/ja02242a004 (cit. on p. 18).

[62] V. G. Levič, V. G. Levič, *Physicochemical Hydrodynamics*, 2. ed., Prentice-Hall, Englewood Cliffs, NJ, **1962** (cit. on p. 21).

[63] S. Sjoelander, C. Urbaniczky, "Integrated Fluid Handling System for Biomolecular Interaction Analysis", *Analytical Chemistry* **1991**, *63*, 2338–2345, DOI 10.1021/ac00020a025 (cit. on p. 21).

[64] R. L. Rich, D. G. Myszka, "Survey of the Year 2007 Commercial Optical Biosensor Literature", *Journal of Molecular Recognition* **2008**, *21*, 355–400, DOI 10.1002/jmr.928 (cit. on p. 22).

[65] R. L. Rich, D. G. Myszka, "Survey of the 2009 Commercial Optical Biosensor Literature", *Journal of Molecular Recognition* **2011**, *24*, 892–914, DOI 10.1002/jmr.1138 (cit. on p. 22).

[66] H.-J. Butt, K. Graf, M. Kappl, *Physics and Chemistry of Interfaces*, Wiley-VCH, Weinheim, **2003** (cit. on p. 23).

[67] J. N. Israelachvili, *Intermolecular and Surface Forces*, 3rd ed, Academic press, Burlington (Mass.), **2011** (cit. on p. 23).

[68] R. G. Nuzzo, D. L. Allara, "Adsorption of Bifunctional Organic Disulfides on Gold Surfaces", *Journal of the American Chemical Society* **1983**, *105*, 4481–4483, DOI 10.1021/ja00351a063 (cit. on p. 23).

[69] C. Vericat, M. E. Vela, G. Benitez, P. Carro, R. C. Salvarezza, "Self-Assembled Monolayers of Thiols and Dithiols on Gold: New Challenges for a Well-Known System", *Chemical Society Reviews* **2010**, *39*, 1805–1834, DOI 10.1039/B907301A (cit. on p. 23).

[70] H. B. Lu, C. T. Campbell, D. G. Castner, "Attachment of Functionalized Poly(Ethylene Glycol) Films to Gold Surfaces", *Langmuir* **2000**, *16*, 1711–1718, DOI 10.1021/la990221m (cit. on p. 23).

[71] S. Löfås, B. Johnsson, "A Novel Hydrogel Matrix on Gold Surfaces in Surface Plasmon Resonance Sensors for Fast and Efficient Covalent Immobilization of Ligands", *J. Chem. Soc. Chem. Commun.* **1990**, 1526–1528, DOI 10.1039/C39900001526 (cit. on p. 23).

[72] E. Wijaya, C. Lenaerts, S. Maricot, J. Hastanin, S. Habraken, J.-P. Vilcot, R. Boukherroub, S. Szunerits, "Surface Plasmon Resonance-Based Biosensors: From the Development of Different SPR Structures to Novel Surface Functionalization Strategies", *Current Opinion in Solid State and Materials Science* **2011**, *15*, 208–224, DOI 10.1016/j.cossms.2011.05.001 (cit. on p. 24).

[73] C. A. Hunter, J. K. M. Sanders, "The Nature of .Pi.-.Pi. Interactions", *Journal of the American Chemical Society* **1990**, *112*, 5525–5534, DOI 10.1021/ja00170a016 (cit. on p. 24).

[74] *Functionalization of Graphene*, (Ed.: B. Geōrgakilas), Wiley-VCH, Weinheim, **2014** (cit. on p. 24).

[75] C. Anichini, W. Czepa, D. Pakulski, A. Aliprandi, A. Ciesielski, P. Samorì, "Chemical Sensing with 2D Materials", *Chemical Society Reviews* **2018**, *47*, 4860–4908, DOI 10.1039/C8CS00417J (cit. on p. 24).

[76] V. Lozanova, A. Lalova, L. Soserov, R. Todorov, "Optical and Electrical Properties of Very Thin Chromium Films for Optoelectronic Devices", *Journal of Physics: Conference Series* **2014**, *514*, 012003, DOI 10.1088/1742-6596/514/1/012003 (cit. on p. 25).

[77] A. Sytchkova, A. Belosludtsev, L. Volosevičienė, R. Juškėnas, R. Simniškis, "Optical, Structural and Electrical Properties of Sputtered Ultrathin Chromium Films", *Optical Materials* **2021**, *121*, 111530, DOI 10.1016/j.optmat.2021.111530 (cit. on p. 25).

[78] R. L. Olmon, B. Slovick, T. W. Johnson, D. Shelton, S.-H. Oh, G. D. Boreman, M. B. Raschke, "Optical Dielectric Function of Gold", *Physical Review B* **2012**, *86*, 235147, DOI 10.1103/PhysRevB.86.235147 (cit. on p. 25).

[79] G. Rosenblatt, B. Simkhovich, G. Bartal, M. Orenstein, "Nonmodal Plasmonics: Controlling the Forced Optical Response of Nanostructures", *Physical Review X* **2020**, *10*, 011071, DOI 10.1103/PhysRevX.10.011071 (cit. on p. 25).

[80] A. D. Rakić, A. B. Djurišić, J. M. Elazar, M. L. Majewski, "Optical Properties of Metallic Films for Vertical-Cavity Optoelectronic Devices", *Applied Optics* **1998**, *37*, 5271, DOI 10.1364/AO.37.005271 (cit. on p. 25).

[81] H. Lorentz, *The Theory of Electrons and Its Applications to the Phenomena of Light and Radiant Heat*, 2nd edition, B.G. Teubner, New York, **1916** (cit. on p. 27).

[82] N. An, B. Zhuang, M. Li, Y. Lu, Z.-G. Wang, "Combined Theoretical and Experimental Study of Refractive Indices of Water–Acetonitrile–Salt Systems", *The Journal of Physical Chemistry B* **2015**, *119*, 10701–10709, DOI 10.1021/acs.jpcb.5b05433 (cit. on p. 27).

[83] E. T. Arakawa, L. C. Emerson, S. I. Juan, J. C. Ashley, M. W. Williams, "The Optical Properties of Adenine from 1.8 to 80 eV", *Photochemistry and Photobiology* **1986**, *44*, 349–353, DOI 10.1111/j.1751-1097.1986.tb04674.x (cit. on p. 27).

[84] E. M. Yeatman, "Resolution and Sensitivity in Surface Plasmon Microscopy and Sensing", *Biosensors and Bioelectronics* **1996**, *11*, 635–649, DOI 10.1016/0956-5663(96)83298-2 (cit. on p. 27).

Chapter 3

Utilising Spatial Angle Modulation for Surface Plasmon Resonance Imaging

Surface Plasmon Resonance is a sensitive, label-free detection method for biosensors but suffers from cross-sensitivities due to signal contributions from the evanescent field that penetrates several hundred nanometres into the probed medium. This results in a signal that is not only altered upon adsorption of target analytes but also due to components in the matrix changing with time and experimental conditions. Herein, a method to utilise a two-dimensional sensor by projecting non-collimated light onto the sensor surface resulting in the modulation of the incidence angle across the surface is presented. This angular modulation can be used to extract additional information of the layer composition of the sensor and allows to distinguish changes in reflectivity due to adsorption from bulk refractive index induced changes.

3.1 Introduction

Two-dimensional surface plasmon resonance (SPR) sensors can be utilised to encode additional information on either axis. Spatial frequencies modulated through varying the incidence angle have been identified as one useful component [1]. This angular information can be used to determine the parameters of the plasmonic surface [2], as well as the refractive index and thickness of adsorbates [3].
While the modulation is mostly achieved by scanning the angle, some researchers have projected the angle onto the imager. Liu et al. [4] have used angular information to optimise illumination of their sensor with the conclusion that a wavelength-filtered LED (light-emitting diode) light source provides the best signal-to-noise ratio. The same group optimised their setup with regards to angular spread that is projected onto the sensor surface [5]. They applied a series of polynomial fits to approximate the SPR curve and track the resonance minimum for biosensing after calibration. Alternatively, minimum tracking can also be done by calculating the polynomial fit centroid [6].
Angular modulation by projecting a divergent light source onto the surface offers the advantage of time-resolved angular measurements, since for every time step a spectrum can be acquired. The recorded spectra can be used for further data processing. In this text methods to use the angular modulation for direct physical modelling are explored. This approach enables the prediction of SPR sensor parameters and additionally can be used to distinguish adsorption of analytes from bulk refractive index changes. The term multi-parametric surface plasmon resonance imaging (MP-SPRi) is used to reflect the utilisation of the entire imaged angular spectrum and fitting of multiple parameters.

3.2 Theory and Methods

In Figure 3.1 the concept of MP-SPRi is illustrated. With angular modulation of the input light and structuring of the sensor surface, a multitude of different response curves can be observed with a change in analyte which ultimately allows for

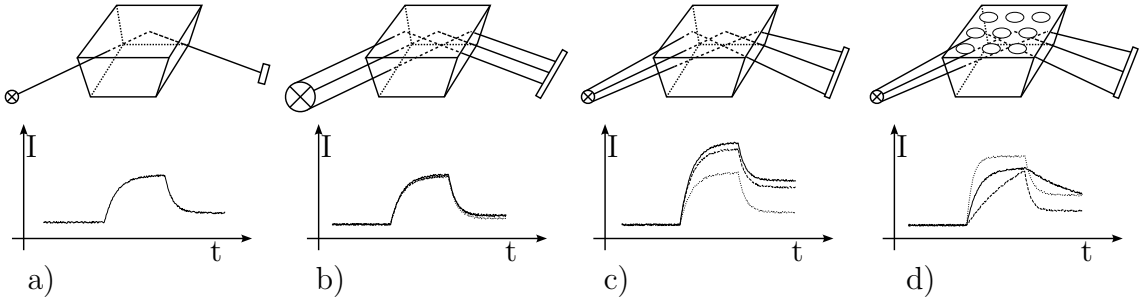

Fig. 3.1. SPR can be observed on a single spot with a single detector (a). Imaging provides redundancy and elimination of correlated noise when a surface is observed simultaneously (b). Through angular modulation of the input light, different sensitivities for the sensor surface can be achieved (c). Using recognition elements, a specific response towards an analyte can be observed (d). Every step can be seen as an information increase.

discrimination of sensor states. The application of angular modulation (Figure 3.1 c) is explored within this chapter.

3.2.1 Transfer-Matrix Method

For the theoretical calculations throughout this work, a python module to compute the reflection was developed. It was specifically written for Kretzschmann-Raether type SPR and includes the calculation of the incident angle on the plasmonic surface due to refraction at the prism and reflection of light on the air-glass interface. It was tested against the popular software WinSpall*. Since the module can be used within Python, more flexible calculations are possible.

The transfer-matrix method is used to calculate reflectivities of multi-layer structures by exploiting the continuity conditions of the boundaries between layers. Homogeneous, isotropic layers between semi-infinite phases are assumed where the initial phase (n_1) shall be transparent resulting in a real refractive index. Additionally, the relative permeability of the materials shall be unity [7]. The presented equations are also restricted to p-polarised light.
The transfer matrix (M) relating the electric and magnetic fields of the input to the output of the SPR stack with N layers where the first and last layer are semi-infinite is [8]

$$\begin{pmatrix} H_{y1} \\ E_{x1} \end{pmatrix} = M \begin{pmatrix} H_{y(N-1)} \\ E_{x(N-1)} \end{pmatrix}. \tag{3.1}$$

The transfer matrix is the product of the transfer matrices of the layer interfaces

$$M = \prod_{k=2}^{N-1} M_k = \begin{pmatrix} M_{11} & M_{12} \\ M_{21} & M_{22} \end{pmatrix} \tag{3.2}$$

*`http://www.res-tec.de/downloads.html`

with

$$M_{k,p} = \begin{pmatrix} \cos\beta_k & -i/q_k \sin\beta_k \\ -iq_k \sin\beta_k & \cos\beta_k \end{pmatrix} \tag{3.3}$$

and q_k can be calculated with the help of

$$q_k = \frac{\sqrt{\hat{\epsilon}_k - n_1^2 \sin^2\theta_1}}{\hat{\epsilon}_k}. \tag{3.4}$$

For s-polarised light, q_k has to be multiplied by $\hat{\epsilon}_k^2$. β_k is the phase factor of the wave in the material (Equation 2.1) and is defined by (see also Equation 2.2)

$$\beta_k = d_k \cdot k_{z,k} = \frac{2\pi d_k}{\lambda}\sqrt{\hat{\epsilon}_k - n_1^2 \sin^2\theta_1}. \tag{3.5}$$

The reflectivity can be calculated by relating the amplitudes of the reflected to the input field (refer to Equation 3.1):

$$R_p = |r_p|^2 = \left|\frac{(M_{11} + M_{12}q_N)q_1 - (M_{21} + M_{22}q_N)}{(M_{11} + M_{12}q_N)q_1 + (M_{21} + M_{22}q_N)}\right|^2. \tag{3.6}$$

This formalism allows for fast computation of arbitrary stacks of layers.

3.2.2 SPRi Modelling

For imaging this definition needs to be extended to two dimensions. The approximate theoretical propagation length of surface plasmons on gold is approximately 10 µm (see Figure 2.5), although for a real system higher refraction due to imperfections of the gold layer is expected which, in praxis, reduces the propagation length. The employed camera utilises a Sony IMX178 CCD chip (section C.3), which is a 1/1.8" (7.2 mm x 5.4 mm) sensor and is paired with an objective lens (section C.4). The SPR prism surface size is 18 mm x 18 mm and the required depth of focus due to the viewing angle at around 62° is close to 20 mm. This results in a high required f/D to maintain the depth of focus which reduces the lateral resolution. The diffraction-limited resolution of the setup (camera and lens aperture and distance to object) is approximately 15 µm which is further reduced by the lens properties (and the application of magnifiers or a higher back focal length to increase magnification). The resulting primary magnification of the setup together with the pixel size implies an object space resolution of 10 µm per pixel in the direction perpendicular to the incident plane and roughly twice that in the direction parallel to the incident plane. The optical PSF and the object space resolution are similar in scale to the propagation length of the surface plasmon. In praxis, the PSF is expected to be higher than anticipated while the propagation length is lower due to non-zero surface roughness. As the observations can be averaged over at least two pixels in either dimension, the observations are thus assumed to be independent.
The reflected intensity of an SPRi system can then generally be written as

$$I_{\mathrm{r},t}(x, y, t) = I_{0,t}(x, y, t) \cdot R_t(x, y, t) \tag{3.7}$$

with the spatiotemporal input intensity I_0 and the reflectivity of the surface R. The input intensity is subject to noise ($I_0 = I_{0,\text{source}} + \sigma_{\text{source}}$) and is captured with a camera. The camera can be assumed an approximately linear transducer, giving

$$I_{\text{c},t}(x, y, t) = S_\text{c}(I_{0,t}(x, y, t) \cdot R_t(x, y, t)) + I_{\text{c,dark}} + \sigma_{\text{camera}} \tag{3.8}$$

with the camera sensitivity S_c, the dark current of the camera ($I_{\text{c,dark}}$) and its noise (σ_{camera}). Temporal averaging can be used to reduce the influence of noise and dark current can be determined so it can be approximated to

$$I_\text{c}(x, y) \approx I_0(x, y) \cdot R(x, y) \tag{3.9}$$

by introducing the temporal averages $I_\text{c} = \overline{I_{\text{c},t}}$, $I_0 = \overline{I_{0,t}}$ and $R = \overline{R_t}$.

3.2.2.1 Determining SPRi parameters

Modulating the input angle Φ, an intensity sequence which relates to every angular position can be generated

$$I_\text{c}(x, y, \Phi) \propto I_0(x, y, \Phi) \cdot R(x, y, \Phi). \tag{3.10}$$

This can be used together with the s-polarisation to eliminate the input intensity under the assumption of negligible (or previously subtracted) dark current and noise to

$$\frac{I_{\text{c,p}}(x, y, \Phi)}{I_{\text{c,s}}(x, y, \Phi)} = \frac{R_\text{p}(x, y, \Phi)}{R_\text{s}(x, y, \Phi)}. \tag{3.11}$$

The parameters that describe the SPR surface are the refractive indices and thicknesses of the layers that constitute the sensor surface. These can now be determined by optimising the set of parameters P that satisfy:

$$\min \left(\frac{I_{\text{c,p}}(x, y, \Phi)}{I_{\text{c,s}}(x, y, \Phi)} - \frac{R_\text{p}(x, y, \Phi, P)}{R_\text{s}(x, y, \Phi, P)} \right). \tag{3.12}$$

Although it was shown that such an optimisation problem is ill-posed for determining both thickness and refractive index of layers [9], a stable minimum can be found when using multiple wavelengths or refractive indices for calculation.
Another means to find the parameter set P is available by using the lateral dimensions of the sensor surface. Modulating the refractive index across the surface is possible with a separated flow cell which has been explored for example in [10]. Alternatively, the incidence angle can be modulated across the surface by using a slightly decollimated light source. This leads to a small variation of the incidence angle in one direction (along the xz-plane as indicated in Figure 3.2) which means that the angle distribution becomes a function of the surface position $\Phi = f(x, y)$. Note that the coordinate system for the surface angle distribution has its origin on the sensor surface (inner angle) while the coordinate system used for the description in Figure 3.2 has its origin on the prism entry face (outer angle).

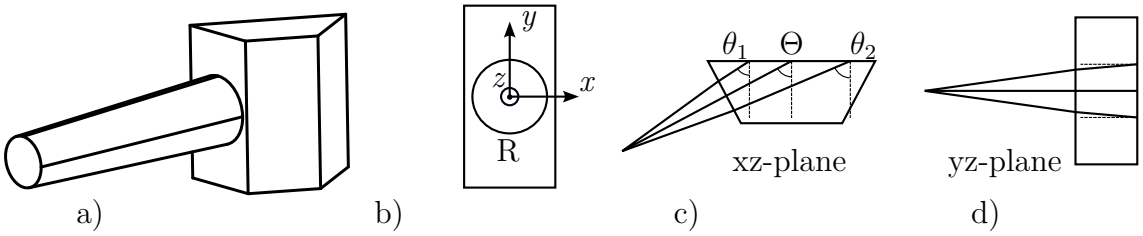

Fig. 3.2. A slightly divergent point light source which illuminates a prism far away from the source (a) exhibits an approximately linear angular dependency across its illumination radius R (b). In the xz-plane a range of angles on the SPR surface can be observed that is approximately linear for small angles, here $\theta_1 < \Theta < \theta_2$ and Θ is identical to the prism angle (c). In the yz-plane, small deviations from vertical illumination can be observed (d) which barely affect the SPR response.

The outer angle and the inner angle are related via

$$\Phi_{\text{inner}} = \arcsin\left(\frac{n_{\text{air}}}{n_{\text{prism}}}\sin\left(\Phi_{\text{outer}} - \Theta\right)\right) + \Theta \tag{3.13}$$

with the prism base angle Θ, the refractive index of air ($n_{\text{air}} \approx 1$), and the prism refractive index n_{prism}. The mapping of the outer angular function ($\Phi_{\text{outer}}(x_{\text{o}}, y_{\text{o}})$) to the inner angular function ($\Phi_{\text{inner}}(x_i, y_i)$) further depends on the dimensions of the prism and is defined by a homographic projection of the prism incidence surface to the sensitive surface. The projection (scaling due to the steeper or more shallow angles the surface is viewed under, translation and rotation due to imperfect alignment) for every image in the stack onto the prism base angle image can be calculated and the images may be adjusted accordingly.
Since the outer angular distribution can be assumed constant around its centre angle Φ_0 even when adjusting the centre incidence angle, the projected angular distribution onto the sensor surface was incorporated into the model (Equation 3.12) to

$$\min\left(\frac{I_{\text{c,p}}(x, y, \Phi)}{I_{\text{c,s}}(x, y, \Phi)} - \frac{R_{\text{p}}(\Phi_{\text{outer}}(x, y), P)}{R_{\text{s}}(\Phi_{\text{outer}}(x, y), P)}\right) \tag{3.14}$$

which together with Equation 3.13 gives the angle distribution on the sensor surface. For small angles, the angular distribution on the prism entry surface can be assumed linear with respect to x and y. Additionally, the projection onto the prism surface can be assumed linear. From Figure 3.2 d, it can also be seen that the y-dependency can be neglected. To minimise potential errors, $\Phi(x, y)$ was modelled as a two-dimensional polynomial of second order. The polynomial parameters can be optimised together with the surface parameters (metal refractive indices and thicknesses) or sequentially. It is, however, advisable to provide a sensible initial guess when trying to optimise both sets simultaneously.

In Figure 3.3 the mapping of position and angle is presented. The sensor surface was cropped to the area that is neither perturbed by the sealing (bright vertical stripes) or the limited FOV due to the aperture (semicircle borders top and bottom). In

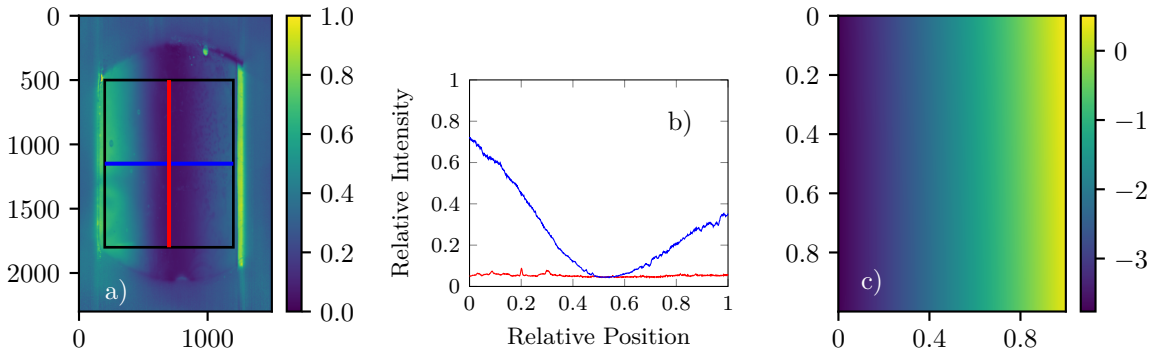

Fig. 3.3. Ratio between p and s-polarised images at 61° with indicated selection of the middle area of the sensor surface and two cuts (a). Intensities along the direction of angular spread (blue) and perpendicular to that (red) (b). Angular deviation from the configured outer angle across the surface (c), the distribution suggests a slight tilt of the prism relative to the optical axis, as zero deviation is not centred.

the z-direction (compare Figure 3.2), a section of the SPR curve can be observed (see Figure 3.3 b). In the y-direction no position-dependent intensity change was observed (red curve). The angular deviation to the set incidence angle was modelled as a two-dimensional second order polynomial as visualised in Figure 3.3 c.
With an entire surface of varying incidence angles (Figure 3.3 c), a host of SPR curves can be recorded at once by scanning the incidence angle. This allows for accurate determination of the surface parameters with just a single refractive index and wavelength. The magnification of the optical system results in an imaged sensor that spans more than 1300x1000 pixels (Figure 3.3 a). It is sufficient to select a subset of curves from the surface to achieve adequate accuracies for the parameter determination. In this case 130 (13x10) curves spaced evenly across the surface were selected (a less tight grid can be used without changing the result significantly but the two-dimensional angle function will be less well defined).

For calibration of the sensor surface, several measurements were performed. SPR images were collected using the setup described in section B.2. Outer angles were varied between 55° and 70° for s- and p-polarised illumination. Images were aligned to 61° via homographic projection with the homography matrix calculated with the data collected under s-polarisation. Angle scan data was acquired in three-fold replicates for water (Millipore, 18.21 Ω cm, 3 ppb total organic compound), ethanol (Merck Millipore EMPARTA $\geq$ 99.5 %) and 2-propanol (Merck Millipore EMSURE $\geq$ 99.8 %).
Data was either extracted from the images as an average over a defined region of interest extending over 10x20 pixels, or taken from points in a grid over the entire surface where every point is just a single pixel.
Extracted data was fit to the model using the minimisation criterium defined in Equation 3.12 for data averaged over a region of the image or Equation 3.14 when taking data from the entire sensor surface with the help of the Levenberg-Marquardt

Tab. 3.1. Fit initial values used for parameter optimisation with the Levenberg-Marquardt algorithm. Values based on Lorentz Drude modelling.

Bounds	n_{nicr}	k_{nicr}	t_{nicr}	n_{au}	k_{au}	t_{au}
init	3.91	4.34	$2 \cdot 10^{-9}$	0.24	3.96	$4.8 \cdot 10^{-8}$
min	1	0.3	$1 \cdot 10^{-9}$	0.1	2	$4.6 \cdot 10^{-8}$
max	6	6	$1 \cdot 10^{-8}$	0.75	5	$5.5 \cdot 10^{-8}$

algorithm using least squares loss. The initial parameter values are presented in Table 3.1. The optimised values from a set of initial values and boundaries were then used to explore the parameter space by drawing from their posterior probability distribution using a Markov-Chain Monte Carlo (MCMC) based algorithm [11]. MCMC optimisation was performed with uniform priors, maintaining the ranges from the initial parameter set.

3.2.2.2 Disentangling refractive index change contributions

In an SPR sensor the refractive index of the dielectric and the thickness of an adsorbed layer or amount of an adsorbate can change simultaneously. A system that relies on intensity monitoring of a homogeneous surface cannot discriminate the two changing parameters. This is where the angular distribution across a sensor surface becomes relevant. With the help of angular information, the effects of bulk refractive index changes and adsorption can be disentangled which allows more precise determination of the composition of a medium [12].
With angular information including the angle of total internal reflection, this is a rather simple task, since the TIR angle is unaffected by an adsorption layer with nanometer size while a bulk refractive index change significantly alters it (Figure 2.4). The TIR angle is about 10° from the resonance angle which means that an accurate angle scanning device has to be available and image matching of the deformed images that get scaled due to the viewing angle has to applied.
As an alternative, it can be shown that a smaller section from the angular response is sufficient to discriminate the two effects. With a calibrated sensor surface, i.e. a defined parameter set P, the input intensity distribution can now be calculated, e.g. by employing any of the polarisations (s and p) and their respective known reflectivities (under the assumption of negligible noise and dark current):

$$I_{\mathrm{c,p}}(x, y) \propto I_0(x, y) \cdot R_{\mathrm{p}} \tag{3.15a}$$

$$I_{\mathrm{c,s}}(x, y) \propto I_0(x, y) \cdot R_{\mathrm{s}} \tag{3.15b}$$

It is, however, again advisable to find a function $I_{f0}(x, y)$ for the input intensity. A two-dimensional Gaussian as a reasonable guess was chosen to model the intensity distribution.
With known parameter sets P and incident intensity I_0 it is possible to model a camera image for every time step in a measurement sequence where the analyte

varies with time. It is then straightforward to directly predict the refractive index of the dielectric or the adsorption layer, respectively. For that, the set of refractive indices that satisfy:

$$\min\left(I_{\mathrm{c,p}}(x,y,t) - R_{\mathrm{p}}(x,y,P_{\mathrm{fixed}},P_n(t)) \cdot I_{f0}(x,y)\right) \tag{3.16}$$

are optimised, where the parameter set P_{fixed} are the parameters related to the sensor surface found previously and $P_n(t)$ are the varying refractive indices of the dielectric or a bound layer of molecules.
As a proof of concept, a single SPR curve for three different conditions (with the changes in refractive index of the adsorption layer and the dielectric Δn_{ad} and Δn_{di}, respectively) was modelled:

1. $\Delta n_{\mathrm{ad}} = 0$, $\Delta n_{\mathrm{di}} = 0$
2. $\Delta n_{\mathrm{ad}} = 0$, $\Delta n_{\mathrm{di}} = \Delta n_{\mathrm{di},2} > 0$
3. $\Delta n_{\mathrm{ad}} = \Delta n_{\mathrm{ad},3} > 0$, $\Delta n_{\mathrm{di}} = 0$

Although, in this case, the refractive index of the adsorption layer was chosen as a parameter, its thickness can be evaluated equivalently (see also section 2.2.4.1). The change in refractive index of the adsorption layer ($\Delta n_{\mathrm{ad},3}$) was chosen somewhat arbitrary to be 1×10^{-3} RIU at a thickness of 2 nm. The change in refractive index of the dielectric ($\Delta n_{\mathrm{di},2}$) was chosen so it generates the same change of reflectivity at the angle of maximum sensitivity towards condition 1 as condition 3 (here approximately 1.5553×10^{-5} RIU which is coincidentally a change that can be comfortably resolved with a 14-bit camera where unity reflectivity is equivalent to full scale). The generated SPR curve was evaluated in two different angular ranges: from 45° to 65° and from 57° to 61° (compare Figure 3.3 c). The generated curves (see Figure 3.4) were fit to the SPR curve function subject to the parameters Δn_{ad} and Δn_{di} (compare Equation 3.16).
Additionally, the curve was fit using the smaller angle selection but with 13 repeats to emulate the use of a spatial sensor with the angular distribution found during previous optimisation. Gaussian noise was added to the data in the magnitude of one digit of a 14-bit camera (Figure B1) and the fit result was recorded over 100 repeats.

3.2.3 Data-based Modelling

In contrast to explicitly modelling a specific dependency like shown above, it is also possible to employ data-based models to evaluate sensor responses. It was shown that neural networks with hidden layers and a sufficient amount of neurons can approximate any function (to any desired accuracy) [13]. This implies that the dependencies illustrated above may be inferred from data which has the advantage of preventing inaccuracies in the physical model describing the sensor.

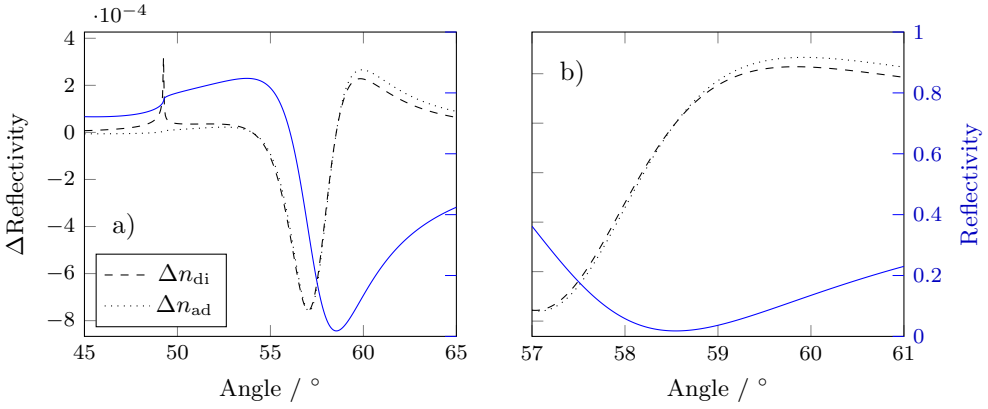

Fig. 3.4. Change in reflectivity due to a change in bulk refractive index or a change of the adsorption layer for the full simulated angular range (a) and a reduced range that can be projected onto the sensor surface (b). A change in bulk refractive index results in a strong change at the angle of total internal reflection. In the reduced angular range the differences between the two changes are very subtle.

There are several assumptions made during the modelling approach detailed above which are merely approximations of the underlying physical system:

- the sensor surface is homogeneous
- plasmons are laterally independent
- the layers on the sensor surface are isotropic
- incident light is perfectly monochromatic
- incident light is perfectly polarised
- incident intensity for both polarisations is identical
- optical aberrations are temporally stable

While these approximations have been heuristically shown to be adequate, their behaviour may change in yet untested conditions.
It is also computationally intensive to calculate the Fresnel equations for an entire image. This motivates the use of data-driven methods as an unbiased, efficient, and powerful method for analysis.

3.2.3.1 Feature extraction

Current CCD cameras produce images with megapixel resolution where every pixel holds information on the measurement. The high dimensionality of the data can

cause problems, as calculations require more resources, the importance of specific pixels becomes difficult to manage and distance metrics between points in high dimensions are very small which makes it hard to computationally differentiate data points [14, p. 152]. To reduce dimensionality, derived values can be extracted from the image data. These so-called features can be obtained via different means and can be categorised into expert-based and trainable feature extraction.
The former involves the segmentation of specific regions of interest which correspond to functional areas like receptors or reference structures. These values can then be directly used in a sub-sequent model or processed further, e.g. by calculating average intensities of these areas. This approach has the benefit that the features used for further processing are easily interpretable but it requires the scientist to know which areas contribute to solving the analytical task.
Trainable feature extraction, on the other hand, utilises data-driven models that transform the input data onto different axes and allow for reduction of unimportant features (e.g. principal component analysis - PCA), methods that extract subsets of the input (e.g. segmentation), or deep learning models (e.g. convolutional neural networks - CNN). Image data is very specific in a sense that it consists of spatially correlated data. This property is used within convolutional neural networks, which are translation equivariant which means a feature moving laterally in an image will produce the same output magnitude after convolution. Pooling also makes the feature space invariant to small lateral shifts [14, pp. 334, 336]. This rather weak bias proves to be enough for CNNs to have become the de-facto standard for image classification. In an SPRi setup the role of a feature extractor would be to extract parameters related to the refractive indices at certain functional areas which then allow determination of an analyte or its abundance. Since the functional areas are distributed across the sensor surface but similar functional groups are expected to be close to each other, feature extraction can exploit spatial correlation of functionality. Trainable and expert-based feature extraction can be combined, by manually selecting valid patches from an image and then utilising a latent representation algorithm to further reduce features [15]. Alternatively, automatic segmentation with a pre-trained algorithm may be used [16] to extract data from the detected regions which can then be processed further using, e.g. average intensities, statistical information, or histograms of the segmented spots.

3.2.3.2 Models

After feature extraction a suitable machine learning model has to be selected for the analytical task, i.e. finding analytes or their abundances, discriminating analytes, or finding anomalies in observed patterns. In deep learning this is most commonly a multi-layer perceptron (MLP) parametrised by weights ($\mathbf{W}$) and biases ($\mathbf{b}$) as well as their activation functions (σ) for each layer:

$$f_l(\mathbf{x}; \mathbf{W}, \mathbf{b}) = \sigma\left(\mathbf{x}\mathbf{W}^T + \mathbf{b}\right). \tag{3.17}$$

The input of each layer is the output of its subsequent layer. The activation function is a non-linear function (most commonly a sigmoid function, rectified linear unit, or

variants of the two [17, p. 392]).
The feature extraction methods and a suitable MLP head can be combined to different architectures briefly sketched in Figure 3.5. The models presented in this diagram have all been employed experimentally using the data presented in chapter 4 where a CNN with an MLP head was used for classification and analyte quantification. As an alternative to a CNN, a vision transformer was employed for analyte quantification. Transformers have received increasing attention since their breakthrough in natural language processing [18, 19]. Patch-wise self-attention can be understood as a generalisation of CNNs which can improve the extraction of inter-related features that are spatially further apart but generally also requires more training data [20].
In Figure 3.5 (a) steady-state analysis is sketched, which was used in chapter 4 and for the evaluation of the vision transformer as well as models based on manual feature extraction. It involves the analysis of several points in time per feature: before binding (A), after binding (B) and after washing (C). The CNN was used as a feature extractor on the stacked images of the respective steady-state time steps. The features were then analysed with a MLP (b). Similarly, the vision transformer is used to find features for an MLP head (c). For the transformer, the images are segmented into patches which are transformed via learnable patch embeddings. This process is described in more detail in [21].
The analysis utilises only steady-state images, which prompted the urge for a method capable of handling time series since SPR is an optical technique yielding transitional data. For this purpose, the images from the binding curve of the experiment were sampled in discrete time steps (d) and analysed with two different approaches (e) (refer to Figure 3.5). In the first, the images were stacked in their third dimension and subsequently fed into a standard CNN with a MLP head. In the second approach a long short-term memory (LSTM) layer was put in sequence with a CNN where images from a sequence were presented in order so a representation of the time series could be learned [22, 23]. LSTMs are generally used for time-series data due to their ability to retain information from different time steps.

3.2.3.3 Data requirements

In order to utilise these models suitable data need to be recorded. As a rule of thumb, this data should enable an expert in the field to tackle the task at hand. As such, the measured data should correlate to the quantity in question which is reasonable to expect when the analyte causes a physical response at the sensor. As a consequence of this restriction extrapolation is to be avoided, so the training data should include the concentration ranges of the analytes that are expected in the sensor application environment. Similarly, substances that were not previously part of the training data may significantly impact the sensor's predictive capabilities. This principle severely limits the uses of such a sensor system but is very hard to circumvent. Alternatively, anomaly detection may be a more suitable approach, where an algorithm detects significant deviations from training data that represents a "normal" state. This is commonly achieved by autoencoder networks [24, 25].
Most importantly, the experimental design should reflect the research question and

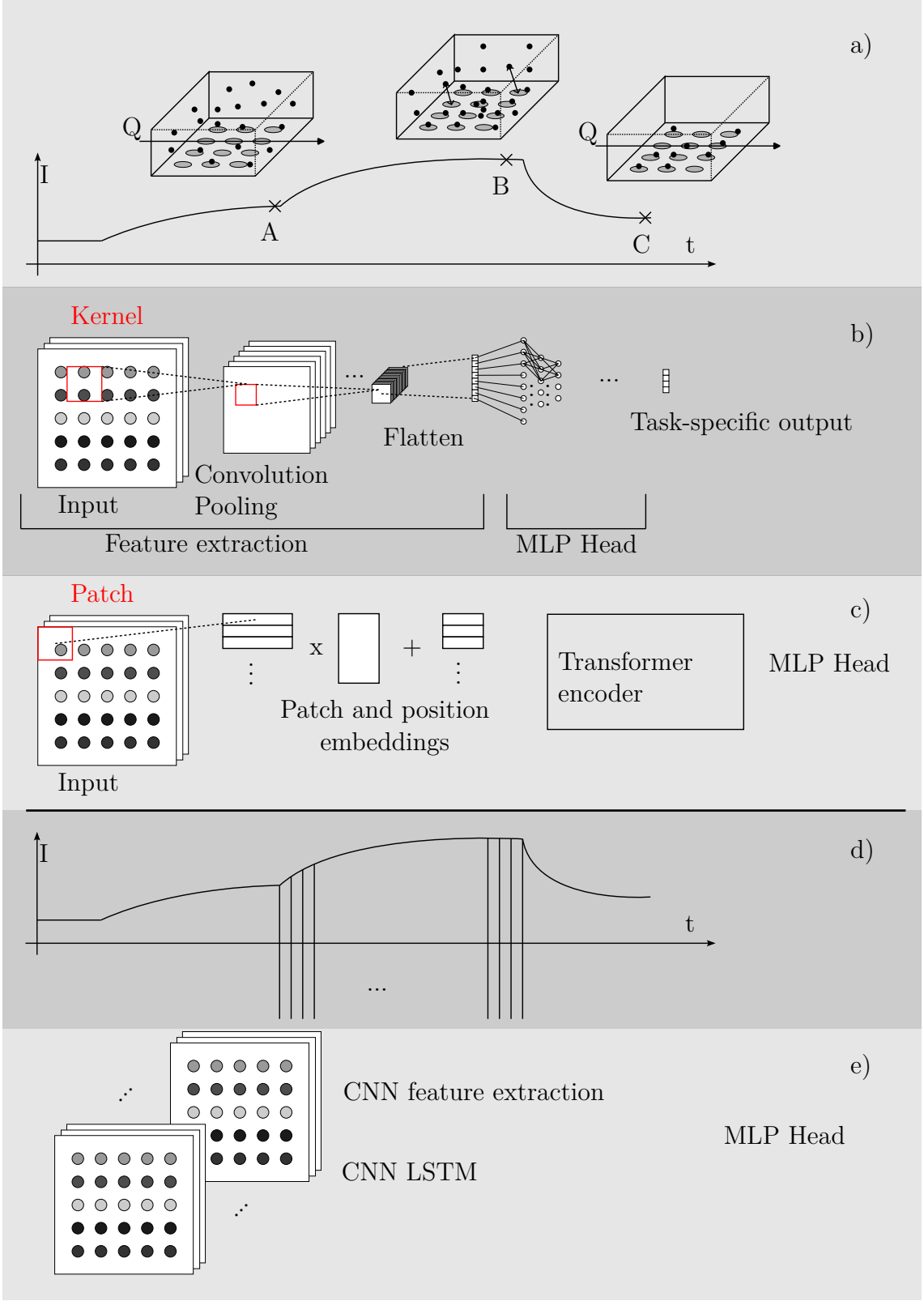

Fig. 3.5. Methods to process an image sequence in an experiment involving analyte association.

it has to be emphasised that an independent test set not used during training is required to make any significant claims. This requirement is sometimes lost upon or heavily obfuscated in literature which can partly invalidates the findings.
This raises questions about data quantity. While more complex algorithms generally require more data to converge and higher numbers of features further increase the samples needed, pre-trained models with strong bias and augmentation can help to limit experimental load. Biases can be introduced in different ways, e.g. by using CNNs for image data or by integrating physical information into the loss function:

$$\frac{1}{N}\sum_{b=1}^{N}\left[(y_b-\hat{y}_b)^2+(X_b(x_0,y_0)-I_{\mathrm{c,p}}(x_0,y_0,\Phi_0))^2\right]. \tag{3.18}$$

With batches one to N, the output label y_b, i.e. an analyte concentration and predicted analyte concentration $\hat{y}_b$ for every batch as regular mean squared loss. Additionally, there is an added term, where the input intensity I is modelled after Equation 3.10 and compared to the input image X at selected positions (x_0, y_0) via mean squared loss. These different loss types need to be properly normalised to work effectively but can help to decrease the number of samples needed to learn since physical information is introduced [26].
Image augmentation improves model performance when common cross-influences can be modelled effectively, e.g. intensity fluctuations due to changes in illumination conditions or shifting of the image when re-using sensors. However, it is preferable to include these variations in the experimental data where feasible.
Data quality and quantity can be explored using unsupervised methods like t-SNE (t-distributed stochastic neighbour embedding), UMAP (uniform manifold approximation and projection), and MDE (minimum-distortion embedding) [27–29]. These methods can be used to explore the feature space of the data in two or three dimensions. If no structure is visible in these embeddings, the data may be insufficient to solve the task at hand.

3.2.3.4 Data-based methods for Disentanglement

Data similarly to section 3.2.2.2 was used to evaluate the capabilities of a neural network to distinguish different signal contributions with simulated SPR images. Images were scaled to zero mean and a standard deviation of one and subsequently fed into a deep neural network consisting of fully-connected linear layers and Gaussian Error Linear Units (GELUs [30]) as non-linearities with three hidden layers to predict the refractive index of the adsorbate and the bulk. This architecture was chosen since there is no local structure where the application of a convolutional neural network would be beneficial although a CNN can be employed analogously. A grid of images generated with parameters found in section 3.2.2.1 was used for training, where the refractive index of the bulk and the adsorbate were used as labels. The grid contained different amounts of images ranging from 100 to 2500 where the refractive indeces were varied between zero and 2×10^{-3} , or zero and 2×10^{-5} for adsorbate and dielectric, respectively. Networks were trained with the addition of physical loss

Equation 3.18 and with regular root mean squared loss.
Test data was generated in accordance to section 3.2.2.2 for the in-distribution (id) data and with data outside the training set refractive index range for the out-of-distribution (ood) data.

Additionally, different architectures were tested against a dataset containing purines detected with the help of a semi-selective array as detailed in chapter 4. In addition to the CNN reported therein, three additional models were trained in reference to Figure 3.5: a vision transformer used for adenine quantification, and two models that incorporate more of the temporal information (see Figure 3.5 d and e).

3.3 Results and Discussion

First, the surface calibration is performed using the proposed algorithm after which the found surface parameters can be used for further modelling. Finally, results from the data-based methods are presented.

3.3.1 Exploring Parameter Space

Using the angular measurement in water with a single region of interest (ROI) to extract the SPR curve to fit the parameters of the SPR surface, the optimisation has no unique minimum. Thus, the resulting parameter distribution is characterised by skewed distributions and strong correlations between parameters (Figure 3.6). This result is expected and can be mitigated by using multiple refractive indices with otherwise constant parameters.
This can be shown by visualising the posterior distribution of the parameter space of such an optimisation for using three different refractive index solutions for calibration (Figure 3.7). While for a single measurement the parameter distributions show strong deviations of the median values from the maximum likelihood estimates (MLE) and especially for the chrome layer its parameter distributions are non-gaussian, this is not the case for multiple refractive indices. This indicates that multiple measurements using different refractive indices allows for more confident and precise prediction of surface parameters, as expected (see Figure 3.7) [9].

With the obtained optimum, the observed SPR curves can be compared to the measured curves and their residuals can be found (see Figure 3.8). Deviations from model to the measurements can have several reasons: improper alignment of the images, inhomogeneous region of interests, or inaccuracies of the model. Since errors are distributed close to zero with low variance and only a few outliers, a well-aligned model can be assumed. The, relative to water, higher refractive index of ethanol and 2-propanol shifts the curves to the right which results in the inclusion of the TIR angles in the measurement range which can be observed in the measurements.

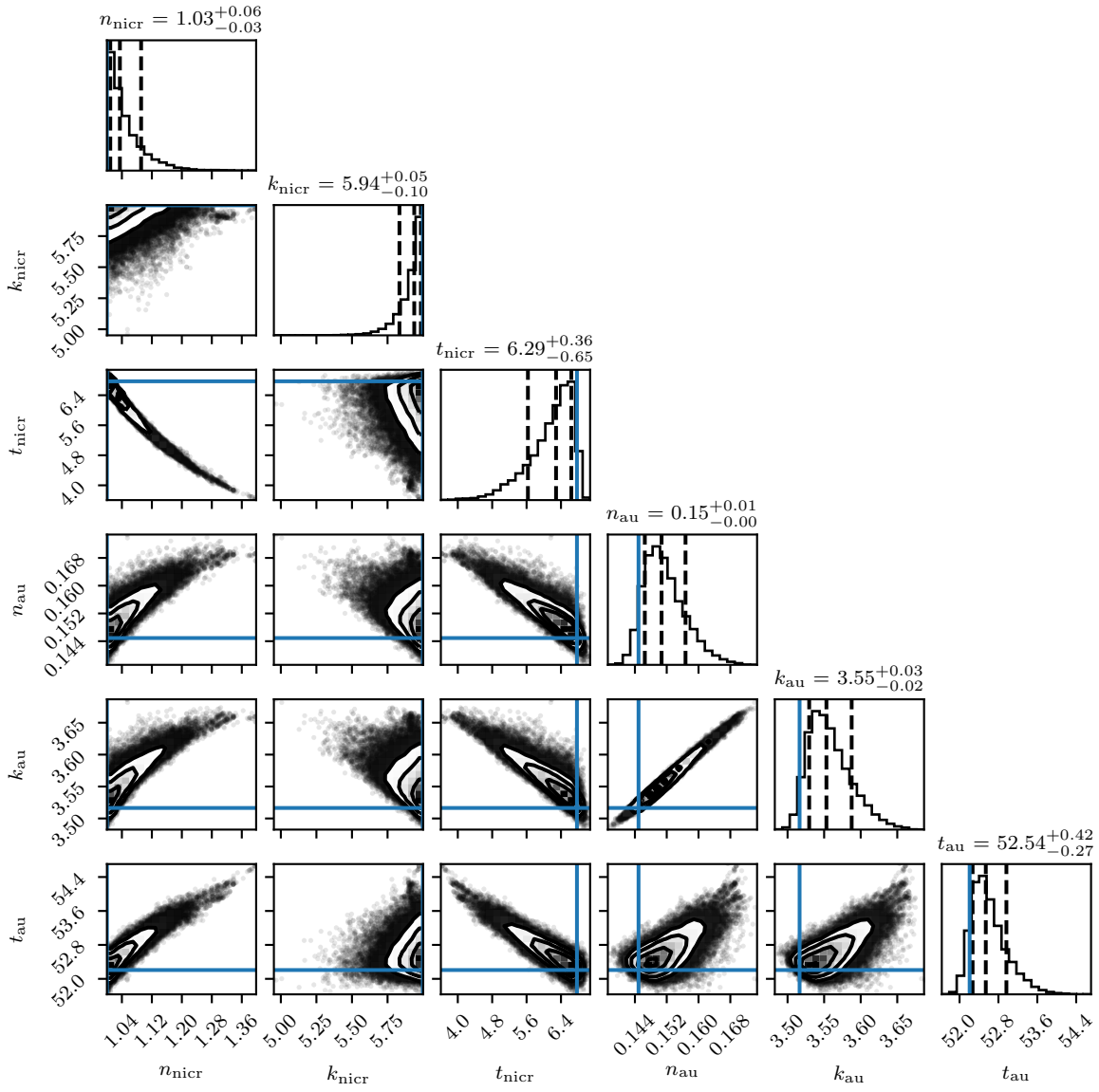

Fig. 3.6. Single refractive index measurement - Posterior distributions of parameters using Markov Chain Monte Carlo (MCMC) to generate samples. The single parameter distributions (1D histograms) indicate the parameter prediction quality. The joint distributions (2D histograms) reveal correlations between parameters. The maximum likelihood estimate (MLE, indicated in blue) is mostly outside the interquartile range of the distribution. The parameter predictions also do not compare well to the manufacturer's specifications (section C.1) and the (nickle-)chromium refractive indices are predicted close to their respective boundaries which makes the fit unreliable. Thicknesses t_{nicr} and t_{au} given in nm.

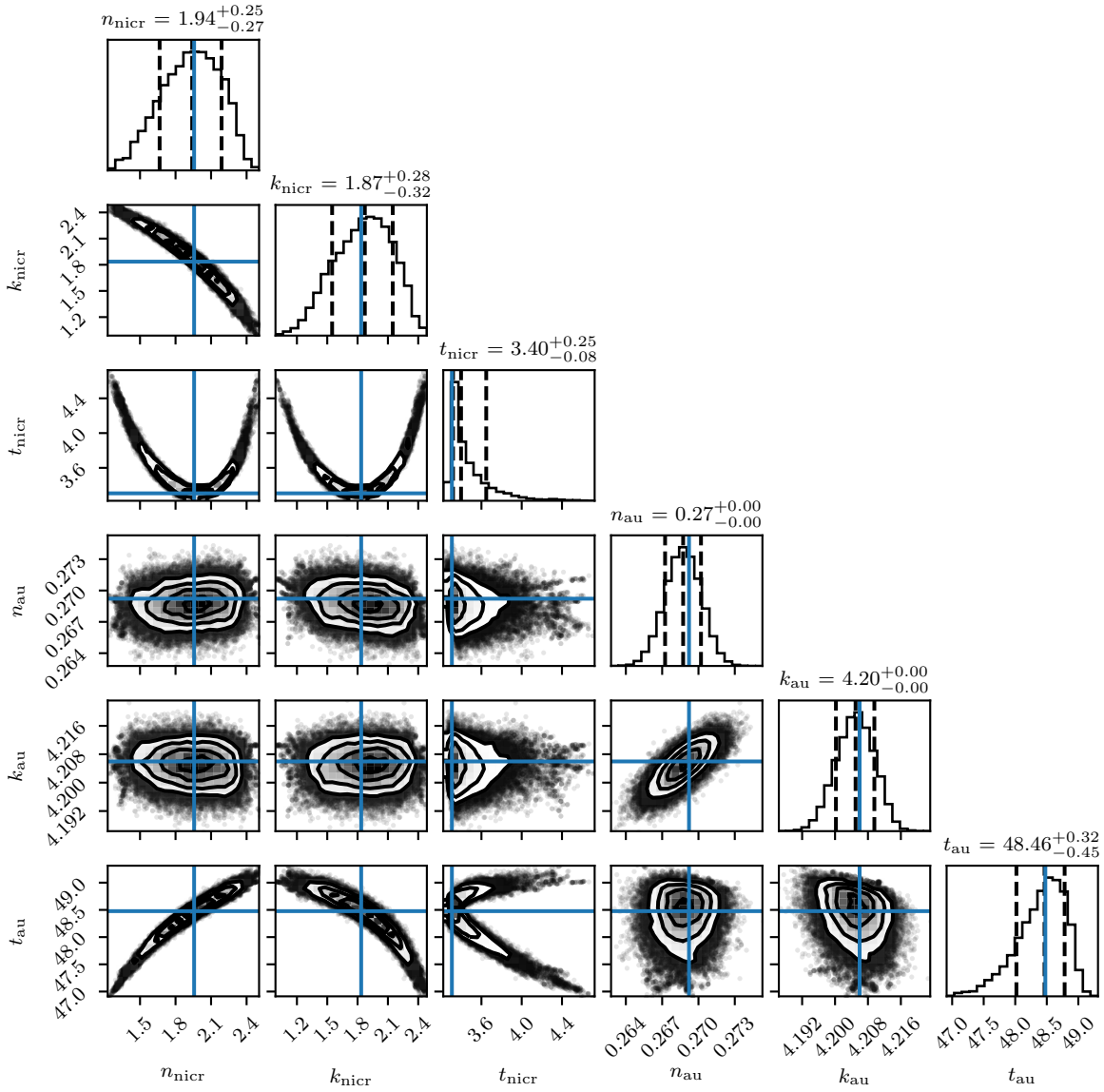

Fig. 3.7. Multiple refractive index measurement - Parameter distributions are generally more close to a gaussian and the MLE match with the distribution maxima as well as the specification (section C.1) and fall within the range reported in literature (Table 2.1).

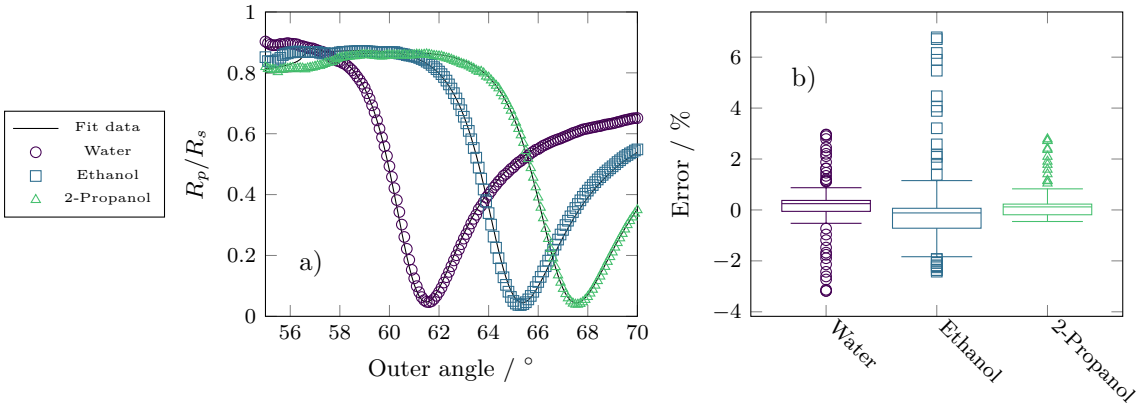

Fig. 3.8. Fit for three angular scans at different refractive indices; modelled refractive index of water, ethanol and 2-propanol according to [31], [32], and [33], respectively (a). Errors are distributed evenly and close to zero (b), with most outliers for ethanol below total internal reflection, which can be attributed to the image alignment which is more error-prone for angles far from the prism base angle.

Similarly, the posterior distributions of parameters using points over the entire prism surface with the angular distribution visualised in Figure 3.3 c increases the overall prediction quality (Figure 3.9). The MLE is well-aligned with the parameter distributions and their medians, the distributions are Gaussian and narrow and match well to the specification of the thicknesses of the metal layers. These results show that it is possible to find the SPR stack parameters from a single angular scan using just one wavelength and one refractive index solution. This greatly simplifies the instrumental setup and reduces measurement time. Additionally, the parameters were determined with data from the entire surface which reduces the effect of local variations in evaporation deposited metal on the determined parameters.

It was attempted to verify the calculated refractive indices by means of spectral ellipsometry. However, the high dimensionality of the problem means that any set of parameters can be fit to the observed curves. The available device (Horiba Auto SE, Horiba, Japan) did not allow changing the angle of incidence so that up to 33 parameters (with two metal layers and Lorentz-Drude formalism with up to five resonances) had to be fit to only one spectral measurement. This problem has no unique solution.

3.3.2 Predicting Refractive Index

The results in the following section are all produced in silico as a proof of concept and its application has been pursued experimentally in chapter 5.
With no added noise the parameters used for curve generation can be recovered almost perfectly for both angular ranges and all three conditions defined above.

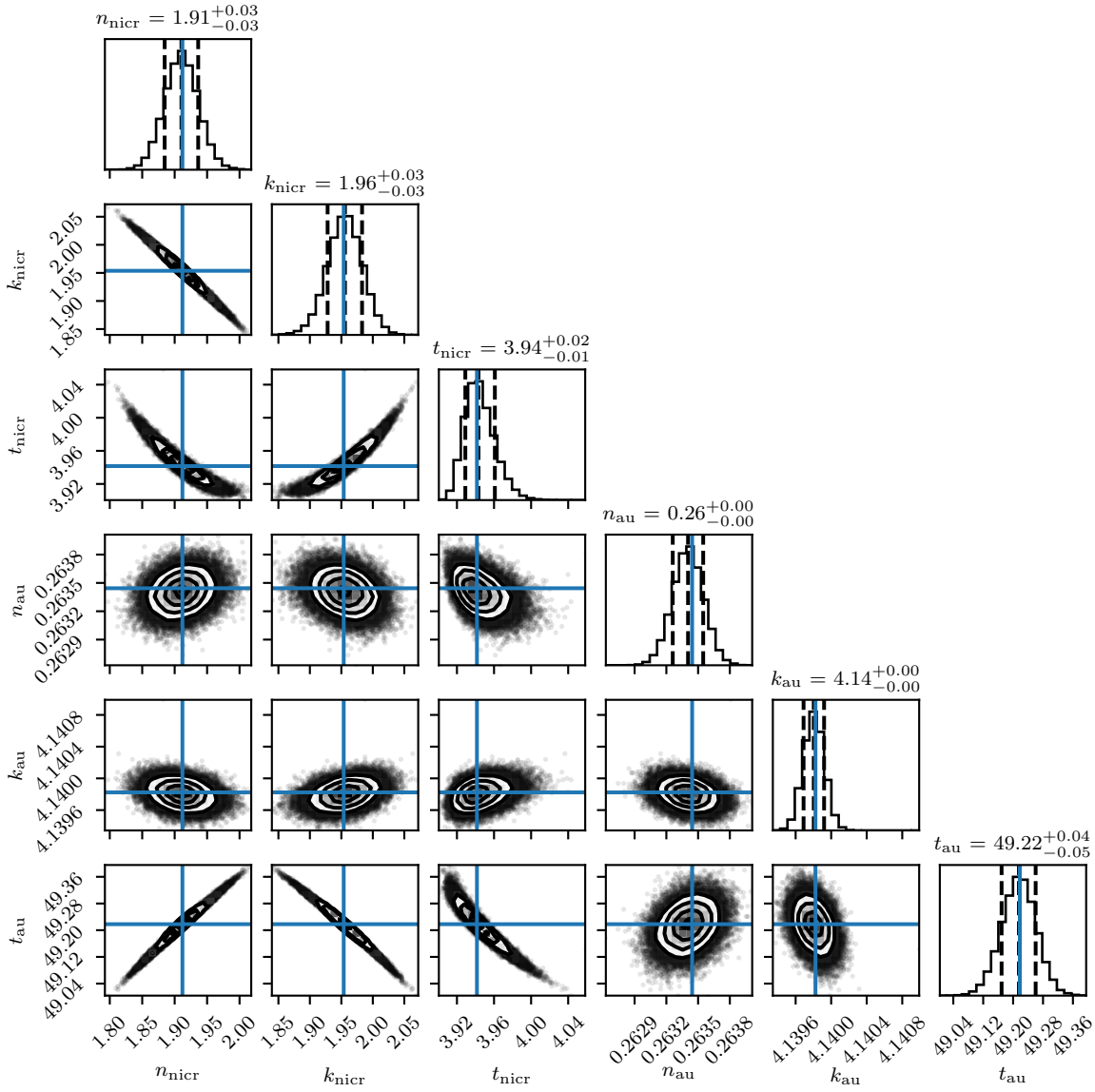

Fig. 3.9. Surface angle distribution - Parameter distributions are generally more close to a Gaussian and the MLE match with the distribution maxima as well as the specification (section C.1).

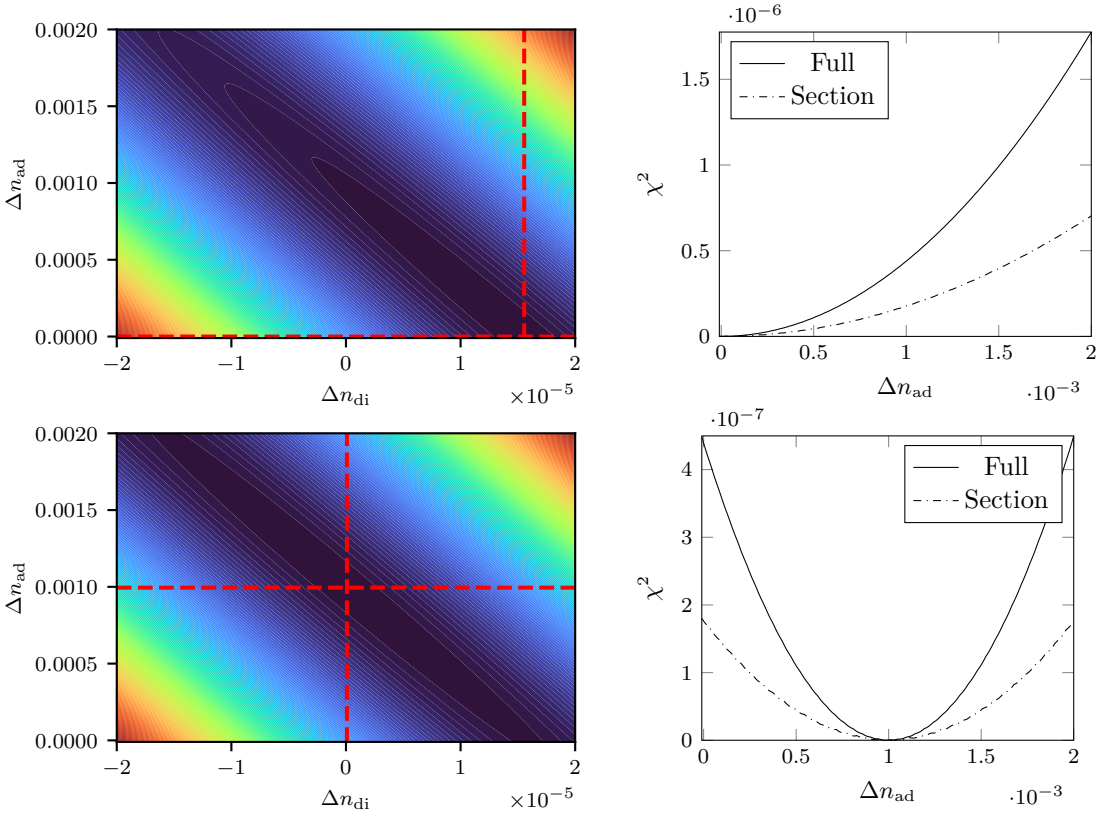

Fig. 3.10. Error surface in the parameter space of changes in bulk Δn_{di} and adsorption layer refractive index Δn_{ad} under a simulated change of $\Delta n_{\mathrm{di},2} \approx 1.5553 \times 10^{-5}\,\mathrm{RIU}$ (top) and $\Delta n_{\mathrm{ad},3} = 1 \times 10^{-5}\,\mathrm{RIU}$ (bottom). The minimum is indicated with the dashed lines. With a shift of the minimum, the whole surface shifts without perturbation. The minimum along the ridge is visualised in the right-hand plot for both the full angular range and a four degree section (where χ^2 is the squared residual sum). Data was generated by evaluating the fit function in a grid.

While the error surface in parameter space for the full angular range has a more pronounced minimum than with the reduced angular range, there is still a unique global minimum (Figure 3.10). This implies that measurement of the TIR position is not strictly required to simultaneously determine bulk refractive index and adsorption layer changes. The error surface was generated by calculating the error for every parameter combination in a grid defined by the graph axes. The fit error changes quickly when only one parameter is changed but by changing both along the ridge the minimum becomes less pronounced. A more distinct minimum is less vulnerable to noisy measurements and thus more stable in a real environment. The full section fit exhibits a more pronounced minimum which indicates its higher tolerance to noisy data.

With added Gaussian noise in the magnitude of a digit of a 14-bit camera, the prediction quality will be reduced. The three example conditions were analysed with regards to the prediction error of the fitted parameters towards the real parameter

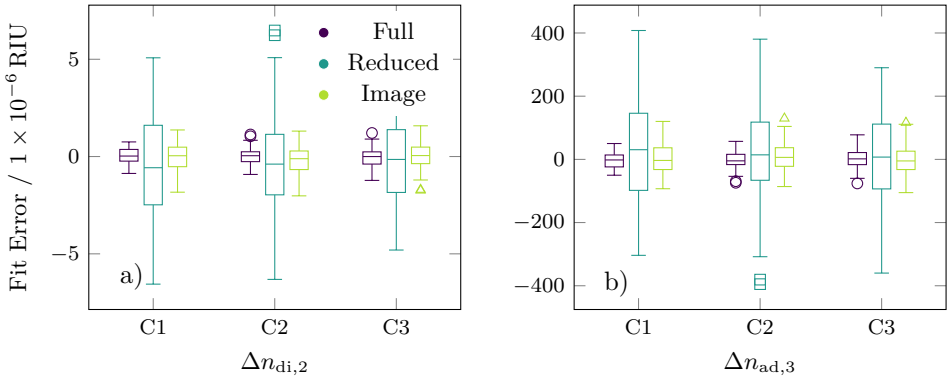

Fig. 3.11. Fit error of the refractive index parameters with added Gaussian noise for the three conditions C1 to C3, and the three range of used values. The reduced angular range results in a poorly defined fit parameter, while using data from the entire surface leads to an almost retained prediction quality compared to the full angular range.

values for 100 repeats with added Gaussian noise. It can be observed that the error using the reduced angular range becomes rather large and can be in the magnitude of the parameter change thus rendering a single measurement with reduced range impractical. Utilising the full angular range, the variance is reduced significantly. When data from the entire image surface is used, a similar result can be observed (Figure 3.11). This observation indicates that image-based measurements with a small angle projected onto the surface can be utilised similarly to an angular scan including the TIR angle with regards to refractive index disentanglement.
As noise increases the fit error variation increases, too. This imposes a limit on the disentangled determination of bulk refractive index change and change of adsorbate. High resolution and signal-to-noise ratio is a necessity to accurately determine the refractive indices of the different layers. However, it can be clearly seen that correct discrimination of bulk refractive index changes and of an adsorbate is possible without the use of the TIR angle.

3.3.3 Data-based Modelling

When using in-distribution (id) data in the test set, the prediction error is very low for both physical and non-physical loss (Figure 3.12). The data-based method compares well to the model-based method and can even outperfom the latter. However, the training data has to be suitable for the task which in the case of out-of-distribution (ood) data leads to misquantification of the refractive index. Physical loss can mitigate this to a degree for very low training set sizes.

The vision transformer was suitable for analyte quantification while slightly worse in performance (3.9 µM mean absolute error in the test set compared to 1.8 µM for a CNN as presented in chapter 4).

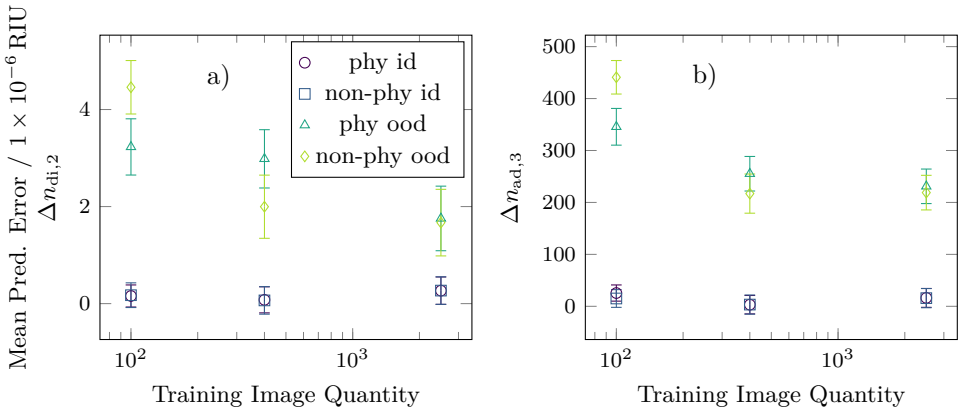

Fig. 3.12. Mean absolute prediction errors for the conditions C1, C2, and C3 for different training set sizes. Errors for added physical loss (phy) and regular root mean squared loss (non-phy) as well as in-distribution (id) and out-of-distribution (ood) test data are shown.

In the first alternative model the images were stacked in their third dimension and subsequently fed into a standard CNN with a MLP head. In the second approach a long short-term memory (LSTM) layer was put in sequence with a CNN where images from a sequence were presented in order so a representation of the time series could be learned [22, 23]. Although both models were learning from the training set (i.e. the train loss decreased), generalisation was not possible (the validation loss did not improve). This is probably due to the low amount of data available for this approach: every analyte was only presented to a sensor six times and two sensors were available for training so the training set was essentially reduced to twelve examples. This could be improved by augmentation since every example can be sampled in different time steps but the amount of data was evidently insufficient. Additionally, mass transport may not be perfectly reproducible between sensors when the flow cell is removed and re-introduced resulting in potentially different thicknesses of flow channels.

3.4 Conclusion

Within this chapter, an SPRi-based sensor utilising spatial angle modulation was evaluated. To the best of the author's knowledge, this is the first time SPR surface parameters were determined with such a sensor by merely applying angular modulation. The presented method reduces measurement time and instrumental complexity. SPRi allows for two methods that enable the determination of the signal change origin when subject to changes in bulk refractive index and adsorption changes: use of recognition elements and angular modulation across the sensor surface. Within this chapter the method of angular modulation was explored and a proof of concept was provided. The disentangled determination of bulk refractive index change and

changes at the surface by the analyte is, however, dependent on the data quality i.e., the signal-to-noise ratio.
As an alternative, data-based modelling can be employed which may use angle-modulated SPRi implicitly by weighting the different areas in the image accordingly. This is generally less data-efficient since training data has to be provided and the amount significantly impacts the performance. On the other hand, the data-based approach is more flexible in its modelling capabilities because less assumptions have to be made of the data beforehand. As a third approach hybrid modelling can be applied, where the physical information can be used as a bias for the neural network by means of a modified loss function. This increases data efficiency while the flexibility is maintained.

References

[1] M. J. O'Brien, V. H. Pérez-Luna, S. Brueck, G. P. López, "A Surface Plasmon Resonance Array Biosensor Based on Spectroscopic Imaging", *Biosensors and Bioelectronics* **2001**, *16*, 97–108, DOI 10.1016/S0956-5663(00)00137-8 (cit. on p. 38).

[2] T. Del Rosso, J. E. H. Sánchez, R. D. S. Carvalho, O. Pandoli, M. Cremona, "Accurate and Simultaneous Measurement of Thickness and Refractive Index of Thermally Evaporated Thin Organic Films by Surface Plasmon Resonance Spectroscopy", *Optics Express* **2014**, *22*, 18914, DOI 10.1364/OE.22.018914 (cit. on p. 38).

[3] G. Beketov, Y. Shirshov, O. Shynkarenko, V. Chegel, "Surface Plasmon Resonance Spectroscopy: Prospects of Superstrate Refractive Index Variation for Separate Extraction of Molecular Layer Parameters", *Sensors and Actuators B: Chemical* **1998**, *48*, 432–438, DOI 10.1016/S0925-4005(98)00081-1 (cit. on p. 38).

[4] L. Liu, J. Guo, Y. He, P. Zhang, Y. Zhang, J. Guo, "Study on the Despeckle Methods in Angular Surface Plasmon Resonance Imaging Sensors", *Plasmonics* **2015**, *10*, 729–737, DOI 10.1007/s11468-014-9859-0 (cit. on p. 38).

[5] K. Ma, L. Liu, P. Zhang, Y. He, Q. Peng, "Optimization of Angle-Pixel Resolution for Angular Plasmonic Biosensors", *Sensors and Actuators B: Chemical* **2019**, *283*, 188–197, DOI 10.1016/j.snb.2018.12.023 (cit. on p. 38).

[6] S. Zhan, X. Wang, Y. Liu, "Fast Centroid Algorithm for Determining the Surface Plasmon Resonance Angle Using the Fixed-Boundary Method", *Measurement Science and Technology* **2011**, *22*, 025201, DOI 10.1088/0957-0233/22/2/025201 (cit. on p. 38).

[7] D. J. Griffiths, *Introduction to Electrodynamics*, Fourth edition, Pearson, Boston, **2013** (cit. on p. 39).

[8] W. N. Hansen, "Electric Fields Produced by the Propagation of Plane Coherent Electromagnetic Radiation in a Stratified Medium", *Journal of the Optical Society of America* **1968**, *58*, 380, DOI 10.1364/JOSA.58.000380 (cit. on p. 39).

[9] T. M. Chinowsky, S. S. Yee, "Quantifying the Information Content of Surface Plasmon Resonance Reflection Spectra", *Sensors and Actuators B: Chemical* **1998**, *51*, 321–330, DOI 10.1016/S0925-4005(98)00207-X (cit. on pp. 41, 51).

[10] M. Piliarik, J. Homola, "Self-Referencing SPR Imaging for Most Demanding High-Throughput Screening Applications", *Sensors and Actuators B: Chemical* **2008**, *134*, 353–355, DOI 10.1016/j.snb.2008.06.011 (cit. on p. 41).

[11] D. Foreman-Mackey, D. W. Hogg, D. Lang, J. Goodman, "Emcee: The MCMC Hammer", *Publications of the Astronomical Society of the Pacific* **2013**, *125*, 306–312, DOI 10.1086/670067 (cit. on p. 44).

[12] J. Svirelis, J. Andersson, A. Stradner, A. Dahlin, "Accurate Correction of the "Bulk Response" in Surface Plasmon Resonance Sensing Provides New Insights on Interactions Involving Lysozyme and Poly(Ethylene Glycol)", *ACS Sensors* **2022**, *7*, 1175–1182, DOI 10.1021/acssensors.2c00273 (cit. on p. 44).

[13] K. Hornik, M. Stinchcombe, H. White, "Multilayer Feedforward Networks Are Universal Approximators", *Neural Networks* **1989**, *2*, 359–366, DOI 10.1016/0893-6080(89)90020-8 (cit. on p. 45).

[14] I. Goodfellow, Y. Bengio, A. Courville, *Deep Learning*, The MIT Press, Cambridge, Massachusetts, **2016** (cit. on p. 47).

[15] A. S. Malinick, D. D. Stuart, A. S. Lambert, Q. Cheng, "Surface Plasmon Resonance Imaging (SPRi) in Combination with Machine Learning for Microarray Analysis of Multiple Sclerosis Biomarkers in Whole Serum", *Biosensors and Bioelectronics: X* **2022**, *10*, 100127, DOI 10.1016/j.biosx.2022.100127 (cit. on p. 47).

[16] A. Kirillov et al., Segment Anything, **2023**, DOI 10.48550/ARXIV.2304.02643 (cit. on p. 47).

[17] T. Hastie, R. Tibshirani, J. H. Friedman, *The Elements of Statistical Learning: Data Mining, Inference, and Prediction*, Second edition, Springer, New York, NY, **2017** (cit. on p. 48).

[18] A. Vaswani, N. Shazeer, N. Parmar, J. Uszkoreit, L. Jones, A. N. Gomez, L. Kaiser, I. Polosukhin, Attention Is All You Need, **2017**, DOI 10.48550/ARXIV.1706.03762 (cit. on p. 48).

[19] X. Amatriain, A. Sankar, J. Bing, P. K. Bodigutla, T. J. Hazen, M. Kazi, Transformer Models: An Introduction and Catalog, **2023**, DOI 10.48550/ARXIV.2302.07730 (cit. on p. 48).

[20] S. Khan, M. Naseer, M. Hayat, S. W. Zamir, F. S. Khan, M. Shah, "Transformers in Vision: A Survey", *ACM Computing Surveys* **2022**, *54*, 1–41, DOI 10.1145/3505244 (cit. on p. 48).

[21] A. Dosovitskiy et al., An Image Is Worth 16x16 Words: Transformers for Image Recognition at Scale, **2020**, DOI 10.48550/ARXIV.2010.11929 (cit. on p. 48).

[22] T.-Y. Kim, S.-B. Cho, "Predicting Residential Energy Consumption Using CNN-LSTM Neural Networks", *Energy* **2019**, *182*, 72–81, DOI 10.1016/j.energy.2019.05.230 (cit. on pp. 48, 58).

[23] I. E. Livieris, E. Pintelas, P. Pintelas, "A CNN–LSTM Model for Gold Price Time-Series Forecasting", *Neural Computing and Applications* **2020**, *32*, 17351–17360, DOI 10.1007/s00521-020-04867-x (cit. on pp. 48, 58).

[24] F. Esmaeili, E. Cassie, H. P. T. Nguyen, N. O. V. Plank, C. P. Unsworth, A. Wang, "Anomaly Detection for Sensor Signals Utilizing Deep Learning Autoencoder-Based Neural Networks", *Bioengineering* **2023**, *10*, 405, DOI 10.3390/bioengineering10040405 (cit. on p. 48).

[25] C. Zhou, R. C. Paffenroth in Proceedings of the 23rd ACM SIGKDD International Conference on Knowledge Discovery and Data Mining, ACM, Halifax NS Canada, **2017**, pp. 665–674, DOI 10.1145/3097983.3098052 (cit. on p. 48).

[26] Nils Thuerey, Philipp Holl, Maximilian Mueller, Patrick Schnell, Felix Trost, Kiwon Um, *Physics-Based Deep Learning Book* (cit. on p. 50).

[27] L. van der Maaten, G. Hinton, "Visualizing Data Using T-SNE", *Journal of Machine Learning Research* **2008**, *9*, 2579–2605 (cit. on p. 50).

[28] L. McInnes, J. Healy, J. Melville, UMAP: Uniform Manifold Approximation and Projection for Dimension Reduction, **2020**, DOI 10.48550/arXiv.1802.03426 (cit. on p. 50).

[29] A. Agrawal, A. Ali, S. Boyd, "Minimum-Distortion Embedding", *Foundations and Trends® in Machine Learning* **2021**, *14*, 211–378, DOI 10.1561/2200000090 (cit. on p. 50).

[30] D. Hendrycks, K. Gimpel, Gaussian Error Linear Units (GELUs), **2023**, DOI 10.48550/arXiv.1606.08415 (cit. on p. 50).

[31] A. H. Harvey, J. S. Gallagher, J. M. H. L. Sengers, "Revised Formulation for the Refractive Index of Water and Steam as a Function of Wavelength, Temperature and Density", *Journal of Physical and Chemical Reference Data* **1998**, *27*, 761–774, DOI 10.1063/1.556029 (cit. on p. 54).

[32] S. Kedenburg, M. Vieweg, T. Gissibl, H. Giessen, "Linear Refractive Index and Absorption Measurements of Nonlinear Optical Liquids in the Visible and Near-Infrared Spectral Region", *Optical Materials Express* **2012**, *2*, 1588, DOI 10.1364/OME.2.001588 (cit. on p. 54).

[33] E. Sani, A. Dell'Oro, "Spectral Optical Constants of Ethanol and Isopropanol from Ultraviolet to Far Infrared", *Optical Materials* **2016**, *60*, 137–141, DOI 10.1016/j.optmat.2016.06.041 (cit. on p. 54).

Chapter 4

Semi-Selective Array for the Classification of Purines with Surface Plasmon Resonance Imaging and Deep Learning Data Analysis

In process analytics or environmental monitoring, the real-time recording of the composition of complex samples over a long period of time presents a great challenge. Promising solutions are label-free techniques such as surface plasmon resonance spectroscopy. They are, however, often limited due to poor reversibility of analyte binding. In this work we introduce how SPR imaging in combination with a semi-selective functional surface and smart data analysis can identify small and chemically similar molecules. Our sensor uses individual functional spots made from different ratios of graphene oxide and reduced graphene oxide, which generate a unique signal pattern depending on the analyte due to different binding affinities. These patterns allow four purine bases to be distinguished after classification using a convolutional neural network (CNN) at concentrations as low as 50 µM. The validation and test set classification accuracies were constant across multiple measurements on multiple sensors using a standard CNN, which promises to serve as a future method for developing online sensors in complex mixtures.

4.1 Introduction

Sensors used to monitor the environment or industrial processes must withstand the challenges of complex mixtures. Apart from a changing analyte matrix, it is often also desirable to recognize a specific analyte molecule or to detect the presence of unknown substances that either disrupt the process or can pose a hazard in the environment. These circumstances have greatly fueled research interest in electronic noses and electronic tongues [1–3]. A label-free detection mechanism as offered by surface plasmon resonance imaging (SPRi) is advantageous for long-term online monitoring. In addition, SPRi offers the potential of multi-analyte detection [4]. Intensity-based SPRi allows the spatially resolved detection of changes in the refractive index over time in the immediate vicinity of the sensor surface with a penetration depth of a few hundred nm. This allows changes in the composition of the analyte matrix to be detected as a change in refractive index. If the surface is functionalized in such a way that certain analyte molecules bind to it, an analyte can also be determined in a targeted and very sensitive manner. The larger the analyte, e.g. in the case of proteins or micro-organisms, the easier it is to detect. In the case of small molecules, this is significantly more difficult due to the lower change in refractive index [5]. This principle proves disadvantageous for long-term online detection of a complex mixture. The pure refractive index change is not specific enough, and targeted binding of analytes to receptors must be established quickly and reversibly in an equilibrium to the concentration of the analyte in the matrix. For the development of very sensitive sensors, one uses receptors with a high binding affinity. However, this means that desorption of the analyte from the surface occurs only very slowly, if at all. The system loses its reversibility. If, on the other hand, the sensor surface is structured with receptors with low selectivity, sensitivity is lost at first approximation, but changes in the analyte matrix can be reversibly tracked over time. If several such receptors are used, unique sensor response patterns can be generated, which are suitable for detecting several analytes in parallel [6]. For example, different beverages

could be classified with a receptor array composed of different mixtures of lactose and sulphated lactose [7].

A promising class of receptors for SPR sensors are 2D carbon materials, especially its two representatives, graphene oxide (GO) and reduced graphene oxide (rGO). These materials are known in SPR sensing for signal amplification or for target binding. [8–10] Additionally, they adhere very well to gold surfaces, and the SPR characteristics of both materials are almost identical. This is particularly useful for intensity-based SPR measurements, as it allows tracking the reflectivity of light at the surface over time at a single angle of incidence. It should also be mentioned that both, GO and rGO, can be chemically functionalized in a wide variety of ways [11, 12]. With GO as the hydrophilic and rGO as the more hydrophobic receptor, their π-system enables the formation of weak interactions between analyte molecules and the receptor surface, i.e. π-stacking in addition to electrostatic, van der Waals, and H-bonding. The contribution of each interaction varies with changing receptor composition. If considering that a single angle of incidence for the surface plasmon excitation is suitable for all mixtures of GO and rGO without losing sensitivity for individual receptor spots, this, in combination with the use of a highly sensitive SPRi setup with a resolution of the refractive index down to a range of 10^{-7} RIU (refractive index units), compensates the disadvantage of lower sensitivity due to the weaker interactions [13].

One of the biggest challenges in online monitoring of complex mixtures is the determination of changes in the concentration of individual metabolites. These are often similar in their structure and in many of their physico-chemical properties and therefore difficult to discriminate, especially in label-free techniques. The molecules caffeine, uric acid, oxipurinol, and adenine belong to the group of purines and are related through the human metabolism. Oxipurinol is the main metabolite of allopurinol which is administered when uric acid levels in blood are excessive. When found in groundwater, oxipurinol can be linked to an anthropomorphic influence on the groundwater due to treated wastewater [14]. One possibility is to design a sensor array with semi-selective receptors which make use of weak molecular interactions to generate signal patterns that can be addressed to those analytes. Here, GO and rGO, are ideal model receptors. Depending on the synthesis, their properties can be tuned, allowing one to obtain materials that are more capable of π-stacking or others that favour van der Waals interaction or H-bonding.

SPR receptor arrays have been evaluated using dimensionality reduction methods and k-NN classifiers [15], as well as linear discriminant analysis [16], or with the help of support vector machines [17] and similar methods. Since in SPRi entire images are available, it is reasonable to employ state-of-the-art classification algorithms like convolutional neural networks (CNNs) for image data. Especially for semi-selective receptors where homogeneity of every spot is limited and exact composition and position may vary, automatic feature extraction is more appropriate than manually tracking receptor positions and their relationships. This is even more important when handling multiple similar sensors, which might differ in their properties. In many fields of analytical chemistry, deep learning has emerged as a tool to enhance

or enable sensing tasks, e.g. for analyte classification, concentration determination [18], segmentation of fluorophores [19], spectral analysis [20], and many more [21, 22]. In SPR, deep learning methods have been mostly applied to microscopy in order to enable or enhance scattering particle detection [23] or to reduce computational load for phase retrieval [24].

Herein, a functional surface comprising different mixtures of GO and rGO has been designed and applied in an intensity-based SPR imaging setup to discriminate adenine, caffeine, oxipurinol, and uric acid. Two different model classes were evaluated on this array data: a tree-based classifier with hand-selected features and a CNN-based model. It is shown that with the help of this array and a CNN model, the classification of four different purines is possible and the model's accuracy is retained over multiple measurements on different sensors and generalizes to new unseen sensors.

4.2 Methods

4.2.1 GO/rGO Synthesis

GO/rGO Synthesis. Graphene oxide was synthesized following an adapted low-temperature Hummers method [25]. In a typical procedure flake graphite (2 g, 99.5 %, Thielmann Graphite) and sodium nitrate (1.5 g, p.a., Merck) were dispersed in sulfuric acid (150 mL, >95 %, w/w, Fisher Chemicals) and cooled to −10 °C in an ice and salt bath. Potassium permanganate (9 g, p.a., Merck) was added over a duration of 8 h under vigorous stirring. The mixture was stirred overnight and subsequently sonicated for 1 h at 4 °C. After six additional days of stirring at 4 °C, the mixture was again cooled to −10 °C and 200 mL of water was added over 8 h. Temporarily the temperature was raised to 9 °C to prevent solidification from sulfuric acid monohydrate. 30 mL of 35 % (w/w) hydrogen peroxide solution was then added slowly to reduce the insoluble by-product MnO_2 to the water-soluble Mn^{2+}. The product was washed three times with 3 % (v/v) sulfuric acid and once with 1 M hydrochloric acid before redispersing in water. Finally, the resulting GO dispersion was dialyzed against water (MWCO: 12-14 kDa) and stored (at 1.5 g L^{-1}) at 4 °C.

For the synthesis of rGO, freeze-dried GO was dispersed in liquid ammonia (0.2 g L^{-1}) and cooled in a dry ice ethanol bath. Potassium was added in excess and the mixture was stirred for 1 h. Then the dry ice ethanol bath was removed, and the ammonia evaporated. The dry rGO was dispersed and washed with water and the solvent was changed to N-methyl-2-pyrrolidone (NMP) at a concentration of 0.2 g L^{-1} [26]. GO and rGO were mixed in total-weight ratios of 1:0, 4:1, 3:2, 1:1, 2:3, 1:4, and 0:1 in a constant solvent mixture of NMP and water (20:1, v/v) at 0.07 g L^{-1} [27].

Sensors. Glass prisms (SF2 18×18mm 62°, Schott AG, Germany) were purchased from Gräfe Spezialoptik (Germany). A 50 nm thin gold layer on top of a 4 nm chromium adhesion layer was used to generate surface plasmons on the glass prism.

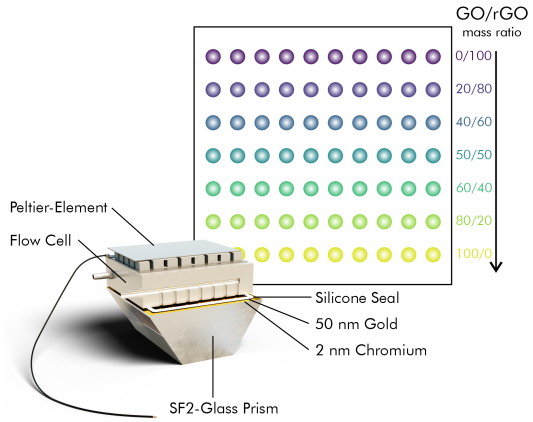

Fig. 4.1. Measurement cell setup and dispensing pattern of dispensed nanomaterial-spots (graphene oxide (GO), reduced graphene oxide (rGO) and their mixtures).

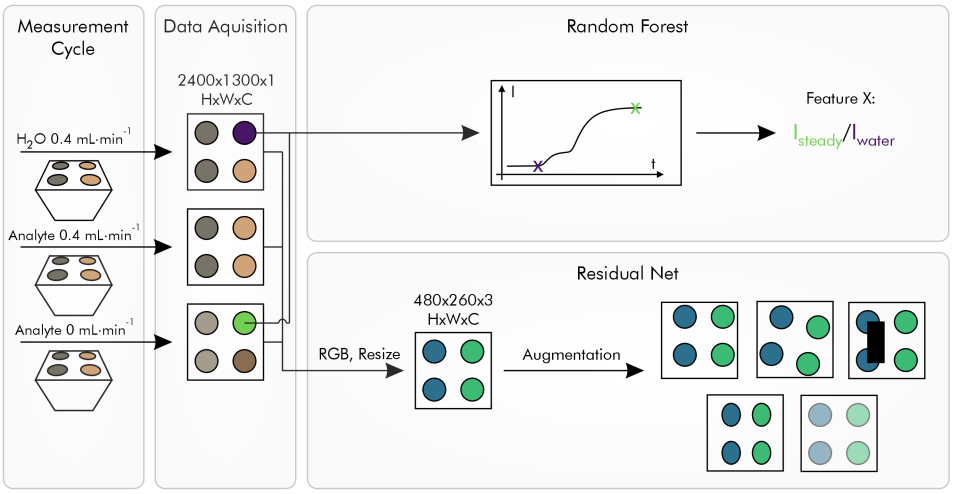

Fig. 4.2. Data extraction from images - Mean intensities from 58 regions of interest were extracted from the steady state images and subsequently used in the tree model. The entire images were used in a convolutional neural network. The CNN-based detection scheme incorporates three images for every analyte state into a three-channel image. During training, the resized images were augmented by translation, rotation, erasing, homographic projection and brightness variation to prevent overfitting.

Both layers were deposited via physical vapor deposition at CREAVAC (Creative Vakuumbeschichtung GmbH, Germany). The mixtures consisting of 2D carbon nanomaterials were sonicated for 10 min before dispensing them with a Musashi ShotMini 200 Sx dispenser (Musashi, Japan) on top of the gold layer. Each GO/rGO mixture was dispensed in a row of ten spots with 500 µm in diameter and 1.5 mm in distance. Seven rows with different mixtures were dispensed in a vertical distance of 2 mm, resulting in a 10 by 7 matrix of nanomaterial spots (Figure 4.1). The volume per spot is approximately 1 µL. After dispensing, the solvent was allowed to slowly evaporate at 50 °C. For a better adhesion of the dispensed material to the gold, the prisms were heated to 80 °C for 30 min.[28] Finally, to prevent non-specific binding to non-covered areas on the gold surface, these were blocked with a self-assembled monolayer of 1-hexadecanethiol.

Data Acquisition Parameters. Surface plasmon resonance images were captured with a 14bit camera (FLIR, Germany) controlled by an in-house software. After a full SPR angle scan, an appropriate angle of 62° was set for every prism. Ten 14-bit images are averaged and saved every 2 s and cropped on a camera to 2,400×1,300 pixels to fit the prism surface.

Experiments. One measurement comprises consecutively pumping the respective analyte for 20 min at a flow rate of 0.4 mL/min, after which the flow is stopped for 20 min. In between two analytes, the sensor is flushed by the analyte-free medium for 20 min at a flow rate of 0.4 mL/min. This way, the purine adenine was quantified from 0 to 50 µM within a mixture of other purines (caffeine, uric acid, and oxipurinol) in Millipore water, each at a concentration of 50 µM.

Purine classification experiments were carried out at a concentration of 50 µM in Millipore water. Their refractive indices were determined with a refractometer (Krüss DR-6300T, Krüss, Germany) and found to be indistinguishable from pure water within its accuracy. During each repetition, a full cycle of these measurements is performed twice on every prism (Figure 4.2).

A robustness experiment for the classification of the purine bases under heavily changed conditions was conducted in synthetic urine according to DIN EN ISO 20696 (Synthetic Urine e.K., Germany), with a 730 nm light source on a prism with only six different GO/rGO mixtures. The changed light source entails an adjusted measurement angle of 59.5°. Prism surfaces were additionally structured with mirror areas which can be used to correct for incident light changes.

Pre-Processing. Data were split into training, validation and test datasets depending on the experiment. Test data were never used during model optimization or evaluation. Steady-state data were extracted and labeled according to the corresponding analyte state by extracting the last two minutes of the 20-minute windows for washing steps, analyte flow and stopped flow, respectively.

For adenine quantification, images were presented to a CNN (for network hyperparameters see Table B1). A three-channel image similar to an RGB image was

constructed from an analyte steady-state image referenced with the corresponding washing step and analyte flow state as colour channels. Data points at 0, 2, 10, and 50 µM analyte concentration were used for training, and the model was tested at concentrations of 5 and 20 µM.

For purine classification in Millipore water, data from two prisms were split into different cross-validation folds. Finally, the test accuracy was calculated on the data acquired with a third prism as shown in Figure B6. As baseline, an extra-tree classifier (as implemented in scikit-learn, herein referred as the tree model) was used. For this, tabular data was extracted from the images by manually selecting 58 regions of interest on GO/rGO spots from the image data for each prism. Additionally, 58 regions of interest on the gold surface were selected for a second tree model, which was trained to compare the classification accuracy with data extracted from the functional spots to gold-thiol surfaces (see Figure B6.c). Alternatively, images were presented to a CNN. The samples were resized to limit memory footprint and normalized to conform with the residual net inputs. Two different residual nets, which are a subset of CNNs, were evaluated (ResNet-18 [29], ResNeXt-50 with 32x4d [30]), pretrained weights were used, and a dropout layer was added to the fully connected layer. The input was adjusted to the colour channel number, and the output was reduced to four classes. The data points were acquired according to Figure 4.2.

Urine classification data were used in a transfer learning setup by re-training the neural network obtained from previous classification for five epochs.

4.3 Results and Discussion

Surface Characterization. For detection and classification of small molecules with a similar chemical structure, high-affinity receptors for each analyte are needed to generate specific responses. Because of this, the recovery of a sensor is limited since strong binding interactions need to be broken up, e.g. by heating or chemical reactions. An array of semi-selective receptors facilitates such a task when the receptors exhibit different binding affinities for changing analytes. Through the mixing of GO and rGO, a functional surface with gradations of hydrogen-bonding and van der Waals/π-stacking forces are expected to be obtained. The content of rGO in the mixture affects the overall amount of sp^2-hybridized carbon of the spot, which in turn influences the non-polar to polar binding ratio. The Raman spectra (Figure 4.3) reflect the differences in hybridization from mostly sp^3 for GO to increasingly sp^2 for rGO.

The more efficiently GO is reduced, the greater are the differences in binding properties. By the chosen reduction method, a sufficient difference is achieved, which may not be the case for typical reduction methods, as with hydrazine-hydrate at 90 °C (Figure B7). As an increasing amount of sp^2 carbon also influences the absorption spectrum of the material, UV-vis spectroscopy was used to show the

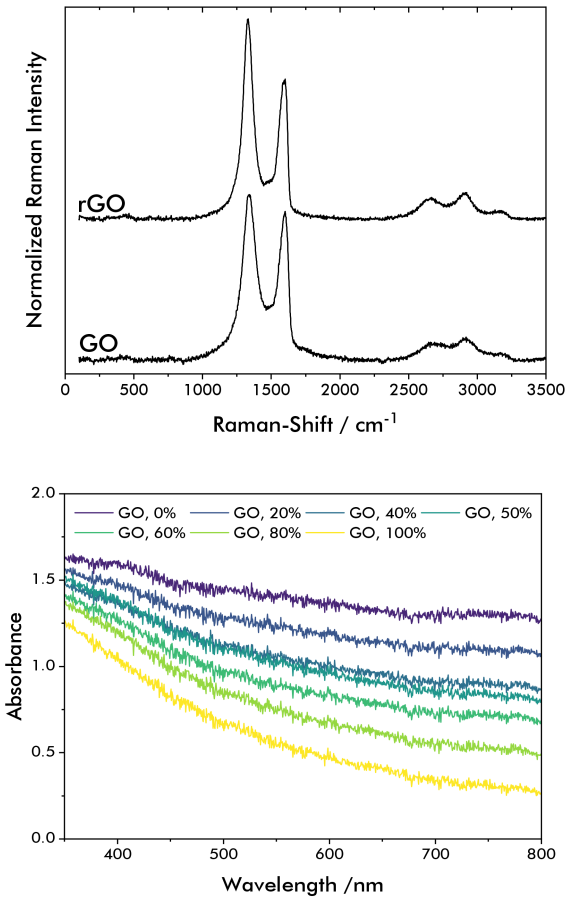

Fig. 4.3. Raman-spectra of rGO and GO. Absorbance spectra in the range of 350 – 800nm for each GO/rGO-mixture in NMP/water (20:1). NMP has a UV cut-off at $\leq$285 nm.

increasing sp^2/sp^3 ratio for the GO/rGO mixtures. A trend can be observed that shows the correlation of sp^2-carbon to absorbance at long wavelengths.

The different interaction pathways originating from the hybridization of the materials result in different binding affinities toward the purine analytes, allowing discrimination with the help of such an array. This becomes evident when comparing the binding affinities of the analytes to rGO and GO, respectively. These parameters were determined using the SPRi setup. Despite the inhomogeneous and large spots (see Figure B8), applying simple Langmuir kinetics to the obtained values shows clear differences in the materials' binding interactions in a range from 2 to 50 µM (see Figure 4.4).

For the use of the functional spots in intensity-based SPRi, they must be sensitive at the same angle of incidence. Although rGO and GO exhibit different indices of

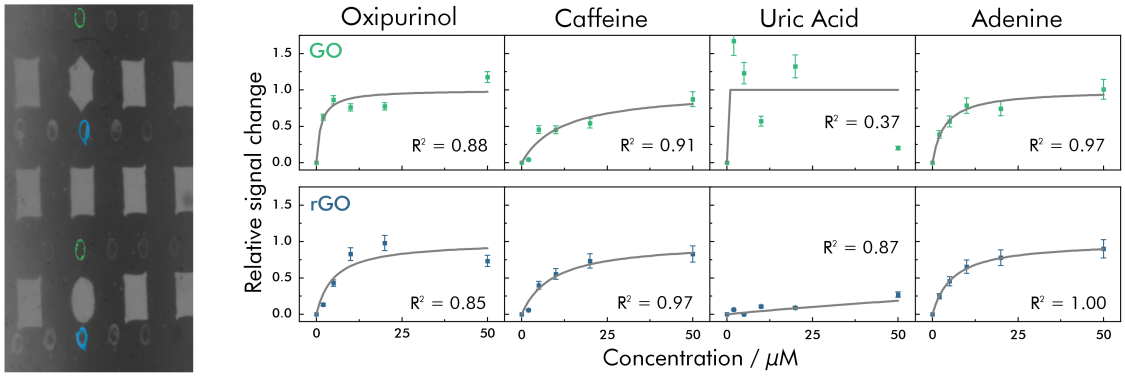

Fig. 4.4. Responses for oxipurinol, caffeine, uric acid, and adenine on GO and rGO. Pixels used for the average values are indicated in the image on the left (with an average and 3σ over a minimum of $n = 450$). Analyte responses were fitted with a Langmuir isotherm.

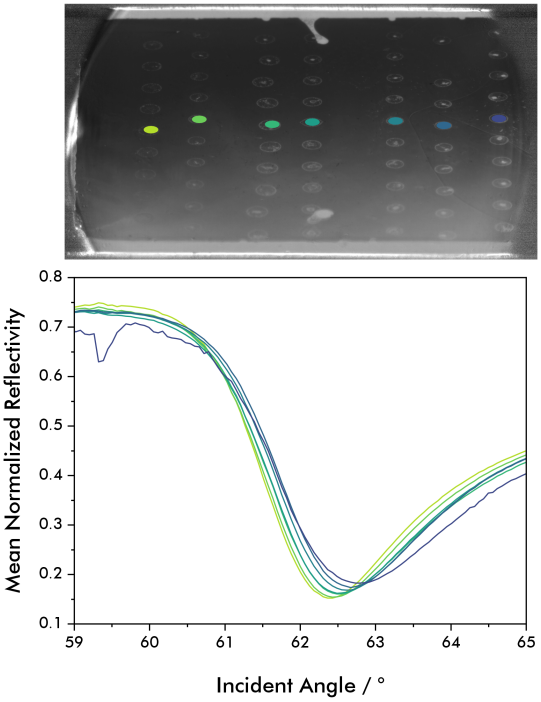

Fig. 4.5. SPR curves for the indicated deposited spots; only a minimal shift of the minimum angle can be observed.

refraction [31], the differences are expected to be small, especially for very thin films and when using mixtures of the materials. SPR curves for each mixture of GO/rGO at the same incident angle are shown in Figure 4.5.

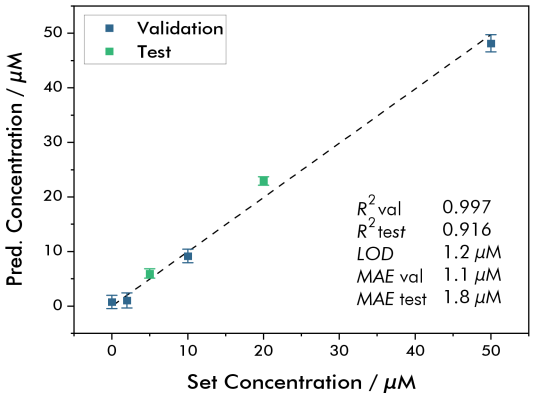

Fig. 4.6. Concentrations of adenine in a fixed solution of caffeine, uric acid, and oxipurinol as predicted by a CNN model (see Table B1). Error bars indicate triple standard deviations of the predictions over the whole dataset. Mean absolute errors for the validation data and a held-out test set are given.

In SPRi, a small range of angles is covered when employing a divergent light source, thus the information content in the SPR image is further enhanced. The angular spread across the sensing area in this setup is shown in Figure B9, by means of the maximum sensitivity. With that, it becomes evident that SPRi is in fact intrinsically multi-parametric. In addition, the different dispensed spots are heterogeneous, which leads to a multitude of different characteristics in one image. The dotted vertical line in Figure B9 shows that the SPR curve is essentially sampled in a 1° range in its slope extending over the minimum with even more variation introduced by the different characteristics obtained from the GO-/rGO-coated spots.

To take advantage of the multitude of characteristics on the sensor surface, the choice of algorithm for data processing should reflect that complexity. Therefore, machine learning was used to process the images. It is challenging to define meaningful features on an image with such heterogeneous characteristics, especially in the context of structurally similar analytes. Automatic feature extraction, e.g. with the help of a CNN, is therefore greatly beneficial.

Quantification. As a proof of principle, it was shown, that on the designed functional surface of GO mixed with rGO quantification of the purine adenine was possible with a limit of detection of 1.2 µM, calculated with a triple standard deviation of predicted concentrations and a mean absolute error of 1.8 µM of the test set data, even when subject to interference by a mixture of the structurally similar purine molecules such as caffeine, uric acid, and oxipurinol at 50 µM each (Figure 4.6).

Classification. Taking a step back, data should be carefully chosen to be able to meaningfully assess the sensor's performance. As one of the benefits of the proposed

semi-selective array is recovery of the sensor surface, repeated measurements must be evaluated.

Additionally, re-calibration for every sensor should be minimal to allow for online monitoring. To limit overfitting, it is vital for complex models to be fed with representative data. This is illustrated in Figure 4.7, where tabular data - similar to that, which was fed to the tree model - from one measurement series of a prism clusters nicely when principal component analysis (PCA) is applied. As soon as measurements, repeated on the same prism, are added to the model, the largest variance in the data is not related to the analyte state anymore, but due to other changes in the images, i.e. different positioning of the GO/rGO spots or the prism itself, which impedes effective clustering. These changes need to be presented to the model to be compensated.

In addition to representative data, the choice of model is of great importance. Automatic feature extraction is beneficial in environments where the role of each specific structure cannot be determined in advance. It also allows for a more relaxed spatial environment when using a CNN due to their shift-invariant nature. This greatly improves performance when exact positioning and composition of the spots cannot be guaranteed. In contrast, manual selection of the positions of the dispensed material requires previous inspection of new data. Further, an aggregated metric of calculating the mean across GO/rGO spots may become less meaningful when the thickness and the composition across a specific spot are not homogeneous.

Hyperparameters for the tree model and the CNN were optimized using Optuna [32]. Additionally, feature derivation for the tree model was adjusted, selecting between calculation of mean and median over the regions and subtracting or dividing the references. For the CNN-based evaluation, the colour channel number, dropout ratio, as well as the brightness augmentation was varied, yielding final hyperparameters as presented in Table B1.

The tree model seems to be capable of distinguishing the analytes to a degree in the training and validation sets based solely on the gold surface, which may be attributed to differences in bulk refractive index and a significant angle spread over the sensor surface, which can be used to eliminate some effects on the sensor signal, like changes in temperature, illumination, and on the surface.

Limitations of the tree model and the associated features become apparent when looking at the test set classification performance (see Figure 4.8), where less than 50 % accuracy was achieved.

Generalization across different prisms and measurements is challenging, which may be attributed to the feature selection procedure or limitations of the model itself.

When feeding the model with data from multiple prisms, the exact composition of a GO/rGO spot may vary since the repeatability of the dispensing process is limited. During training, there may further be variations, i.e. in the positioning of the prism

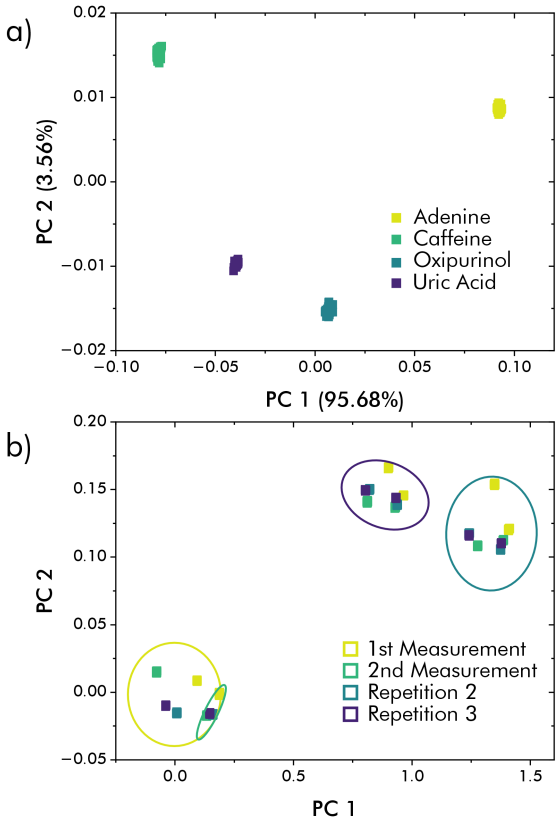

Fig. 4.7. PCA of measurement data (tabular data extracted for the tree-based model) for a single measurement (a) and several repeated measurements on the same prism (b). Different measurement conditions cause clustering, while analyte states are distributed across the PC space making it harder to extract information about analyte states.

between every measurement set as it must be re-inserted into the setup, thus also influencing the functional spot position and the incident angle of light on the surface.

The neural network yields far better generalization to an unseen sensor, reaching around 78 % classification accuracy and much better performance in the validation sets of 85 % (see Figure 4.8). To verify that the information is encoded in the GO/rGO spot intensities, another prism treated similar but with omitted functional spots was used for validation purposes. This nanomaterial-free sensor surface led to only 32 % accuracy which, for four analytes, is hardly better than random guessing. To show that insufficient domain transfer is not responsible for this significant drop in accuracy, the original test data was altered so that the dispensed spots are deleted from the images. This also leads to very low (40 %) classification accuracies. Additionally, the experimental order can be changed. Similar to the test set accuracy, 77 % accuracy was achieved when the order in which the analytes are presented to the sensor was permuted (usually **c**affeine, **u**ric acid, **o**xipurinol, **a**denine – **C-U-O-A** to

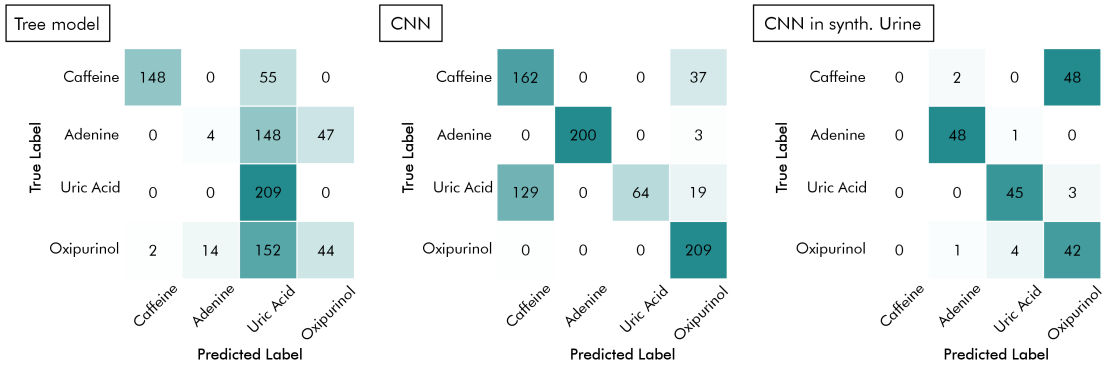

Fig. 4.8. Confusion matrix for analyte classification with the tree model and the CNN in Millipore water, and the CNN applied in synthetic urine (highest validation accuracy fold); Mainly uric acid is misclassified by the CNN in Millipore water due to its small influence on the signal when exposed to the sensor, but high recall for oxipurinol classification with a low precision can be observed. Accuracy is maintained for classification in synthetic urine, only caffeine is misclassified.

A-O-U-C and **O-C-A-U**). This shows that the trained model is robust to changes in experiment order.

To verify how robust the described sensor is to general changes in measurement conditions with respect to classification accuracies, the model was put to an endurance test. Therefore, the same model (see Table B1) was used for classification of the purine molecules caffeine, uric acid, oxipurinol, and adenine in synthetic urine. Training the model for only five epochs with additional data resulted in classification accuracies which are comparable to those obtained from the experiments in Millipore water. Caffeine was, however, misclassified. This may be attributed to either a possible interference from creatinine in the matrix or, on the other hand, generally stronger matrix effects observed within the training data for caffeine. This is indicated by the SHAP values of the model, which are shown in Figure B10. Exemplary response curves for classification measurements in Millipore water as well as in synthetic urine are provided in Figure B11.

The obtained classification accuracies for the tree model (with and without functional spots) as well as for the CNN are summarized in Table B2.

4.4 Conclusion

An SPR functional surface with an array of GO/rGO mixtures was developed, which can be used to quantify selected purine molecules in a mixture and achieves high classification accuracies among four model analytes for different measurement conditions. It was shown that graphene oxide and reduced graphene oxide as

functional materials allow label-free detection of various small molecules. The obtained signal responses mainly relate to molecules bound to these nanomaterials and less to changes in the bulk refractive index. Semi-specific and weak binding interactions varying for each surface/analyte pair were exploited to create an array of mixtures of GO/rGO, which produces unique response patterns to a given analyte. SPRi allows the analysis of entire images, showing the signal responses for these mixtures simultaneously. The image data can be fed directly to a convolutional neural network for automatic feature extraction without manual pre-processing. This proved to be the superior approach, compared to more traditional machine learning methods, where manual feature engineering is needed. The model is capable of generalizing across different measurement conditions and even unseen sensors, showing that a general relationship of sensor state and analyte state can be established. This allows the classification of molecules on new sensors, without requiring re-calibration. The sensors built within this work could be used multiple times without significant losses in classification accuracy, thus indicating good reversibility. Further, classification was achieved under heavily changed measurement conditions in synthetic urine as a proof of principle for the sensor's robustness and possible use in complex media.

The performance may be further enhanced by using models that are capable of handling larger resolution images since the high spatial intensity information is in parts lost due to the resized input in the presented work. Additionally, a neural network tailored specifically for the task of classification based on intensity ratios may be beneficial. The model is limited to the classification of the four purines caffeine, uric acid, oxipurinol, and adenine but may be fine-tuned to include more analytes or for more complex regression tasks.

References

[1] T. Wasilewski, D. Migoń, J. Gębicki, W. Kamysz, "Critical Review of Electronic Nose and Tongue Instruments Prospects in Pharmaceutical Analysis", *Analytica Chimica Acta* **2019**, *1077*, 14–29, DOI 10.1016/j.aca.2019.05.024 (cit. on p. 64).

[2] B. Aouadi, J.-L. Z. Zaukuu, F. Vitális, Z. Bodor, O. Fehér, Z. Gillay, G. Bazar, Z. Kovacs, "Historical Evolution and Food Control Achievements of Near Infrared Spectroscopy, Electronic Nose, and Electronic Tongue—Critical Overview", *Sensors* **2020**, *20*, 5479, DOI 10.3390/s20195479 (cit. on p. 64).

[3] J.-F. Masson, "Portable and Field-Deployed Surface Plasmon Resonance and Plasmonic Sensors", *The Analyst* **2020**, *145*, 3776–3800, DOI 10.1039/D0AN00316F (cit. on p. 64).

[4] D. Wang, J. Loo, J. Chen, Y. Yam, S.-C. Chen, H. He, S. Kong, H. Ho, "Recent Advances in Surface Plasmon Resonance Imaging Sensors", *Sensors* **2019**, *19*, 1266, DOI 10.3390/s19061266 (cit. on p. 64).

[5] R. B. M. Schasfoort, *Handbook of Surface Plasmon Resonance:* 2nd ed., Royal Society of Chemistry, Cambridge, **2017**, DOI 10.1039/9781788010283 (cit. on p. 64).

[6] L.-A. Garçon et al., "A Versatile Electronic Tongue Based on Surface Plasmon Resonance Imaging and Cross-Reactive Sensor Arrays—A Mini-Review", *Sensors* **2017**, *17*, 1046, DOI 10.3390/s17051046 (cit. on p. 64).

[7] M. Genua, L.-A. Garçon, V. Mounier, H. Wehry, A. Buhot, M. Billon, R. Calemczuk, D. Bonnaffé, Y. Hou, T. Livache, "SPR Imaging Based Electronic Tongue via Landscape Images for Complex Mixture Analysis", *Talanta* **2014**, *130*, 49–54, DOI 10.1016/j.talanta.2014.06.038 (cit. on p. 65).

[8] N.-F. Chiu, T.-L. Lin, C.-T. Kuo, "Highly Sensitive Carboxyl-Graphene Oxide-Based Surface Plasmon Resonance Immunosensor for the Detection of Lung Cancer for Cytokeratin 19 Biomarker in Human Plasma", *Sensors and Actuators B: Chemical* **2018**, *265*, 264–272, DOI 10.1016/j.snb.2018.03.070 (cit. on p. 65).

[9] Y. V. Stebunov, O. A. Aftenieva, A. V. Arsenin, V. S. Volkov, "Highly Sensitive and Selective Sensor Chips with Graphene-Oxide Linking Layer", *ACS Applied Materials & Interfaces* **2015**, *7*, 21727–21734, DOI 10.1021/acsami.5b04427 (cit. on p. 65).

[10] N. S. Kaya, A. Yadav, M. Wehrhold, L. Zuccaro, K. Balasubramanian, "Binding Kinetics of Methylene Blue on Monolayer Graphene Investigated by Multiparameter Surface Plasmon Resonance", *ACS Omega* **2018**, *3*, 7133–7140, DOI 10.1021/acsomega.8b00689 (cit. on p. 65).

[11] A. Zubiarrain-Laserna, P. Kruse, "Review—Graphene-Based Water Quality Sensors", *Journal of The Electrochemical Society* **2020**, *167*, 037539, DOI 10.1149/1945-7111/ab67a5 (cit. on p. 65).

[12] M. Singh, M. Holzinger, M. Tabrizian, S. Winters, N. C. Berner, S. Cosnier, G. S. Duesberg, "Noncovalently Functionalized Monolayer Graphene for Sensitivity Enhancement of Surface Plasmon Resonance Immunosensors", *Journal of the American Chemical Society* **2015**, *137*, 2800–2803, DOI 10.1021/ja511512m (cit. on p. 65).

[13] L. Wunderlich, P. Hausler, S. Märkl, R. Bierl, T. Hirsch, "Nanoparticle Determination in Water by LED-Excited Surface Plasmon Resonance Imaging", *Chemosensors* **2021**, *9*, 175, DOI 10.3390/chemosensors9070175 (cit. on p. 65).

[14] J. Funke, C. Prasse, C. Lütke Eversloh, T. A. Ternes, "Oxypurinol – A Novel Marker for Wastewater Contamination of the Aquatic Environment", *Water Research* **2015**, *74*, 257–265, DOI 10.1016/j.watres.2015.02.007 (cit. on p. 65).

[15] A. S. Malinick, D. D. Stuart, A. S. Lambert, Q. Cheng, "Surface Plasmon Resonance Imaging (SPRi) in Combination with Machine Learning for Microarray Analysis of Multiple Sclerosis Biomarkers in Whole Serum", *Biosensors and Bioelectronics: X* **2022**, *10*, 100127, DOI 10.1016/j.biosx.2022.100127 (cit. on p. 65).

[16] L. Shang, C. Liu, B. Chen, K. Hayashi, "Plant Biomarker Recognition by Molecular Imprinting Based Localized Surface Plasmon Resonance Sensor Array: Performance Improvement by Enhanced Hotspot of Au Nanostructure", *ACS Sensors* **2018**, *3*, 1531–1538, DOI 10.1021/acssensors.8b00329 (cit. on p. 65).

[17] P. Maho, C. Herrier, T. Livache, G. Rolland, P. Comon, S. Barthelmé, "Reliable Chiral Recognition with an Optoelectronic Nose", *Biosensors and Bioelectronics* **2020**, *159*, 112183, DOI 10.1016/j.bios.2020.112183 (cit. on p. 65).

[18] Q. Duan, J. Lee, S. Zheng, J. Chen, R. Luo, Y. Feng, Z. Xu, "A Color-Spectral Machine Learning Path for Analysis of Five Mixed Amino Acids", *Chemical Communications* **2020**, *56*, 1058–1061, DOI 10.1039/C9CC07186E (cit. on p. 66).

[19] J. Li, L. Zhang, A. Johnson-Buck, N. G. Walter, "Automatic Classification and Segmentation of Single-Molecule Fluorescence Time Traces with Deep Learning", *Nature Communications* **2020**, *11*, 5833, DOI 10.1038/s41467-020-19673-1 (cit. on p. 66).

[20] J. Houston, F. G. Glavin, M. G. Madden, "Robust Classification of High-Dimensional Spectroscopy Data Using Deep Learning and Data Synthesis", *Journal of Chemical Information and Modeling* **2020**, *60*, 1936–1954, DOI 10.1021/acs.jcim.9b01037 (cit. on p. 66).

[21] L. B. Ayres, F. J. Gomez, J. R. Linton, M. F. Silva, C. D. Garcia, "Taking the Leap between Analytical Chemistry and Artificial Intelligence: A Tutorial Review", *Analytica Chimica Acta* **2021**, *1161*, 338403, DOI 10.1016/j.aca.2021.338403 (cit. on p. 66).

[22] F. Cui, Y. Yue, Y. Zhang, Z. Zhang, H. S. Zhou, "Advancing Biosensors with Machine Learning", *ACS Sensors* **2020**, *5*, 3346–3364, DOI 10.1021/acssensors.0c01424 (cit. on p. 66).

[23] G. Moon, T. Son, H. Lee, D. Kim, "Deep Learning Approach for Enhanced Detection of Surface Plasmon Scattering", *Analytical Chemistry* **2019**, *91*, 9538–9545, DOI 10.1021/acs.analchem.9b00683 (cit. on p. 66).

[24] K. Thadson, S. Visitsattapongse, S. Pechprasarn, "Deep Learning-Based Single-Shot Phase Retrieval Algorithm for Surface Plasmon Resonance Microscope Based Refractive Index Sensing Application", *Scientific Reports* **2021**, *11*, 16289, DOI 10.1038/s41598-021-95593-4 (cit. on p. 66).

[25] S. Eigler et al., "Wet Chemical Synthesis of Graphene", *Advanced Materials* **2013**, *25*, 3583–3587, DOI 10.1002/adma.201300155 (cit. on p. 66).

[26] H. Feng, R. Cheng, X. Zhao, X. Duan, J. Li, "A Low-Temperature Method to Produce Highly Reduced Graphene Oxide", *Nature Communications* **2013**, *4*, 1539, DOI 10.1038/ncomms2555 (cit. on p. 66).

[27] D. Konios, M. M. Stylianakis, E. Stratakis, E. Kymakis, "Dispersion Behaviour of Graphene Oxide and Reduced Graphene Oxide", *Journal of Colloid and Interface Science* **2014**, *430*, 108–112, DOI 10.1016/j.jcis.2014.05.033 (cit. on p. 66).

[28] S. Grimm, M. Schweiger, S. Eigler, J. Zaumseil, "High-Quality Reduced Graphene Oxide by CVD-Assisted Annealing", *The Journal of Physical Chemistry C* **2016**, *120*, 3036–3041, DOI 10.1021/acs.jpcc.5b11598 (cit. on p. 68).

[29] K. He, X. Zhang, S. Ren, J. Sun, Deep Residual Learning for Image Recognition, **2015**, DOI 10.48550/arXiv.1512.03385 (cit. on p. 69).

[30] S. Xie, R. Girshick, P. Dollár, Z. Tu, K. He, Aggregated Residual Transformations for Deep Neural Networks, **2017**, DOI 10.48550/arXiv.1611.05431 (cit. on p. 69).

[31] G. G. Politano, C. Versace, "Electrical and Optical Characterization of Graphene Oxide and Reduced Graphene Oxide Thin Films", *Crystals* **2022**, *12*, 1312, DOI 10.3390/cryst12091312 (cit. on p. 71).

[32] T. Akiba, S. Sano, T. Yanase, T. Ohta, M. Koyama in Proceedings of the 25th ACM SIGKDD International Conference on Knowledge Discovery & Data Mining, ACM, Anchorage AK USA, **2019**, pp. 2623–2631, DOI 10.1145/3292500.3330701 (cit. on p. 73).

Chapter 5

Applications of Multi-Parametric Surface Plasmon Resonance Imaging

The development of sensors using surface plasmon resonance can be challenging due to the high variety of surface modifications and analyte-receptor interactions involved in detection. Careful and continuous evaluation is key to success which requires as much information as possible. Multi-parametric surface plasmon resonance imaging (MP-SPRi) can provide higher dimensional data leading to more nuanced and reliable information. This can be used to assess sensor performance with less measurement expense. In this chapter, several practical examples are presented that utilise MP-SPRi to increase information content extracted from measured data.

5.1 Introduction

Sensors based on surface plasmon resonance need to be optimised for the analytical task. This involves a choice of recognition element that associates with the analyte of interest. Often-times, immobilisation of the receptor is a critical step and has to be carefully evaluated during sensor development [1]. The immobilisation process, in practice, is usually imperfect where the density of recognition element is non-constant across the sensor surface [2]. Additionally, the interaction potential of the recognition element with the analyte is not always known a priori, especially for semi-selective surface modifications that can bind to several different analyte molecules.

Therefore, screening of surface modifications and their effectiveness is important for the efficient development of chemo- and biosensors [3, 4]. Imaging techniques can provide spatially resolved information on the surface, particularly SPR imaging due to its high sensitivity at close proximity to the surface delivers valuable insight [5, 6]. Conventional SPRi, however, is limited in two ways: the angle of incidence is constant across the surface which results in varying sensitivity for different modifications and there is no absolute information on the surface state available.
In detail, different modifications result in different optimum angular settings for maximum sensitivity. This effectively reduces the usable signal if multiple different functional areas are imaged since not all regions can be recorded under optimal conditions simultaneously. In order to compare the different regions in a referenced manner, a calibrated change has to be introduced or experiments have to be conducted consecutively under varying optimised conditions.
Equally, no absolute information on the surface is available, only relative changes are recorded. Thus, surface state (i.e. receptor density, surface loading, ...) can only be inferred from time-consuming calibration. During sensor development the receptor density may be unknown, similarly the interaction strength between analyte and recognition element can be a variable in the particular configuration. Both can only be determined in reference to a calibrated signal change or with a series of concentration measurements [7].

Multi-parametric surface plasmon resonance imaging can provide insights into the measurement system and the sensor surface state. Notably, different surface modifications can be used under ideal conditions (i.e. maximum sensitivity) so that several

different receptors can be used effectively simultaneously. Additionally, surface loading can be estimated from fitting measurement data to a calibrated sensor surface as described in section 3.2.2.2. In this chapter, multiple examples for enhancing measurements using MP-SPRi in different settings are provided.

5.2 Fast Surface Mapping

The first insight into surface modifications can be gained by analysing the SPR curve. It can be acquired for every pixel in the image resulting in fast recording of a multitude of SPR curves and provides information about the surface composition across the sensor.

5.2.1 Methods

All prisms in this chapter were purchased from Gräfe Spezialoptik GmbH (Hamburg, Germany) with a 62° base angle and a 18 mm x 18 mm surface area. Measurements in aqueous solution were conducted using SF2 glass (Schott AG, Mainz, Germany) while oil-based measurements were carried out with N-SF6 glass. Metallisation was done by Creavac (Dresden, Germany) with 49 nm gold deposited onto a thin adhesive layer as specified in section C.1 via chemical vapour deposition.

Three variants of surface blocking for creating a graphene-based sensor array were evaluated. Thus, three prisms were prepared:

- On the first reduced graphene oxide (rGO) and graphene oxide (GO) in different mixtures (similar to chapter 4) were dispensed as an array directly on top of the gold surface using a dispenser (Musashi ShotMini 200 Sx, Japan) and the remainder of the surface was subsequently blocked using hexadecane-1-thiol.
- The second prism was prepared with a reversed protocol where the surface was first treated using the thiol and the graphene array was dispensed on top.
- The third prism was modified with chemical vapour deposition (CVD) graphene wet-transferred onto the prism [8] and the rGO/GO array was dispensed after.

SPR images throughout the chapter were acquired using a 660 nm or 730 nm LED (GH CSSRM2.24 or LZ1-00R302, ams-OSRAM GmbH, München, Germany) light source, collimated with the help of a 50 mm focal length aspheric lens (66-025, Edmund Optics, Barrington, USA), a 10 nm full-width half maximum wavelength filter, and a polariser (86-089, 65-176, and 47-216, Edmund Optics, Barrington, USA) mounted in a rotary mount (K10CR2, Thorlabs Inc., Newton, USA) for illumination and a 100 mm objective lens mounted to a 14-bit camera (67-715, and BFS-U3-63S4, both Edmund Optics, Barrington, USA) for image acquisition. Optical components

were mounted with a cage system and illumination and acquisition can be rotated using a motorised linear stage (OWIS GmbH, Staufen im Breisgau, Germany) with respect to the reflector (the prism) to vary the incidence angle. The collimating lens was placed slightly off-focus to create a divergent beam with a few degrees spread in incidence angle across the prism surface. For a rendering of the setup see Figure B5.

Angle scans with p and s-polarised light were acquired in water by adjusting the outer angle of incidence using the linear stage in 0.1° intervals. The images were aligned using homographic projection to match in their dimensions and positions using the 62°-image as base image. Dividing the images taken with p-polarised light by the respective images using s-polarised light a referenced SPR curve for every pixel can be observed. The minimum map is obtained by finding the minimum in the SPR curve for each pixel.
Due to the illumination with divergent light the SPR curve is shifted in one image dimension (vertically in the images shown in this chapter). This can be corrected by linearly fitting the SPR curve minimum value to the prism position. Finally, a corrected SPR curve minimum map is obtained.

5.2.2 Results and Discussion

The minimum map can be viewed as an additional representation of data provided by the imaging setup, similar to a phase image in light microscopy. It immediately reveals that the order of immobilisation is important for the size of the dispensed rGO/GO areas as well as their thickness which is visible as a shift in minimum angle (Figure 5.1). Although the spots are visible when the blocking thiol is administered before the receptors, the material seems to be largely focussed onto a smaller area which complicates data processing. In the case of CVD graphene, the receptor spots become barely distinguishable due to the similarities between base (CVD graphene) and dispensed material (rGO/GO). Additionally, transferring large CVD graphene sheets proved difficult and signifant tearing is visible in the examined specimen. For the application as a receptor array, the dispensed spots should occupy as much space as possible on the sensor and they should be homogeneous, i.e. the angular distribution has uniform as possible.

The minimum map thus allows for quick assessment of surface modifications that need to be optimised for sensing. Additionally, the data can be used for further processing, e.g. by segmentation on the basis of the mininimum map. An exemplary segmentation is shown in Figure 5.2 created directly with Segment Anything [9] on top of the minimum map (Figure 5.1 a). The result can be used to determine the homogeneity of the surface modifications like shown in Figure 5.2 b, where the previously segmented regions which represent different mixtures of rGO and GO are plotted in terms of minimum angle distribution.

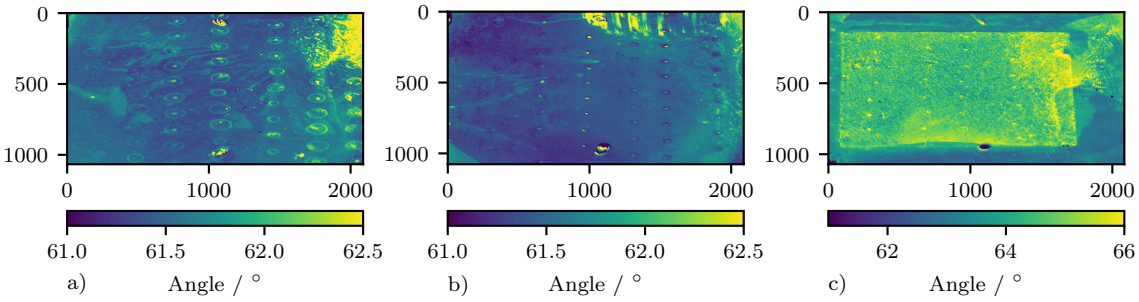

Fig. 5.1. Minimum of different surface modifications, with dispensed rGO/GO followed by hexadecane thiol (a), a reversed protocol (b) and the graphene oxides dispensed on top of CVD graphene. In (a) the dispensed spots can be distinguished from the background and occupy more space than in (b). Larger area receptors can be used to decrease measurement noise by spatial averaging. Brighter areas towards the upper left of the image are due to surface impurities.

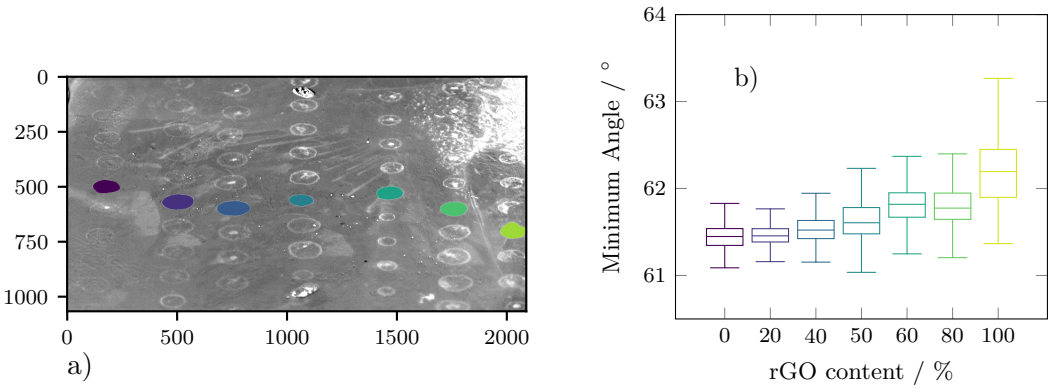

Fig. 5.2. Segmentation mask generated automatically based on Figure 5.1 (a), one receptor position for every rGO/GO mixture was selected by visually choosing an arbitrary point on the spot and subsequent segmentation. The minimum angle distribution for the selected spots is show in (b). With rising rGO content the distribution shifts to higher angles, which can be expected due to the more continuous graphene surface.

From the SPR curve for every pixel, a maximum sensitivity can also be isolated. This can function as a basis for selecting a suitable angle during further experiments. When using MP-SPRi a range of angles is probed simultaneously so that this selection is not exclusive. This means that even though the optimum angle for a specific surface modification is chosen the residual area can still be evaluated under ideal sensitivity conditions (see following section).

5.3 Sensitivity Mapping

Lateral information can be used to provide insight into the spatial distribution of signal change when introducing an analyte. To demonstrate the capabilities three different applications are presented.

The analysis of water and possible pollutants is of substantial importance to understand the limits of wastewater treatment and provide scientific basis for their improvement [10]. Anthropogenic pollutants can serve as model analytes for water treatment shortcomings as they are not expected to develop naturally. Pharmaceutical residues or derivates (e.g. oxipurinol), industrial sweetener (e.g. acesulfam), and pesticides (e.g. glyphosate) can be exceptionally useful [11–13]. For some of these analytes SPR sensors have been reported [14]. However, combined detection of several pollutants would simplify tracking issues with wastewater treatment.

Electrical transformers can fail catastrophically if not maintained meticulously. This is often the result of transformer oil degrading through oxidation. Transformer oil lifetime can be extended by adding phenol-based inhibitors [15, 16]. Therefore, tracking inhibitor content in transformer oil over the course of their lifetime is an active area of research [17, 18]. It was reported that phenolic compounds can adsorb to graphene [19] and graphene oxide [20] which is why their interaction potential was probed with the help of SPR.

Finally, the antibiotic content in milk (exemplary using Kanmycin A) is examined, the background of which is expanded on in section 5.4.

5.3.1 Methods

2D materials were immobilised as described in the previous section using a dispenser. Here, the measurements in aqueous solution feature a selection of several materials (graphene oxide, reduced graphene oxide, boron nitride, molybdenum disulfide) and the measurements in oil were performed using a prism with graphene and reduced graphene oxide dispensed alternating three times each.
The last example was recorded using a prism where a striped pattern was imprinted using a PDMS stamp with 200 µm stripe thickness. The stamp was applied to the prism while partly (approximately half) submerging the prism in triethyleneglycol mono-11-mercaptoundecylether (PEG) for 24 hours and the other half equally in hexadecane-1-thiol (THIOL) afterwards. The previously covered surface was then functionalised with 16-sulfanylhexadecanoic acid by submerging it wholly. The thiols were prepared in 200 µmol L^{-1} ethanolic solution. The hexadecanoic acid was functionalised further by addding a solution of 4 mmol L^{-1} 3-[(ethylimino)methylidene]amino-N,N-dimethylpropan-1-amine (EDC) dissolved in a 10 mmol L^{-1} NaCl solution for 30 minutes and a solution of anti-kanamycin aptamer (APTA) for 60 minutes thereafter rinsing thoroughly with NaCl solution. This results in a striped

pattern with alternating aptamer and ethylene gylcol on one half of the prism and aptamer/hexadecane on the other half.

Sensitvity maps were created by relating the change in intensity after analyte addition to the change when adding a refractive index calibration solution (200 mmol L^{-1} NaCl solution).
The signal-to-noise ratio was calculated by relating the signal change after analyte addition to the signal variation during flushing of the sensor with buffer solution.
Data fits were calculated by first taking average steady-state images for six different Kanamycin A concentrations (0, 2, 5, 10, 20, 100) µM and segmenting the different functional areas using a random forest classifier on edge and texture information of difference images. Every pixel value for the different concentrations functionalised with aptamer was then referenced with an appropriate close pixel that has been blocked (by either hexadecane-1-thiol or triethyleneglycol mono-11-mercaptoundecyl-ether). The referenced intensity values were then fitted to a Langmuir model (see Equation 2.8) to evaluate the receptor performance after immobilisation. The segmentation was used as a mask for the computation, omitting areas with bad signal-to-noise ratio and artefacts of the measurement.

5.3.2 Results and Discussion

As a means to assess the interaction of different 2D materials with pollutants in water, the average signal change after successive addition of 200 µM oxipurinol, acesulfam K, glyphosate, and trinitrophenol was calculated from the measurement. This served as a pre-assessment of which 2D material may be applicable to a detection system for small molecules in water.
The resulting sensitivity map (Figure 5.3) can be used to identify which material results in the largest signal change. It is vital that there is an angular modulation across the sensor surface when several different materials are evaluated simultaneously since their optimum angle is vastly different. Angular modulation allows recording the ideal sensitivity for every material during one experimental run. Here, graphene oxide (left-most structure, blue box) has the highest sensitivity towards the lower area of the sensor while reduced graphene oxide and the gold surface are more sensitive in the upper area of the sensor (yellow outline). Thus, recording the data at an angle suitable for the gold surface would significantly under-estimate the sensitivity of graphene modified areas.

Similarly, the sensitivity can be used to identify if a specific detection system is working as intended. Graphene oxide and reduced graphene oxide were once more employed in an attempt to quantify the phenol-based antioxidant in transformer oil. The sensitivity was expressed as a signal-to-noise ratio (Figure 5.4). Again, the angular information allows a more nuanced interpretation of data. In isolation the signal-to-noise ratio of the (rGO) receptor regions seems superior, however, it is actually not significantly higher than the sensor surface itself when compared

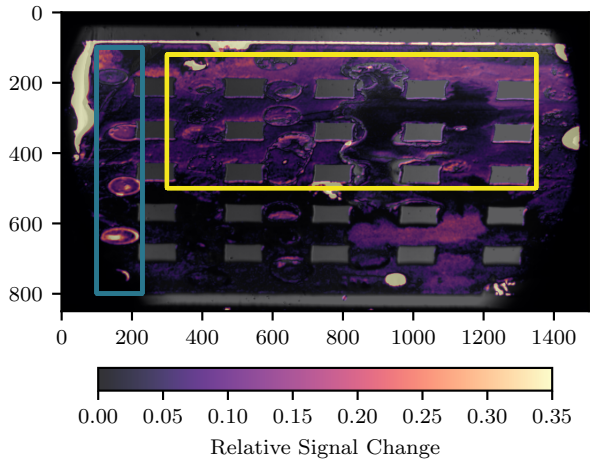

Fig. 5.3. Average sensitivity map for a 2D material array after introduction of four analytes to the sensor surface relative to the signal change generated with a buffer solution. High sensitivity areas for graphene oxide (lower left) are significantly different in optimum angle compared to the background (gold, top area). Different materials exhibit different optimal sensitivity positions. Rectangular grey structures are mirrors, i.e. thick gold ($\approx 200\,\mathrm{nm}$) used to correct changes in intensity.

fairly, i.e. at their respective ideal angles which can differ by a few hundred pixels in vertical direction (see Figure 5.4 b). The receptor surface has higher variance in signal-to-noise ratio than the blank surface due to the inhomogeneous dispensing process but the average of the distribution is not higher which means that no significant effect of the receptor towards the analyte could be detected.

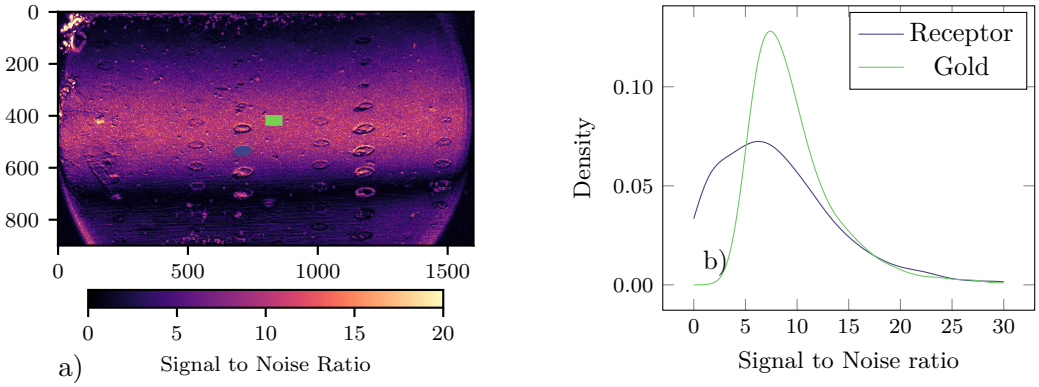

Fig. 5.4. Signal to noise ratio for inhibitor introduced to a sensor array, where the magnitude of the rGO areas is not significantly higher than the background (gold) surface. The results of which can be misinterpreted without angular spread. The signal-to-noise ratio varies vertically due to the changing angle of incidence. The distributions of the marked areas in (a), which are approximately the same size and span the same amount of pixels vertically, do not differ significantly (b).

The setup can be exploited to efficiently gather as much information as possible during a single experiment by optimising surface modifications. Figure 5.5 shows a preliminary study to assess the surface modifications for the detection of kanamycin in milk. Two different blocking agents were utilised: ethylene glycol (left side) and hexadecane (right side), which resulted in different contrast between the areas where the surface was blocked and where the aptamer was immobilised (appearing brighter). Higher contrast is desirable since it indicates better blocking of unspecific binding on the blocked surface.

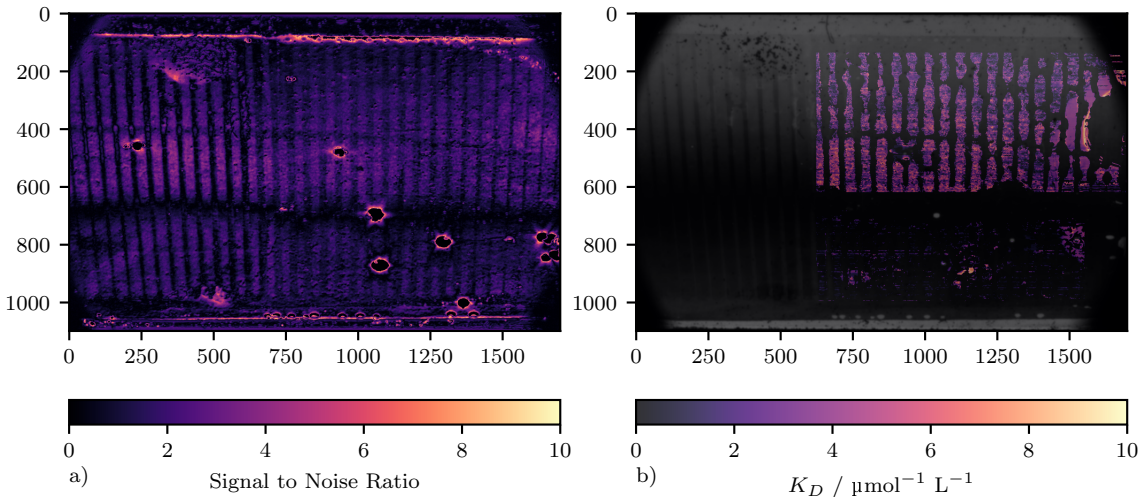

Fig. 5.5. Signal to noise ratio when pumping kanamycin over a structured surface (a), brighter areas correspond to the areas where kanamycin-specific aptamer was immobilised. Two different blocking agents were administered in between the striped pattern where the left half (ethylene glycol) shows less interaction with the analyte solution. Artefacts in the measurement are due to stabilised air bubbles forming. The fit result using concentration data and Langmuir kinetics are shown in (b). The area was restricted to the hexadecane side due to the differences in sensitivity on the left side which makes referencing more challenging.

The surface was segmented into the different functional areas and a binding curve was fitted to a concentration measurement using steady-state data. The result is depicted in Figure 5.5 b, which represents a map of observed dissociation constants. The calculation was restricted to the hexadecane area due to the vastly different sensitivities on the ethylene glycol side as evident from the response in the projected angular region (Figure 5.6 a). They are depicted in Figure 5.5 b and can be used to estimate an average dissociation constant for the aptamer-kanamycin interaction (Figure 5.6 b). The variance is very high which is a consequence of the inhomogeneity of the surface and the pixel size that leads to integration of larger areas. The determined value lies in between values previously reported [21, 22].

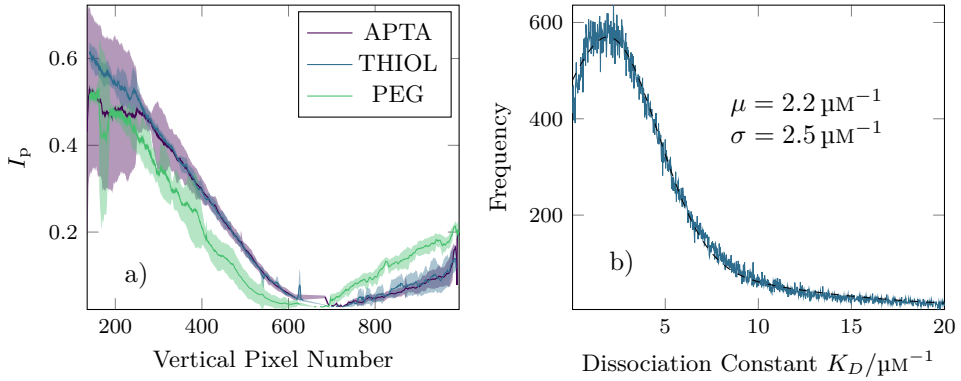

Fig. 5.6. Analysing the striped sensor surface, large differences between the SPR curve minimum of the ethylene glycol area (PEG) and the area where aptamer (APTA) was immobilised can be observed. The curves represent the average intensity in horizontal dimension for different areas, the shaded area represents the lateral standard deviation of intensity. At the curve minimum, the segmentation of the surface areas becomes infeasible due to the low signal changes which results in missing values in the graph. The hexadecane area (THIOL) barely differs from the aptamer area (a). A distribution of dissociation constants can be obtained when fitting the experimental data to a Langmuir isotherm (b). The distribution was fitted to a gaussian, resulting in a mean value for the dissociation constant of $2.2\,\mu mol\,L^{-1}$ with relatively high standard deviation (σ) which can be attributed to the inhomogeneous surface.

5.4 Surface State Tracking

Antibiotics have been used to combat diseases in livestock on dairy farms for decades [23]. The ubiquitous use of antibiotics as prophylaxis or for drug therapy can have several adverse effects on dairy, cattle, and consumers. Misuse of antibiotics can cause resistances, allergic reactions, disturbances of intestine microflora, and other dangers towards the health of livestock and consumers of milk-based products with antibiotic residues. Additionally, the dairy industry is dependant on the use of bacteria for milk derivative products which is impeded by antibiotics [24].
Regulators have begun restricting the use of pharmaceuticals, e.g. with EU Regulation 37/2010 which lists several antibiotics and their maximum residual concentration in food. Kanamycin A, as an example, in milk must not exceed $150\,\mu g\,kg^{-1}$. For these regulatory limits to be effective they have to be monitored so that compliance is at all possible.

Consequently, research activity towards fast and accurate on-site detection of antibiotics in milk has been high [25, 26]. Many of these biosensors apply aptamers for detection due to the possibility of tailor-made aptamers with high specificity and affinity towards the analyte [27, 28]. Sharma et al. used a printed carbon electrode modified with a carboxyphenyl where kanamycin-specific aptamer (5'-TGG GGG

TTG AGG CTA AGC CGA-3', [29]) was immobilised with the help of amide bonds after EDC/NHS activation [30]. They obtained a limit of detection of kanamycin in milk of 0.11 ng mL^{-1}. More sensitive detection was achieved with the help of a fluorescence probe attached to the aptamer sequence that is quenched by Förster resonance energy transfer (FRET) in the absence of kanamycin due to efficient coupling to gold nanoparticles [21]. The aptamer, normally exhibiting random-coiled conformation, forms a hairpin structures upon interaction with the analyte. Kanamycin in milk was also detected with an SPR sensor utilising graphene for signal enhancement [22].

The potential of aptamer-based kanamycin sensors has been thoroughly demonstrated. In this section, the application of MP-SPRi for kanamycin detection is explored which enables determination of surface state and disentangling bulk refractive index and adsorption of analytes [31]. To this end, an SPR imaging setup with a divergent LED light source to modulate the angle of incidence across one dimension of the image is employed. This allows for SPR curve tracking during the adsorption of kanamycin to the aptamer-modified surface.

5.4.1 Methods

Chemicals were purchased from Merck (Merck KGaA, Darmstadt, Germany) unless specified otherwise. Functionalisation was done in two steps:
The prisms were submerged overnight about halfway in a 200 µmol L^{-1} ethanolic solution of triethyleneglycol mono-11-mercaptoundecylether to create a protein-resistant surface while the other half was subsequently submerged in a 200 µmol L^{-1} solution of 16-sulfanylhexadecanoic acid.
For immobilisation the latter half was submerged in 1.8 mol L^{-1} 3-[(ethylimino)-methylidene]amino-N,N-dimethylpropan-1-amine (EDC) dissolved in a 140 mmol L^{-1} NaCl solution for 10 minutes and subsequently submerged in aptamer solution for 30 minutes after rinsing thoroughly with NaCl solution. The 24-base aptamer (5'-AGA TGG GGG TTG AGG CTA AGC CGA-3') with an amino-C6 group at the 5' terminal was purchased from Eurofins Genomics GmbH (Ebersberg, Germany) and dissolved in 10 ml of the NaCl solution to a molar concentration of 12.2 µmol L^{-1}. The two halves are referred to as OEG and aptamer-terminated (APTA) throughout the remainder of this text.

Buffer solution was prepared with 25 mmol L^{-1} 4-(2-Hydroxyethyl)piperazine-1-ethanesulfonic acid (HEPES) buffer at pH 6.7 with an addition of NaCl to match the pH and refractive index of milk. Regeneration solution was made from 50 mmol L^{-1} sodium carbonate in buffer solution.
Ultra-heat treatment milk at 1.5 % fat (Berchtesgadener Land eG, Berchtesgaden, Germany) was purchased from the store and used directly after addition of 1ppmV Tween 20 and Kanamycin A at different concentrations (0.5 µM to 20 µM). The pH of the milk was determined to 6.73, the refractive index of milk and buffer was found to 1.35017 and 1.34966 using a refractometer (Krüss, Hamburg, Germany), respectively.

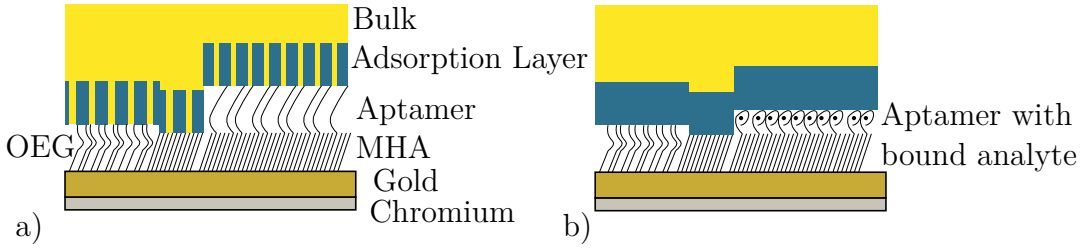

Fig. 5.7. Surface Model used for MP-SPRi calculations. In (a) the initial condition is depicted where the adsorption layers are universally set to the bulk refractive index. At the right hand side (b), the state after binding is sketched where non-specific binding has led to adsorption on all surfaces and kanamycin is bound to the aptamer.

Initially, angle scans with p and s-polarised light were acquired. Then a concentration series was conducted by measuring at a fixed angle (62°) that was identified during the angular scan. The different milk concentrations were pumped through the measurement chamber with a flow of 100 µL/min in the following sequence: buffer solution, raw milk, milk with kanamycin. This sequence was repeated for every concentration step. Regeneration of the receptors was attempted after a full concentration cycle with the sodium carbonate solution but no change in response was observed.
During angular scans i.e., rotation of the illumination and image acquisition with respect to the prism, the resulting image gets scaled due to changes in viewing angle. The images were corrected to 62° incidence with the help of homographic projection. The images from the individual time points were fitted to the surface model with several steps (compare section 3.2.2.1). From the angular scan, the metal parameters as well as the angular distribution modelled as a two-dimensional polynomial were determined. Then the intensity distribution on the sensor surface is calculated by fitting a two-dimensional gaussian to the s-polarised images of the angular scan. The full model was then used to predict the bulk refractive index and a modelled adsorption layer refractive index for the functional surfaces on the sensor for every recorded image (Figure 5.7). The image was laterally sub-sampled with a stride of ten pixels to limit computational load.

5.4.2 Results and Discussion

When analysing the angular scans of the sensors, it becomes immediately visible, that the immobilisation results in two distinct areas: the OEG (left) and the aptamer-terminated area (APTA, right). From the minimum maps, three (less) distinct areas should be identifiable: the OEG-terminated area, the area where the aptamer solution did not reach, thus resulting in a 16-sulfanylhexadecanoic acid or MHA-terminated area, and the aptamer-bound region.
However, from looking at the minimum map, this observation is not easily made (Figure 5.8). In fact, even when transforming the vertical cuts of the image to embedding-space using Minimum-Distortion Embedding (MDE) [32], there seems

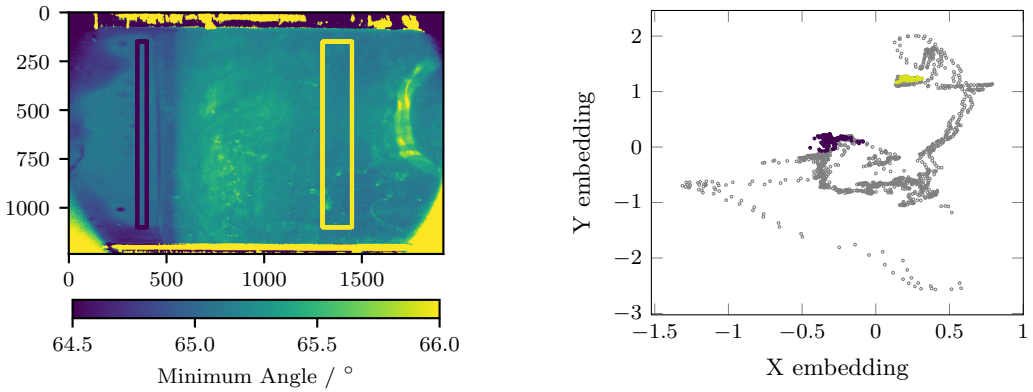

Fig. 5.8. Corrected minimum map of the sensor surface where OEG was immobilised on the left (border roughly at 500) and the aptamer was immobilised on the right side. The areas where data has been extracted from the surface is highlighted. The vertical cuts were transformed to embedding space via MDE and the highlighted areas visualised in this plot.

to be a gradual transition from a very clearly distinct OEG-terminated area to the APTA area. This aptamer-terminated area appears to be higher variance than its OEG counterpart and no distinct border between aptamer-free MHA and the aptamer area can be isolated (Figure 5.8).
The three areas can be characterised with the help of their angle-modulated curves. The Fresnel formalism with multi-layer surfaces was applied, choosing layer structures as indicated in Figure 5.7. The adhesion layer of chromium and the gold layer thicknesses and refractive indices, as well as the bulk refractive index were fitted globally. The three areas are then defined by additional intermediate layers. The OEG area is defined by an undecanol layer, a tri(ethylene glycol) layer and an adsorption layer with a thickness of 3 nm that is set to the bulk refractive index during calibration. The MHA-terminated area is comprised of a hexadecanethiol and a similar adsorption layer. The aptamer-terminated area equally has a hexadecanethiol chain followed by an aptamer layer and an adsorption layer. The initial layer parameters for the three areas are summarised in Table 5.1.
Due to the observed pattern of the minimum map where the OEG surface is visible but the aptamer area can not be distinguished clearly from the MHA area, it has to be assumed that aptamer coverage is rather low. With a coverage of one tenth of the theoretical optimum density, the simulation leads to curves that are barely distinct, especially considering the surface is not perfectly homogeneous. Peculiarly, when low coverage for the aptamer area is assumed, the OEG area has to be imperfectly ordered to explain the large difference between the OEG area and the MHA/aptamer area. Consequently, the surface state cannot be sufficiently determined since the MHA area is not distinguishable and the OEG density is unknown.
As an estimate of the maximum change that can be expected due to binding of the analyte to the aptamer, it was assumed that the OEG surface is as dense as possible while the lack of difference between MHA and APTA surface was ignored by

Tab. 5.1. Initial model parameters for the three functional surfaces used during fitting.

Surface area	Layer Name	Refractive Index	Thickness / nm
OEG	undecanol tri (ethylene glycol)	1.44 [34] 1.43 (estimate)	1.21 [35] 0.843 [35]
MHA	hexadecanol	1.43 [34]	1.76 [35]
APTA	hexadecanol aptamer	1.43 1.52	1.76 2.5 (estimate)
entire surface	adsorption layer	n_{bulk}	3

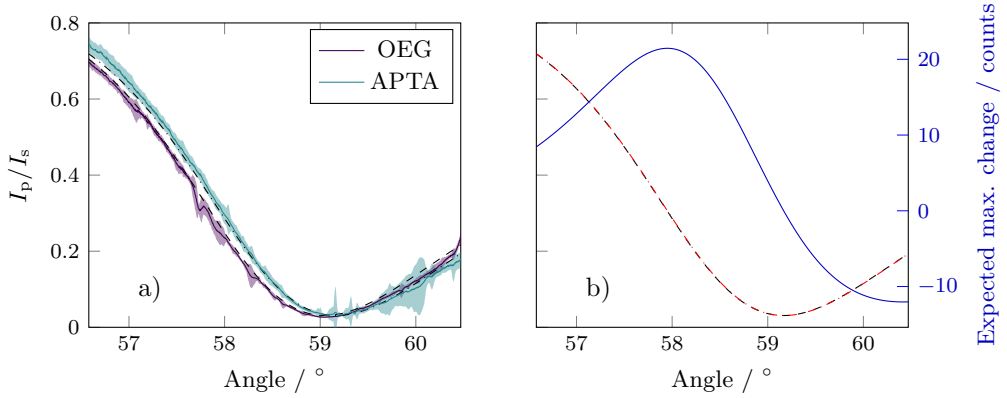

Fig. 5.9. (a) Fit of the models for OEG and APTA surface to the measured data across the sensor as indicated in Figure 5.8. Note that the area is represented as a mean reflectivity across the horizontal dimension and the fit data is likewise. In (b) the expected change due to kanamycin adsorption is presented, the blue curve represents this change when assuming that the camera's full scale output is equal to unity reflectivity.

omission of the MHA surface in the model. The surface density of the aptamer can then be estimated to $1.16 \times 10^{14}\,\mathrm{m}^{-2}$ and a maximum response can be predicted by assuming perfect binding of the analyte to the receptor, and changing the refractive index of the functionalisation layer as indicated in Figure 5.7 together with the Lorenz-Lorentz equation (Equation 2.20) and the refractive index of kanamycin (1.67, [33]). The result is a very low expected change of approximately 20 counts at maximum sensitivity when assuming full scale output of the camera relates to unity reflectivity (Figure 5.9 b).
Since the aptamer density has to be assumed to be rather low and is probably lower than this upper estimate, the expected signal change is lower and may even be insufficient for detection. The time traces for individual regions of interest and with the help of fitting the SPR response to the surface suggest that the analyte cannot

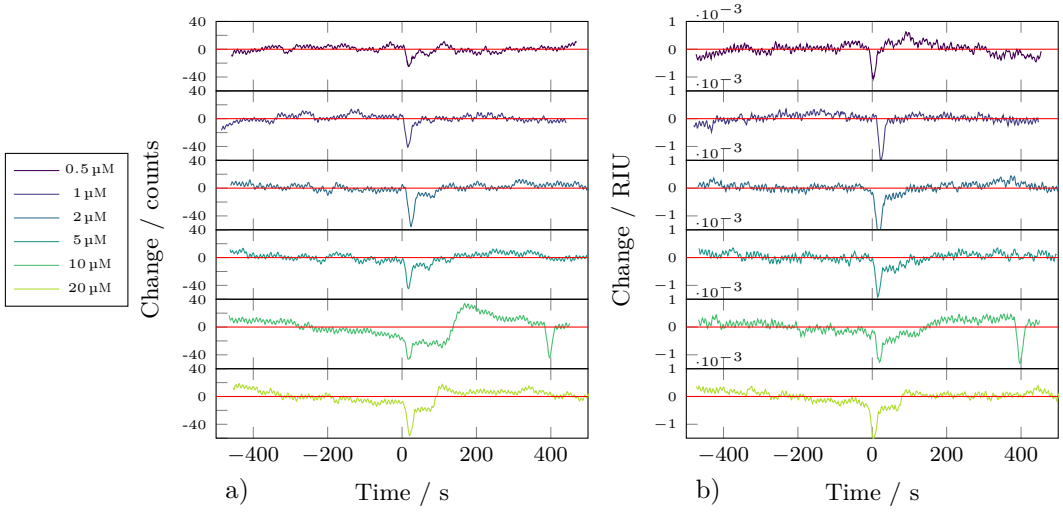

Fig. 5.10. Time traces of kanamycin addition experiment, where zero relates to the injection time of the spiked milk samples with concentrations as indicated. In (a) the average change at a specific subset of the image is depicted where the sensitivity is the largest, whereas in (b) the model output change in refractive index is featured. Although there is a change visible for concentrations greater than 5 µM, it does not follow the expected exponential shape and ultimately reverts to zero.

be detected with this sensor setup (Figure 5.10). The average intensities for the regions of interest were referenced with suitable OEG area regions (i.e. regions of similar sensitivity). The adsorption layer for each surface area was allowed to vary individually while additionally the bulk refractive index was allowed to change. Here, the adsorption layer refractive index change is shown for the APTA area. Data from both methods match nicely, but no change that can be associated with a typical binding curve can be identified with either method.

There are several reasons for these rather unimpressive results. The sensor surface is not homogeneous before immobilisation of the receptor which is clearly visible from optical inspection of the prisms. The surface quality affects the homogeneity of immobilised receptors and the signal quality of the SPR curves imaged from the sensor surface.
Additionally, the efficiency of immobilisation has to be very high to reach good surface coverage which cannot be guaranteed due to the applied protocol. Possible improvements to the immobilisation protocol involve: adjusting the pH of the EDC solution to more acidic conditions, adjusting the pH of the aptamer solution to more basic conditions, applying N-hydroxysuccinimide esters (NHS) together with EDC as the O-acylisourea intermediate of EDC coupling is unstable, and using higher concentration of aptamer. However, very high density of aptamer can also impede capturing of the analyte since the conformation change of the aptamer requires space [36]. This means that immobilisation needs to be carefully optimised.
Furthermore, the expected change due to capturing of kanamycin with ideal receptor

density is still very low and requires high signal-to-noise ratios to reliably determine the changes (Figure 5.9 b). Responses close to zero have been reported before due to the small effect of low molecular weight analytes and the conformational changes of the aptamer [37]. Conversely, small molecules may have a larger effect than anticipated since the assumption of isotropic layers may be inaccurate [38]. This can result in changes that exceed the predicted response due to binding of the analyte to available sites and a corresponding change to the reflectivity [39]. MP-SPRi can help to identify those cases since an angular response is available and any deviation from the predicted model may be indicative of those cases. However, a larger molecule would be more appropriate to assess the performance of the algorithm to disentangle refractive index changes and binding. Indeed, the approach will only work for large changes under low noise.

5.5 Conclusion

This chapter shows how additional information can be used to benefit analytically, either by an increase in information or confidence. Optimal receptors, and detection systems have been identified and characterised. However, it is important to understand the limitations of these methods. Due to the angular modulation in one dimension of the sensor surface it is not advisable to modify the surface modification in this dimension. This reduces the available sensor area by a large amount but at the same time allows for repetition and therefore averaging of data. Additionally, when trying to model the surface state as presented in section 5.4, the sensor has to be calibrated as described previously in section 3.2.2.1. When several sensors are fabricated similarly using chemical vapour deposition for metallisation, it may be sufficient to perform this calibration process once for a batch of prisms, since the gold thickness and refractive indices do not vary greatly in one batch. Furthermore, the layer system has to be known or plausibly estimated to be able to apply the Fresnel equation formalism to estimate the surface state. Deviations from the modelled layer system can lead to wrong estimations of change in refractive index. Ideally, the measurement is compared to a reference structure so as to avoid any misinterpretations.

References

[1] S. Löfås, A. Mcwhirter in *Surface Plasmon Resonance Based Sensors*, *Vol. 4*, (Ed.: J. Homola), Springer Berlin Heidelberg, Berlin, Heidelberg, **2006**, pp. 117–151, DOI 10.1007/5346_017 (cit. on p. 82).

[2] I. I. Gorshkova, J. Svitel, F. Razjouyan, P. Schuck, "Bayesian Analysis of Heterogeneity in the Distribution of Binding Properties of Immobilized Surface Sites", *Langmuir* **2008**, *24*, 11577–11586, DOI 10.1021/la801186w (cit. on p. 82).

[3] B. Yakes, J. Buijs, C. Elliott, K. Campbell, "Surface Plasmon Resonance Biosensing: Approaches for Screening and Characterising Antibodies for Food Diagnostics", *Talanta* **2016**, *156–157*, 55–63, DOI 10.1016/j.talanta.2016.05.008 (cit. on p. 82).

[4] C. S. Schneider, A. G. Bhargav, J. G. Perez, A. S. Wadajkar, J. A. Winkles, G. F. Woodworth, A. J. Kim, "Surface Plasmon Resonance as a High Throughput Method to Evaluate Specific and Non-Specific Binding of Nanotherapeutics", *Journal of Controlled Release* **2015**, *219*, 331–344, DOI 10.1016/j.jconrel.2015.09.048 (cit. on p. 82).

[5] W. Zhou, M. Yang, S. Li, J. Zhu, "Surface Plasmon Resonance Imaging Validation of Small Molecule Drugs Binding on Target Protein Microarrays", *Applied Surface Science* **2018**, *450*, 328–335, DOI 10.1016/j.apsusc.2018.04.072 (cit. on p. 82).

[6] L. Simon, R. E. Gyurcsányi, "Multiplexed Assessment of the Surface Density of DNA Probes on DNA Microarrays by Surface Plasmon Resonance Imaging", *Analytica Chimica Acta* **2019**, *1047*, 131–138, DOI 10.1016/j.aca.2018.09.048 (cit. on p. 82).

[7] P. Schuck, A. P. Minton, "Analysis of Mass Transport-Limited Binding Kinetics in Evanescent Wave Biosensors", *Analytical Biochemistry* **1996**, *240*, 262–272, DOI 10.1006/abio.1996.0356 (cit. on p. 82).

[8] J. W. Suk, A. Kitt, C. W. Magnuson, Y. Hao, S. Ahmed, J. An, A. K. Swan, B. B. Goldberg, R. S. Ruoff, "Transfer of CVD-Grown Monolayer Graphene onto Arbitrary Substrates", *ACS Nano* **2011**, *5*, 6916–6924, DOI 10.1021/nn201207c (cit. on p. 83).

[9] A. Kirillov et al., Segment Anything, **2023**, DOI 10.48550/arXiv.2304.02643 (cit. on p. 84).

[10] N. Morin-Crini et al., "Worldwide Cases of Water Pollution by Emerging Contaminants: A Review", *Environmental Chemistry Letters* **2022**, *20*, 2311–2338, DOI 10.1007/s10311-022-01447-4 (cit. on p. 86).

[11] M. Ruff, M. S. Mueller, M. Loos, H. P. Singer, "Quantitative Target and Systematic Non-Target Analysis of Polar Organic Micro-Pollutants along the River Rhine Using High-Resolution Mass-Spectrometry – Identification of Unknown Sources and Compounds", *Water Research* **2015**, *87*, 145–154, DOI 10.1016/j.watres.2015.09.017 (cit. on p. 86).

[12] N. Kamjunke et al., "Lagrangian Profiles of Riverine Autotrophy, Organic Matter Transformation, and Micropollutants at Extreme Drought", *Science of The Total Environment* **2022**, *828*, 154243, DOI 10.1016/j.scitotenv.2022.154243 (cit. on p. 86).

[13] Z. Hrkal, Y. Adomat, D. Rozman, T. Grischek, "Efficiency of Micropollutant Removal through Artificial Recharge and Riverbank Filtration: Case Studies of Káraný, Czech Republic and Dresden-Hosterwitz, Germany", *Environmental Earth Sciences* **2023**, *82*, 155, DOI 10.1007/s12665-023-10785-7 (cit. on p. 86).

[14] M. H. Do, B. Dubreuil, J. Peydecastaing, G. Vaca-Medina, T.-T. Nhu-Trang, N. Jaffrezic-Renault, P. Behra, "Chitosan-Based Nanocomposites for Glyphosate Detection Using Surface Plasmon Resonance Sensor", *Sensors* **2020**, *20*, 5942, DOI 10.3390/s20205942 (cit. on p. 86).

[15] J. J. Kelly, D. P. Myers, "Transformer Life Extension Through Proper Reinhibiting and Preservation of the Oil Insulation", *IEEE Transactions on Industry Applications* **1995**, *31*, 55–60, DOI 10.1109/28.363050 (cit. on p. 86).

[16] R. Kurz, J. Leedy in Proceedings: Electrical Insulation Conference and Electrical Manufacturing and Coil Winding Conference, IEEE, Rosemont, IL, USA, **1995**, pp. 529–536, DOI 10.1109/EEIC.1997.651235 (cit. on p. 86).

[17] Y. S. Leong, P. J. Ker, M. H. Hasnul, M. A. Khamis, M. A. Hannan, M. Z. Jamaludin, H. M. Looe, "Portable NIR Spectroscopy Measuring Device for Transformer Oil DBPC Inhibitor Analysis", *IEEE Transactions on Industry Applications* **2021**, *57*, 2114–2119, DOI 10.1109/TIA.2021.3057357 (cit. on p. 86).

[18] N. I. H. Zulkefli, M. S. A. Khiar, S. A. Ghani in 2023 19th IEEE International Colloquium on Signal Processing & Its Applications (CSPA), IEEE, Kedah, Malaysia, **2023**, pp. 140–143, DOI 10.1109/CSPA57446.2023.10087719 (cit. on p. 86).

[19] Y. Li et al., "Equilibrium, Kinetic and Thermodynamic Studies on the Adsorption of Phenol onto Graphene", *Materials Research Bulletin* **2012**, *47*, 1898–1904, DOI 10.1016/j.materresbull.2012.04.021 (cit. on p. 86).

[20] H. N. Catherine, M.-H. Ou, B. Manu, Y.-h. Shih, "Adsorption Mechanism of Emerging and Conventional Phenolic Compounds on Graphene Oxide Nanoflakes in Water", *Science of The Total Environment* **2018**, *635*, 629–638, DOI 10.1016/j.scitotenv.2018.03.389 (cit. on p. 86).

[21] J. Chen, Z. Li, J. Ge, R. Yang, L. Zhang, L.-b. Qu, H.-q. Wang, L. Zhang, "An Aptamer-Based Signal-on Bio-Assay for Sensitive and Selective Detection of Kanamycin A by Using Gold Nanoparticles", *Talanta* **2015**, *139*, 226–232, DOI 10.1016/j.talanta.2015.02.036 (cit. on pp. 89, 91).

[22] Á. Écija-Arenas, E.-M. Kirchner, T. Hirsch, J. M. Fernández-Romero, "Development of an Aptamer-Based SPR-biosensor for the Determination of Kanamycin Residues in Foods", *Analytica Chimica Acta* **2021**, *1169*, 338631, DOI 10.1016/j.aca.2021.338631 (cit. on pp. 89, 91).

[23] J. Albright, S. Tuckey, G. Woods, "Antibiotics in Milk—A Review", *Journal of Dairy Science* **1961**, *44*, 779–807, DOI 10.3168/jds.S0022-0302(61)89819-6 (cit. on p. 90).

[24] S. Sachi, J. Ferdous, M. Sikder, S. Hussani, "Antibiotic Residues in Milk: Past, Present, and Future", *Journal of Advanced Veterinary and Animal Research* **2019**, *6*, 315, DOI 10.5455/javar.2019.f350 (cit. on p. 90).

[25] B. V. Ribeiro, L. F. Ferreira, D. L. Franco, "Advances in Biosensor Development for the Determination of Antibiotics in Cow's Milk - A Review", *Talanta Open* **2022**, *6*, 100145, DOI 10.1016/j.talo.2022.100145 (cit. on p. 90).

[26] S. Seth, P. Rathinasabapathi, "A Short Review on Detection of Antibiotics in Milk Using Nanomaterial-Based Biosensor", *Food Analytical Methods* **2022**, *15*, 2181–2192, DOI 10.1007/s12161-022-02291-6 (cit. on p. 90).

[27] S. Song, L. Wang, J. Li, C. Fan, J. Zhao, "Aptamer-Based Biosensors", *TrAC Trends in Analytical Chemistry* **2008**, *27*, 108–117, DOI 10.1016/j.trac.2007.12.004 (cit. on p. 90).

[28] R. Y. Robati, A. Arab, M. Ramezani, F. A. Langroodi, K. Abnous, S. M. Taghdisi, "Aptasensors for Quantitative Detection of Kanamycin", *Biosensors and Bioelectronics* **2016**, *82*, 162–172, DOI 10.1016/j.bios.2016.04.011 (cit. on p. 90).

[29] K.-M. Song, M. Cho, H. Jo, K. Min, S. H. Jeon, T. Kim, M. S. Han, J. K. Ku, C. Ban, "Gold Nanoparticle-Based Colorimetric Detection of Kanamycin Using a DNA Aptamer", *Analytical Biochemistry* **2011**, *415*, 175–181, DOI 10.1016/j.ab.2011.04.007 (cit. on p. 91).

[30] A. Sharma, G. Istamboulie, A. Hayat, G. Catanante, S. Bhand, J. L. Marty, "Disposable and Portable Aptamer Functionalized Impedimetric Sensor for Detection of Kanamycin Residue in Milk Sample", *Sensors and Actuators B: Chemical* **2017**, *245*, 507–515, DOI 10.1016/j.snb.2017.02.002 (cit. on p. 91).

[31] J. Svirelis, J. Andersson, A. Stradner, A. Dahlin, "Accurate Correction of the "Bulk Response" in Surface Plasmon Resonance Sensing Provides New Insights on Interactions Involving Lysozyme and Poly(Ethylene Glycol)", *ACS Sensors* **2022**, *7*, 1175–1182, DOI 10.1021/acssensors.2c00273 (cit. on p. 91).

[32] A. Agrawal, A. Ali, S. Boyd, Minimum-Distortion Embedding, **2021**, DOI 10.48550/ARXIV.2103.02559 (cit. on p. 92).

[33] M. A. Momin, S. Sinha, I. G. Tucker, C. Doyle, S. C. Das, "Dry Powder Formulation of Kanamycin with Enhanced Aerosolization Efficiency for Drug-Resistant Tuberculosis", *International Journal of Pharmaceutics* **2017**, *528*, 107–117, DOI 10.1016/j.ijpharm.2017.06.004 (cit. on p. 94).

[34] *Handbook of Data on Organic Compounds*, 2. ed, (Eds.: R. C. Weast, Chemical Rubber Company), CRC Pr, Boca Raton, Fla, **1989** (cit. on p. 94).

[35] P. Harder, M. Grunze, R. Dahint, G. M. Whitesides, P. E. Laibinis, "Molecular Conformation in Oligo(Ethylene Glycol)-Terminated Self-Assembled Monolayers on Gold and Silver Surfaces Determines Their Ability To Resist Protein Adsorption", *The Journal of Physical Chemistry B* **1998**, *102*, 426–436, DOI 10.1021/jp972635z (cit. on p. 94).

[36] L. Simon, Z. Bognár, R. E. Gyurcsányi, "Finding the Optimal Surface Density of Aptamer Monolayers by SPR Imaging Detection-based Aptamer Microarrays", *Electroanalysis* **2020**, *32*, 851–858, DOI 10.1002/elan.201900736 (cit. on p. 95).

[37] M. Pons, M. Perenon, H. Bonnet, E. Gillon, C. Vallée, L. Coche-Guérente, E. Defrancq, N. Spinelli, A. Van Der Heyden, J. Dejeu, "Conformational Transition in SPR Experiments: Impact of Spacer Length, Immobilization Mode and Aptamer Density on Signal Sign and Amplitude", *The Analyst* **2022**, *147*, 4197–4205, DOI 10.1039/D2AN00824F (cit. on p. 96).

[38] D. J. Bornhop, M. N. Kammer, A. Kussrow, R. A. Flowers, J. Meiler, "Origin and Prediction of Free-Solution Interaction Studies Performed Label-Free", *Proceedings of the National Academy of Sciences* **2016**, *113*, DOI 10.1073/pnas.1515706113 (cit. on p. 96).

[39] J. Dejeu, H. Bonnet, N. Spinelli, E. Defrancq, L. Coche-Guérente, A. Van Der Heyden, P. Labbé, "Impact of Conformational Transitions on SPR Signals—Theoretical Treatment and Application in Small Analytes/Aptamer Recognition", *The Journal of Physical Chemistry C* **2018**, *122*, 21521–21530, DOI 10.1021/acs.jpcc.8b07298 (cit. on p. 96).

Chapter 6

Conclusion and Outlook

This work provides insight into the potential of camera-based surface plasmon resonance sensors when utilising the spatial sensor by modulating the sensor response through lateral modification of surface parameters or input illumination. These modifications have to be coupled with adequate signal processing. Modelling the sensor response using Fresnel formulae allows for accurate representation of the sensor surface state, increasing confidence in measured values. Alternatively, data-based modelling approaches can be utilised which eliminate the need for approximation of a physical model to observed data but are limited by the data they are trained on. It has been explored how, especially, deep learning models that are specialised in image processing (CNNs) can be utilised for qualitative or quantitative assessment of analytes with the help of a receptor array on an SPR surface. Notably, this approach demonstrates strong generalization capabilities, performing effectively on unseen sensors used for the same task. Preliminary experiments indicate that performance enhancements are feasible when data from different points in time during binding or debinding are used during processing.

However, there are several caveats to the presented methodology. The lateral change in input angle results in a image that is more difficult to evaluate since simply averaging over large areas is not useful when the sensitivity varies drastically. This also means that the noise decrease through spatial averaging is locked behind effectively using the lateral information available which makes the presented methodology vital for angle-modulated SPRi. Data-driven models are, in principle, able to use that information but have to be constrained during training to use this lateral shift by appropriate data which requires a significant amount of measurements. Most importantly, the data-driven methods require the training data to contain possible expected variations associated with the analytical task as they are usually unable to extrapolate. Consequently, trained detectors cannot be used for new analytes or in a new matrix without retraining the model which requires additional labelled data. Data labelling is another challenging restriction, since in order to label a certain sensor state, the analyte concentration and matrix state has to be known as precisely as possible which is often not available in transitional periods. So far, this has been

circumvented by using only steady-state data, effectively reducing the amount of captured data by a large margin.

In future, several improvements are conceivable. One very promising approach is the application of a physical loss term during training of the neural network. This can be done by calculating the expected response for a set of parameters with the help of the Fresnel equations and adding the result to a combined loss term (conveniently, differentiable transfer-matrix formalism is available for use in neural networks*). This approach has the benefit of integrating physical information into the neural network. Consequently, the network can be trained to predict parameters such as the refractive index and thickness of functionalisation layers, enabling the detection of captured analytes while retaining the flexibility of high-dimensional neural networks. Unfortunately, this approach relies on precise knowledge of the sensor state beforehand for training. As with any deep learning model, performance hinges on high-quality training data. The incorporation of a physical loss function can mitigate this reliance on extensive datasets, provided the physical model within the loss function accurately reflects real-world sensor behaviour.
Another improvement is the more fine-grained segmentation of the image data. Due to the large surface area of the sensor, large variation of surface state is to be expected. This effectively reduces the redundant information and leads to diverse sensor responses collected over the surface. Currently, most of this information is discarded through spatial averaging of intensities, large receptive fields of the convolutional neural network and pooling of surface area in physical modelling. It would be more appropriate to consider the surface laterally continuously changing or at least increase the amount of different areas considerably. Modern segmentation models can be used in semi-supervised manner, where setting markers for different functional areas is sufficient to effectively partition the surface which enables the researcher using the instrument to set the different functional areas. Fully automatic detection of these areas is also possible when utilising e.g., an angle scan and an appropriate segmentation model capable of processing image sequences†.
Apart from these methods that can be applied to the presented sensor setup, more information can be collected during acquisition by employing polarisation- or wavelength-sensitive detectors. These cameras are equipped with several filters similar to colour-sensitive detectors but with higher wavelength resolution or alternatively polarisation filters with different orientations placed in front of pixels and combining those pixels to a multi-polarisation or -spectral image. This information increase can be utilised similarly: via physical modelling through the Fresnel formalism, or with the help of machine learning under known conditions and with a defined purpose. Polarisation information can be used to continuously reference intensity and temperature variations. Wavelength data is frequently used as an alternative to angular modulation and additionally enables the use of LSPR-based sensors.

In conclusion, deep learning-assisted spatial SPR sensors hold immense potential for diverse applications, including online quality control, anomaly detection, and bio-

*`https://github.com/MLResearchAtOSRAM/tmm_fast`
†`https://github.com/facebookresearch/sam2`

fouling quantification. However, realizing this potential hinges on carefully designed experiments that yield high-quality data. Furthermore, incorporating orthogonal data sources is crucial for more precise determination of the surface state during calibration. Suitable surface-sensitive techniques include Raman spectroscopy, ellipsometry, and impedance spectroscopy. Coupling these methods can improve knowledge on the observed state during training. This information together with the presented methods can simplify sensor development and improve performance.

Chapter 7

Zusammenfassung in deutscher Sprache

Diese Arbeit gibt einen Einblick in das Potenzial kamerabasierter Oberflächenplasmonenresonanzsensoren, wenn der räumliche Sensor durch die Modulation von Sensorreaktionen durch laterale Modifikation der Oberflächenparameter oder der Eingangsbeleuchtung genutzt wird. Diese Modifikationen erzeugen eine komplexe Sensorantwort und müssen daher mit einer geeigneten Signalverarbeitung gekoppelt werden. Die Modellierung der Sensorantwort mit Hilfe von Fresnel-Formeln ermöglicht eine genaue Bestimmung des Sensoroberflächenzustands und erhöht so die Konfidenz in gemessene Werte. Alternativ können datenbasierte Modellierungsansätze angewandt werden, die eine Annäherung eines physikalischen Modells an aufgenommene Daten ersetzen können, aber durch die Daten, auf denen sie trainiert werden, begrenzt sind.

Es wurde untersucht, wie insbesondere tiefe neuronale Netze, die auf die Bildverarbeitung spezialisiert sind (CNNs), für die qualitative oder quantitative Bewertung von Analyten mit Hilfe eines Rezeptor-Arrays auf einer SPR-Oberfläche eingesetzt werden können. Insbesondere zeigt dieser Ansatz starke Generalisierungsfähigkeiten, die auch bei unbekannten (unkalibrierten) Sensoren, die für dieselbe Aufgabe verwendet werden, wirksam sind. Vorläufige Experimente deuten darauf hin, dass Genauigkeitssteigerungen möglich sind, wenn bei der Verarbeitung Daten von verschiedenen Zeitpunkten während der Bindung verwendet werden.

Zusammenfassend lässt sich sagen, dass räumliche SPR-Sensoren mit Hilfe von tiefen neuronalen Netzen immenses Potenzial für verschiedene Anwendungen haben, darunter Online-Qualitätskontrolle, Erkennung von Anomalien und Quantifizierung von Biofouling. Die Realisierung dieses Potenzials hängt jedoch von sorgfältig geplanten Experimenten ab, die qualitativ hochwertige Daten liefern. Darüber hinaus ist die Einbeziehung orthogonaler Datenquellen entscheidend für eine genauere Bestimmung des Oberflächenzustands während der Kalibrierung. Zu geeigneten oberflächensensitiven Techniken gehören Raman-Spektroskopie, Ellipsometrie und

Impedanzspektroskopie. Die Kopplung dieser Methoden kann das Wissen über den beobachteten Zustand während des Trainings verbessern. Diese Informationen können zusammen mit den vorgestellten Methoden die Sensorentwicklung vereinfachen und die Leistung des Sensors in der Anwedung verbessern.

Appendices

A Miscellaneous

A.1 Surface Plasmon Dispersion Relation

The reflectance for p-polarised light at an interface between medium 1 and medium 2 (Fresnel's tangent law) is [1, p. 40]:

$$R = \left| \frac{\tan(\theta_1 - \theta_2)}{\tan(\theta_1 + \theta_2)} \right|^2 . \tag{A.1}$$

We can distinguish between two extreme cases: [2]

1. $\theta_1 + \theta_2 = \pi/2$: the denominator approaches infinity, the reflected light vanishes (Brewster angle)
2. $\theta_1 - \theta_2 = \pi/2$: the nominator approaches infinity, the reflected light approaches infinity, implying resonance

The second case implies:

$$\cos\theta_1 = -\sin\theta_2$$

With Snell's law:

$$\tan\theta_1 = \frac{\sin\theta_1}{-\sin\theta_2} = -\frac{n_2}{n_1}$$

And trigonometric relations (see Figure 2.2):

$$\tan\theta_1 = \frac{k_{x1}}{k_{z1}}$$

$$\left|\vec{k}\right|^2 = k_x^2 + k_z^2 = \frac{\omega^2}{c^2}\epsilon$$

Rearrangement yields:

$$k_x^2 = \left|\vec{k}\right|^2 - k_x^2\frac{\epsilon_1}{\epsilon_2}$$

$$k_x = \frac{\omega}{c}\sqrt{\frac{\epsilon_1\epsilon_2}{\epsilon_1 + \epsilon_2}} \tag{A.2}$$

$$k_{zi} = \frac{\omega}{c}\sqrt{\frac{\epsilon_i^2}{\epsilon_1 + \epsilon_2}} \tag{A.3}$$

From Equation A.2 and Equation A.3 we can see that when ϵ_2 becomes smaller than $-\epsilon_1$, k_z is purely imaginary while k_x is real (the relative permittivity of metals is in general complex with a large negative real part). That means the electromagnetic wave is travelling parallel to x and exponentially decays in z-direction.

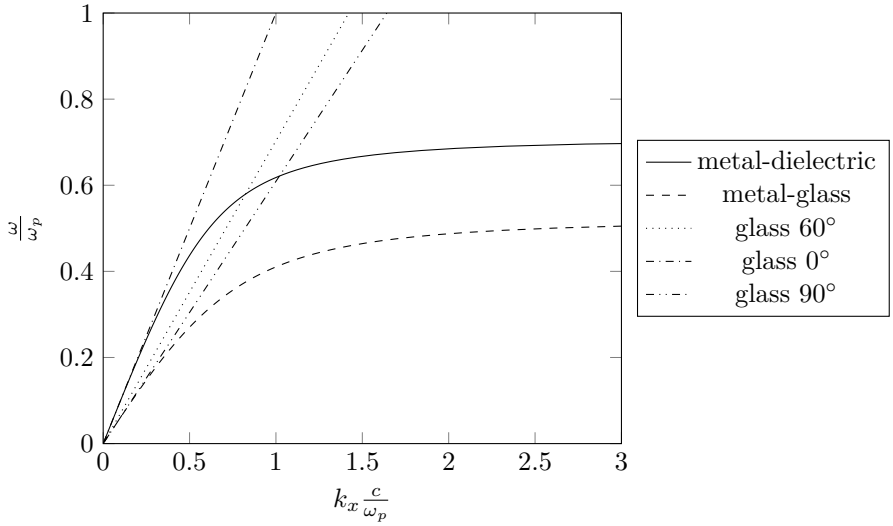

Fig. A1. Dispersion relations for a three-phase setup, where metal-dielectric (solid line) is the dispersion relation for surface plasmons excited on the interface between metal and dielectric and the lines relate to the dispersion relation of light propagating through glass at different angles towards the surface. Light passing through glass can excite surface plasmons by selecting appropriate angles (e.g. 60° here) so that the wave vector of the incident light and the surface plasmons match, i.e. they intersect.

Note that, in general, the permittivity of the metal is a complex quantity and there is a significant imaginary part towards the surface plasmon frequency ω_{sp} given by:

$$\omega_{sp} = \frac{\omega_p}{\sqrt{1+\epsilon_1}}$$

where ω_p is the bulk plasma frequency which can be calculated with the Drude model [3]:

$$\epsilon(\omega) = 1 - \frac{n_e e^2}{\epsilon_0 m^* \omega^2} = 1 - \frac{\omega_p^2}{\omega^2} \tag{A.4}$$

With electron density n_e, elementary charge e, and m^* electron mass.

Substituting Equation A.4 into Equation A.2, we get the dispersion relation for surface plasmons (see Figure A1).

A.2 Temperature and wavelength dependant Sellmeier equation

The wavelength dependant Sellmeier equation is:

$$n_0(\lambda) = \sqrt{1 + \frac{B_1\lambda^2}{\lambda^2 - C_1} + \frac{B_2\lambda^2}{\lambda^2 - C_2} + \frac{B_3\lambda^2}{\lambda^2 - C_3}} \tag{A.5}$$

with the wavelength λ and the Sellmeier coefficients B and C. The temperature coefficient of the refractive index is:

$$\Delta n(\lambda, T) = \frac{n_0^2(\lambda) - 1}{2n_0(\lambda)} \left(D_0 \Delta T + D_1 \Delta T^2 + D_3 \Delta T^3 + \frac{E_0 \Delta T + E_1 \Delta T^2}{\lambda^2 - \lambda_{TK}^2} \right) \quad \text{(A.6)}$$

with ΔT the temperature difference to reference temperature 20 °C, the wavelength coefficient λ_{TK} and the temperature coefficients D and E.

B Supporting Information

B.1 SI: Characterising Surface Plasmon Resonance Imaging for Biosensing

B.1.1 Experimental

All measurements were performed using a setup as described in section B.2 unless stated otherwise.

Noise Measurements. Data for allan deviation was obtained by collecting image data from an SPR setup with a 730 nm LED (LZ1-00R302, Osram, Germany), a suitable wavelength filter (centre wavelength 730 nm with a 10 nm full width at half maximum, Thorlabs, UK) and a motorised polariser illuminating a SF2 prism with s-polarised light. The image was collected with a IMX178 sensor and a objective lens with a distance ring increasing the back focal length and thus magnification of the image. Noise was determined with the help of the overlapping allan deviation [4].

Objective Lens. The f# of the objective lens was adjusted as well as a 2x focal length extender was introduced between camera and objective lens while imaging the surface of a prism where small rectangular mirrors were deposited. These mirrors were created by vapor deposition of an additional 200 nm of gold onto the plasmonic surface so the plasmons are quenched. The surface was illuminated with p-polarised light at a dielectric of air against the sensor surface (resulting in weak contrast between mirrors and gold surface). Sharpness was measured with the help of acutance defined by the brightness change over pixel change of the mirrors where relative acutance measures the ratio of the gradients of the mirrors towards the edge of the prism to the maximum gradients. The contrast is calculated by taking the mean intensities of the mirror surface area and the regular surface and computing the contrast like so:

$$\frac{I_{max} - I_{min}}{I_{max} + I_{min}}$$

Receptor Thickness. Receptors were deposited using a dispenser (Musashi Shot-Mini 200 Sx, Musashi, Japan). This device operates by pushing the dispensing medium through a needle with the help of air pressure. As such, there are several parameters influencing the droplet formed during dispensing: dispensing pressure, dispensing time, needle diameter, and medium viscosity. Additionally, the droplet may be deposited onto the surface when the needle is in close proximity to the substrate or get expelled from the needle when the distance is large. First, dispensing characteristics were determined: the dispensed volume per shot was calculated by repeatedly applying 20 kPa for 0.05 s until a droplet is expelled from a needle with 0.06 mm inner diameter. The droplet volume was determined with a microscope objective attached to a high-speed camera (VH-Z20R and VW-6000, Keyence, Japan). The dispensed volume per shot can then be calculated by dividing the droplet volume

by the amount of shots needed to form a droplet. The resulting volume was calculated to 0.12 mm^3. The 2D materials Graphene oxide (GO), reduced graphene oxide (rGO), boron nitride (BN), and MoS_2MoO_3 were evaluated. These materials were provided by Patrick Recum who synthesised the graphene based materials while the others were purchased. Various solvents (1-Methyl-2-pyrrolidon, water and 2-propanol) and the material concentrations resulted in quite diverse viscosity liquids. The graphene solutions were gradually diluted to a concentration of approximately 0.02 $g\,L^{-1}$. The dispensed material was then imaged with the SPR setup and the angle was varied in 1° steps while the intensity was recorded as an average over the dispensed areas.

Oil Classification. Plant oils were mixed to create different refractive index solutions with a diverse set of components. Almond oil was used as a base and cinnamon oil was added until the refractive index measured with a refractometer (DR6000, Krüss, Germany) fell into one of three values: 1.4735, 1.4740, and 1.4745. Cedar oil was also used to create a mixture with almond oil to a refractive index of 1.4740. The different oils were analysed with two different prisms, where on one of them 2D materials were dispensed as is, while on the other diluted material solutions were used. Each receptor was spotted 10 times on the sensor surface. The different oils were pumped over the functionalised surfaces for 25 minutes each at least three times commutating the order in which the oils were presented to the sensor. Steady state data of the last two minutes before changing analyte was used for further processing. Every data point consists of six regions of interest for every receptor type, where the measured intensity was averaged over the pre-defined regions. Since there were four different receptor types used (rGO, MoS_2/MoO_3, GO, BN), a 24-dimensional vector was acquired for every time step. The first two repeats of the analyte solutions were used to train a random forest classifier, while the last one was used to test the accuracy of the classifier.

B.1.2 Noise and Detector Configuration

The overlapping allan deviation was acquired for the detector without illumination by using averages over a set of pixels (see Figure B1 a). The deviation roughly follows a $1/\sqrt{\tau}$ relationship which means that it is dominated by Gaussian noise and longer integration generally decreases noise until thermal fluctuations change this dynamic. With added illumination this picture changes (Figure B1 b), the light source in use is also subject to flicker noise ($\propto \tau$), which decreases the benefit of longer integration times. Spatial averaging decreases noise approximately as expected with the number of pixels that are averaged N ($\propto \sqrt{N}$) with diminishing returns for very large regions.

Field of view, lateral resolution and depth of field cannot be maximised collectively as a sensor geared towards lateral resolution will have a limited depth of field. The optical system used throughout this work was configured so that field of view and depth of field were optimised under constraints of space and readily available lenses. Depth of field was characterised with the help of acutance and contrast of the image edges relative to the middle, which was put in focus. Acutance was calculated via

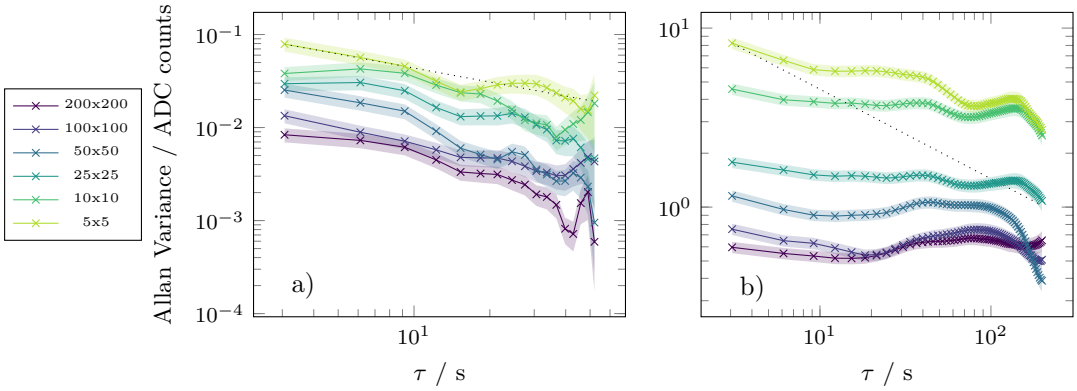

Fig. B1. Overlapping allan deviation calculated for the camera sensor without illumination (a) and with illumination (b) for different rectangular sizes of image subsets.

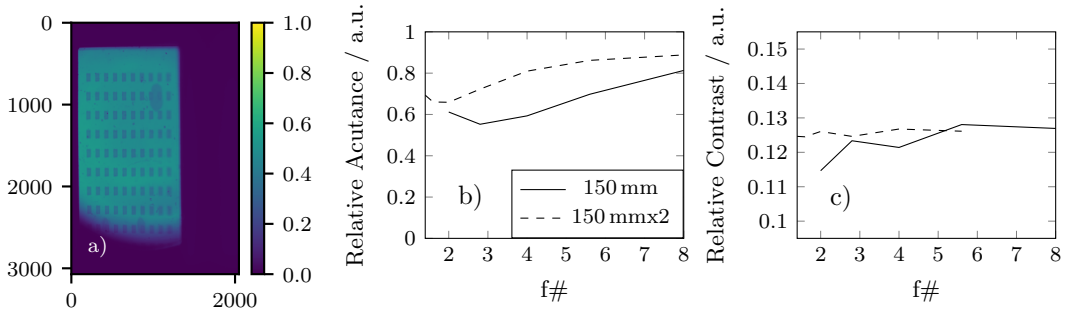

Fig. B2. The optical setup was tailored towards large field of view so that the entire sensor can be imaged (a). With a decrease of aperture (which relates to larger f#) the edges of the image become more focussed as the DOF increases (b). This affects image resolution while contrast is unaffected (c). Acutance and contrast were calculated for an objective lens with 150 mm and the same objective lens with a 2x focal length extender. 50 mm and 100 mm lenses performed worse (not shown).

the image gradient and contrast was determined with structure intensity minima and maxima where the structure was generated with the help of mirrors on a regular sensor surface. Acutance can be understood as a measure of image sharpness, which should be as homogeneous as possible for the entire surface which can be quantified with a relative metric like in Figure B2 b. Since the contrast is unaffected by the different aperture sizes and the focal length extender, the optimum f# of 5.6 together with a focal length extender was chosen for most measurements to achieve a large field of view and a high depth of field.

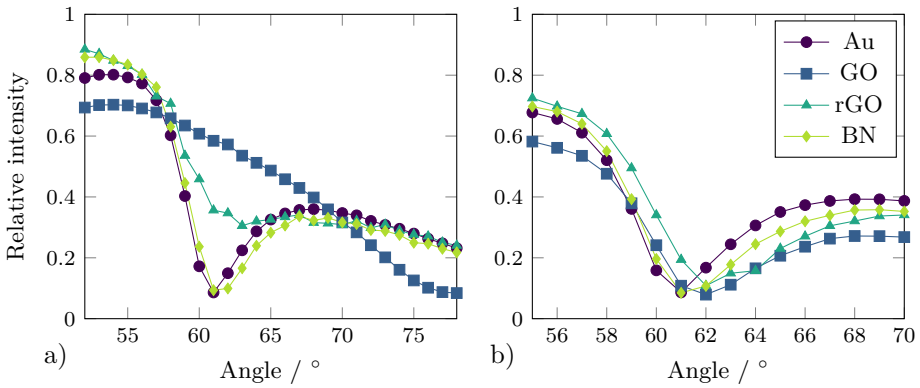

Fig. B3. 2D materials have been dispensed on top of a SPR sensor surface. The solvent, concentration and the dispensing parameters have an effect on the size of the dispensed spots and their thickness. The heterogeneous materials can be very different from the gold surface in terms of SPR response (a). Iteratively, the 2D material concentration was optimised to achieve very thin layers on top of gold which results in a small shift of the SPR curve (b) so that sensitivity is maximised at a similar angle.

B.1.3 Receptor selection

Different 2D materials were evaluated using a dispenser to spot the materials onto a gold-coated glass prism. Solvent and receptor concentration as well as the dispenser parameters (dispensing pressure and time, needle diameter) had to be optimised for all the different materials. Graphene oxide, reduced graphene oxide, boron nitride, and MoS_2/MoO_3 were evaluated. Due to the different solvents (NMP, H_2O/IPO) dispensing proved to be difficult to control and some materials produced very inhomogeneous layers (especially MoS_2/MoO_3).
The materials were diluted to form very thin layers on top of gold and match the SPR curve as close as possible to the gold surface Figure B3. The diluted rGO and GO (to approximately $0.02\,\mathrm{g\,L^{-1}}$) were theoretically sufficient in quantity to produce more than a single layer over the entire dispensed spot even when accounting for loss due to the rather strong coffee ring. The different materials were used in a test setup where two different oils (cinnamon and cedar) were mixed with almond oil to the same refractive index (as determined with a refractometer). The intensity on top of the receptors was recorded and a random forest classifier was used to classify the oils. Through optimisation of the dispensing process and dilution of the receptor solutions a 50 % improvement in classification accuracy (to approximately 90 %) was achieved in an independent test set. Feature importance of the GO-derivatives, their tuneability in oxidisation state, and good matching to the SPR curve of the gold surface led to the employment of GO and rGO as most viable 2D receptors (Figure B4).

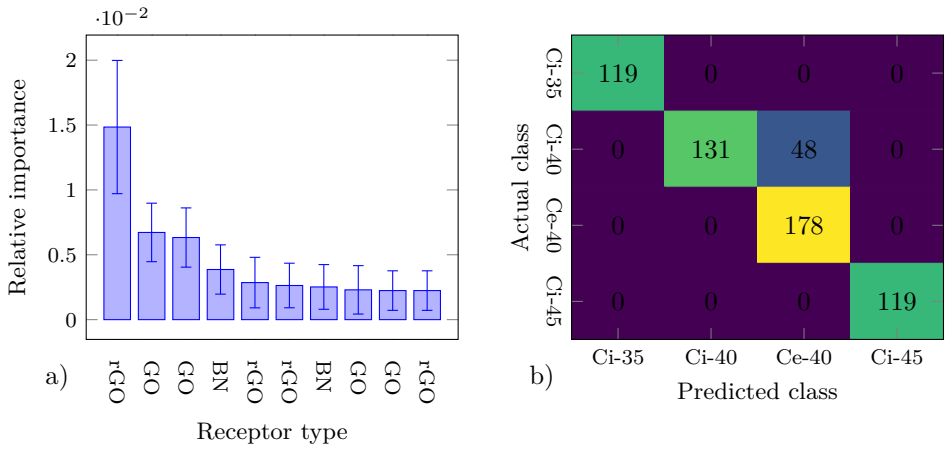

Fig. B4. Classification of food oil composition with an array of different 2D materials (GO and rGO, boron nitride - BN, molybdenum disulfide - MoS_2). (Permutation) feature importance of the ten most important receptor spots indicated in (a) and test classification confusion matrix in (b). The classes "Ci" and "Ce" refer to cinnamon and cedar additive to almond oil, respectively. The numbers indicate the last digits of the refractive index that was measured with a refractometer.

This does not necessarily mean that the 2D materials have any affinity to the plant oil components but the sensitivity may have been increased due to the optimised layer thickness of the 2D materials.

B.2 SI: Semi-Selective Array for the Classification of Purines with Surface Plasmon Resonance Imaging and Deep Learning Analysis

Data was gathered with an adjustable SPR setup built in-house as described in detail elsewhere [5]. Briefly, a red LED (WL-SMDC 660 nm, Würth Elektronik, Germany) with a collimator lens (50 mm focal length, Edmund Optics, UK), wavelength filter (660 nm with 10 nm full width half maximum (FWHM), Edmund Optics) and polarizer (Edmund Optics) were used for illumination. The LED current was supplied by a 2636B Source Meter (Keithley, Germany). A FLIR BFS-U3-63S4 camera (FLIR, Germany) with a fixed focal length camera lens (Edmund Optics) and a 2x lens extender (Computar EX2C, Computar, USA) were used. A 3D-printed aluminum flow cell with a silicone sealing was fixed to the prism surface. A peltier was attached to the flow cell to control the medium and flow cell temperature. A peristaltic pump (Cole-Parmer GmbH, Germany) was used to pump the analyte-solutions over the sensor surface. The LED current was set to 10 mA, temperature of the flow cell was set to 21 °C, the objective's aperture was 5.6/f, and the exposure time 10 ms.

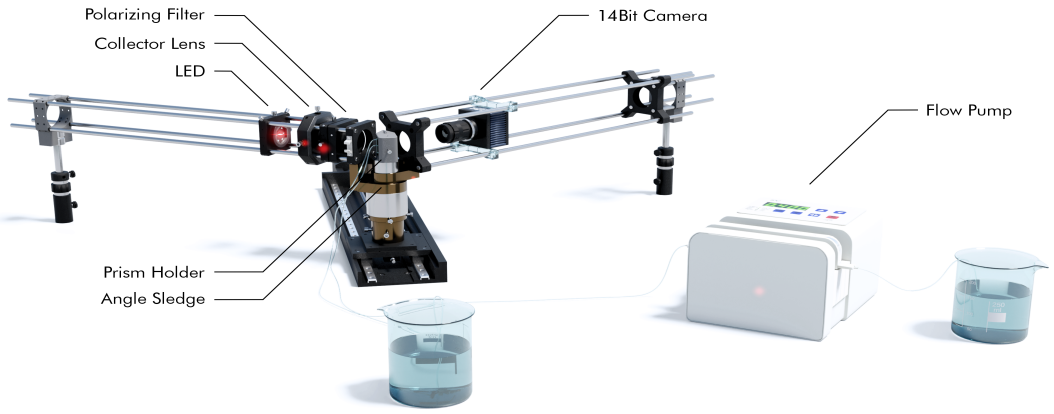

Fig. B5. Components and arrangement of the custom-built measurement setup for SPR imaging.

Brightness variations and masking were deliberately introduced in augmentation to reduce the effects of interferences often present in online monitoring i.e., fluctuations of the light source or emerging air bubbles. Similarly, temperature variations can be introduced during training to eliminate their impact on classification. As an alternative, reference structures may be introduced onto the sensor surface to calibrate for temperature drifts.

Hardware and software packages:

GPU device: NVIDIA GP102 (TITAN Xp) driver: nvidia v: 470.161.03

Cuda compilation tools, release 11.3

DL pipeline packages: Python 3.8.10, Pytorch 2.0.0, Pytorch-lightning 2.0.1, Kornia 0.6.11, Captum 0.6.0, Torchmetrics 0.11.4, Optuna 3.1.1

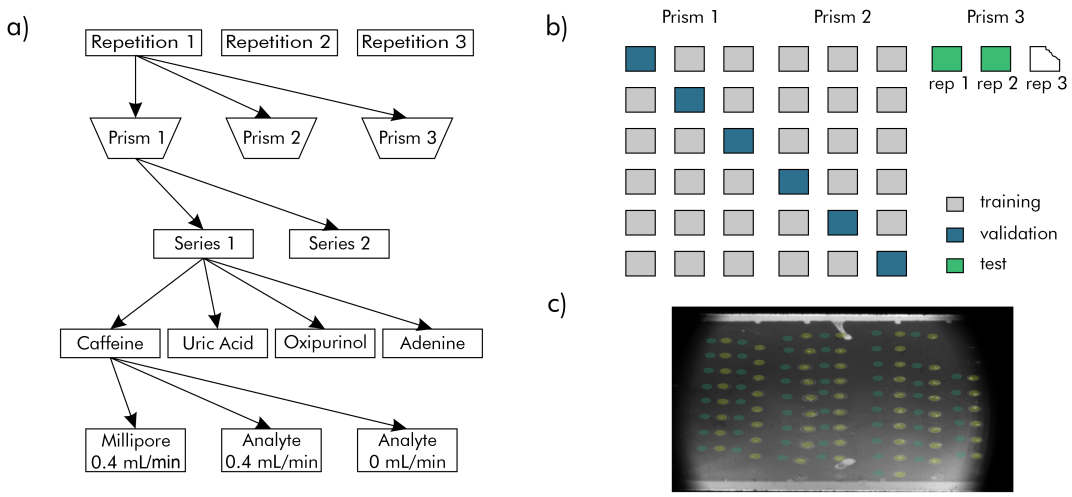

Fig. B6. a) Measurement and repetitions – each analyte is presented to the sensor after a washing step. The measurement cycle is repeated for all analytes, twice for every prism. Each prism was measured three times; b) Measurements for the third prism on the last repetition were not possible due to a fracture. Prism 3 was used for test data. Measurements from prisms one and two were used as training and validation data with cross-validation as shown; c) Regions of interest on sensor image - yellow ellipses lie on receptor spots, green ellipses on the gold surface close to receptor spots. ROIs are smaller than the receptors but uniform in size. Here rGO content increases from left to right.

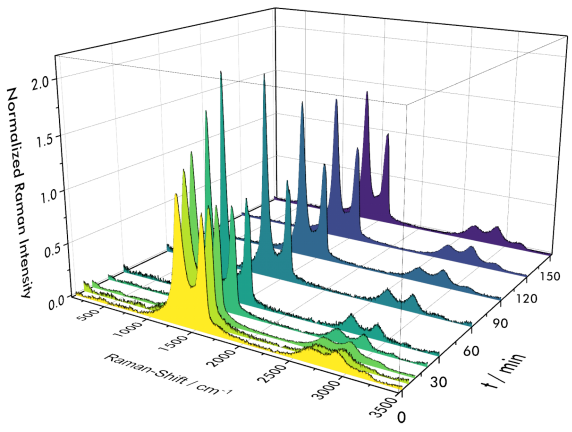

Fig. B7. Time-dependent Raman spectra, taken during the reduction of GO. The rising and then decreasing intensity ratio of D- to G-bands indicates a far-reaching reduction to rGO.

Tab. B1. Model hyperparameters, where no parameter value is given, scikit-learn or pytorch defaults were used.

Hyperparameter	**Baseline Model**	**CNN (classification)**	**CNN (regression)**
Data setup	*Scale*	-	
Mean setup	*Mean*	-	
Brightness	0.49	0.3	0.3
Estimators	265	-	
Criterion	*Entropy*	-	
Min samples split	0.013	-	
Min samples leaf	10	-	
Max features	$log2$	-	
Ccp alpha	0.015	-	
Bootstrap	*False*	-	
Class weight	-	-	
Max samples	-	-	
Ndim	-	3	3
Img size	-	480×260	800×680
Batch size	-	16	8
Learning rate	-	8.8×10^{-6}	1×10^{-5}
Weight decay	-	0.0063	0.0063
Model	-	*ResNeXt 50* $32 \times 4d$	*ConvNext*
Pretrained	-	*True*	*True*
# epochs	-	20	20

Tab. B2. Classification accuracies for different datasets and models. The standard deviation for the different accuracies was calculated on the validation folds. The tree models reach about 50% test accuracy while showing large variance in the validation sets, which indicates overfitting on the training set. The CNN model outperforms the tree-based models. The blank and masked accuracies refer to a prism without receptors and digitally masked receptors respectively. Both accuracies are expected to be low. The permuted accuracy is the model accuracy when experiment order is changed.

Model	**Accuracies / %**					
	Training	Validation	Test	Blank	Masked	Permuted
Tree model receptor ROIs	83 ± 1	68 ± 15	49 ± 4	-	-	-
Tree model gold ROIs	81 ± 2	67 ± 19	48 ± 7	-	-	-
CNN (water)	89 ± 1	85 ± 10	77 ± 6	32 ± 12	41 ± 10	76 ± 4
CNN (urine)	94 ± 2	69 ± 3	67 ± 3	-	-	-

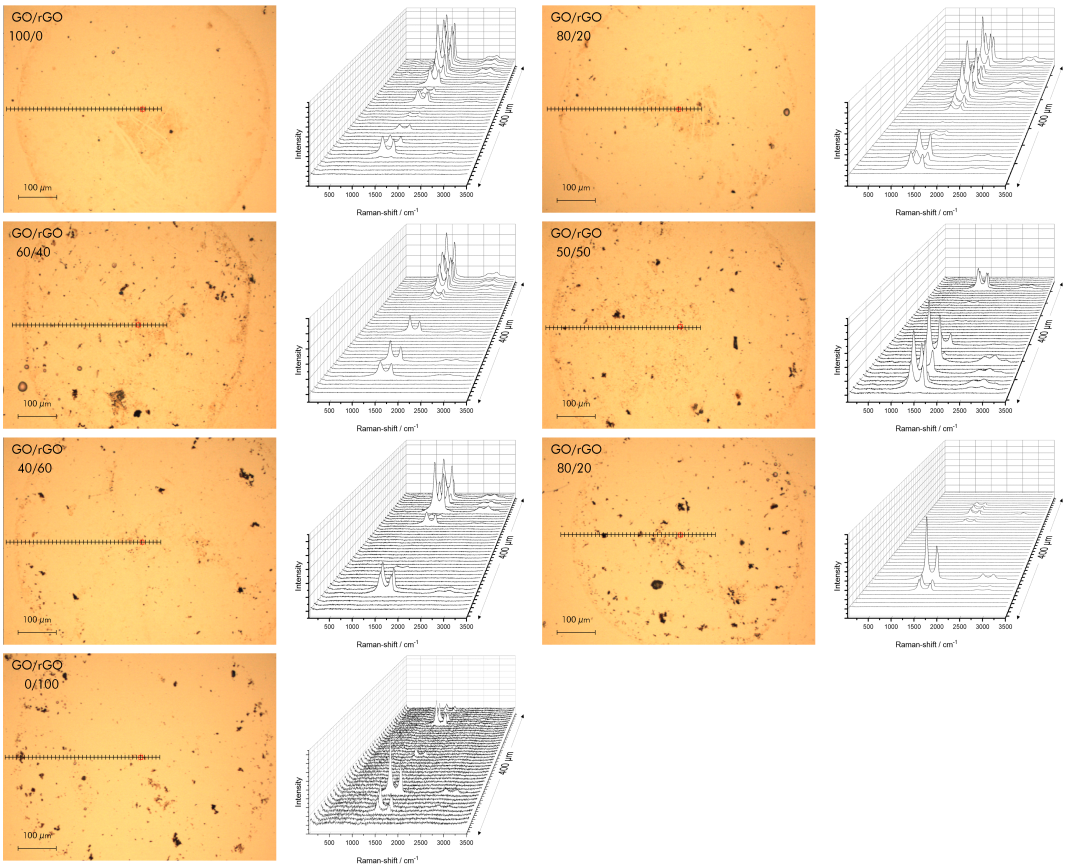

Fig. B8. Morphology of GO/rGO spots: microscopic images of individual spots with Raman spectra collected as line scans across 400 µm as indicated.

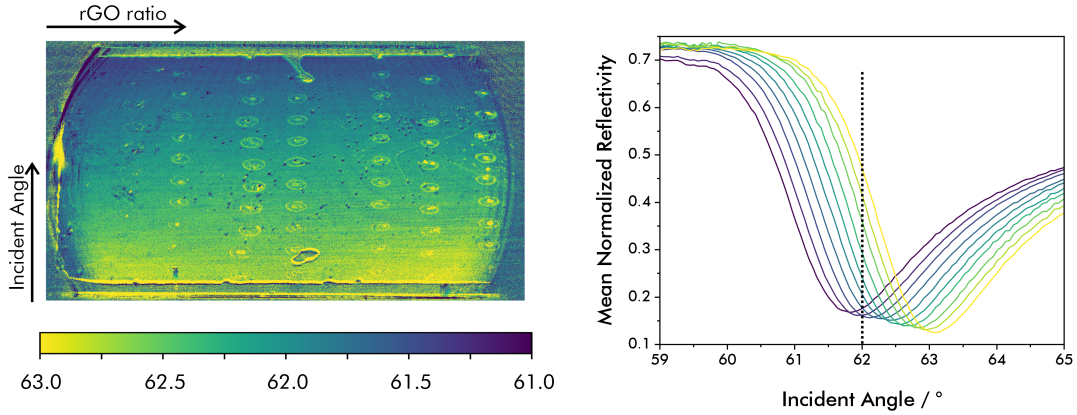

Fig. B9. (Left) Sensitivity map of the sensor surface, where the color represents the position of the maximum slope of the SPR curve for every pixel; The angle of incidence increases from top to bottom, causing a shift of the SPR curve towards different incident angles and measured intensities. (Right) SPR curves of different positions on the sensor surface, exemplary for one sensor. The curves are averaged over the length of the prism and normalized by their intensity in s-polarization. The dotted line shows the operating angle for the following measurements on this SPRi system.

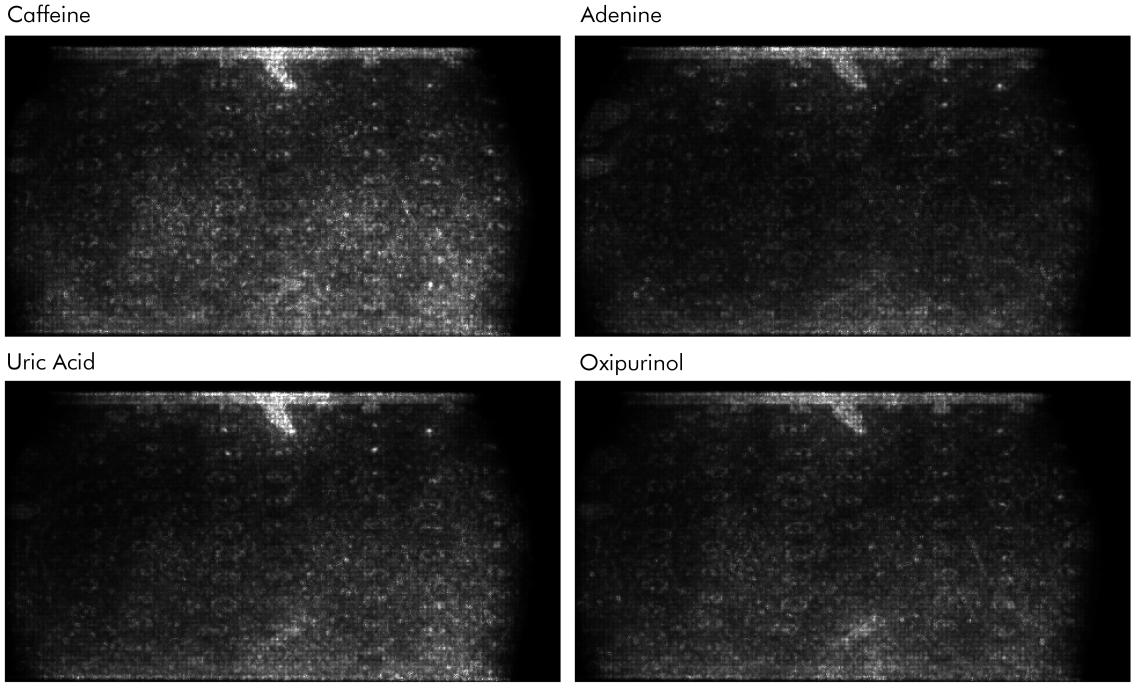

Fig. B10. Mean SHAP values for the test data as a measure for feature importance. The most important features are class-dependent, and the receptor spots are distinctly visible. High SHAP values aside of the receptor spots for the classification of caffeine indicate stronger matrix effects compared to other purines.

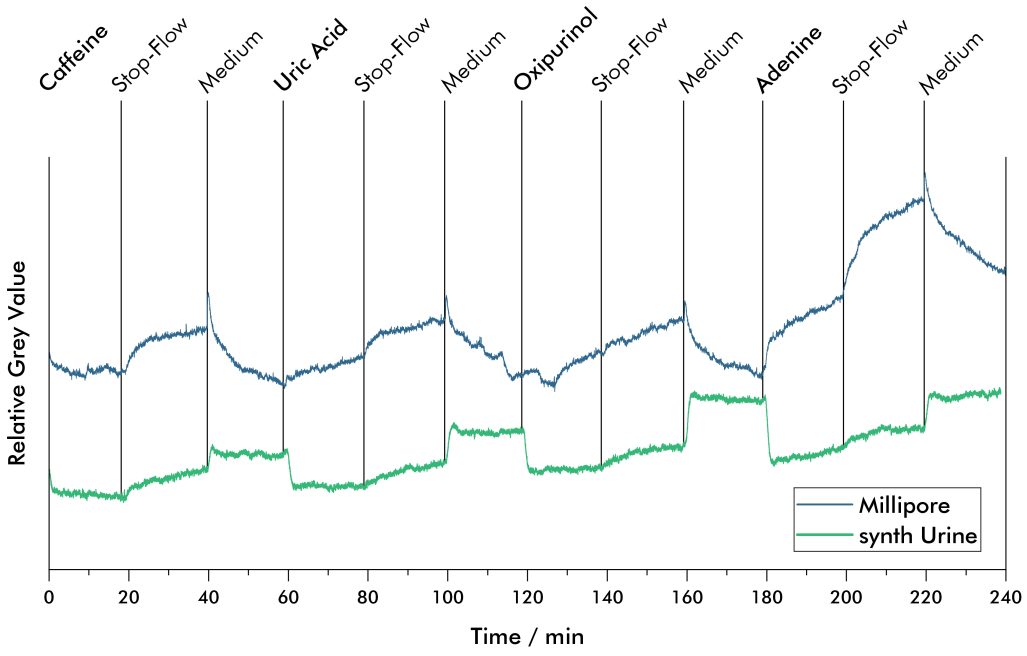

Fig. B11. Exemplary measurement curves used for purine classification in Millipore water and in synthetic urine. Urine samples are spiked with purine dissolved in Millipore, resulting in a slightly lower refractive index, visible as signal jumps before and after purge-steps with analyte free urine.

C Datasheets

C.1 CreaVac

Creavac - Creative Vakuumbeschichtung GmbH
Sporbitzer Ring 9

D - 01259 Dresden

Qualitätsprüf-Zertifikat DIN 55 350-18-4.2.1

Kunde **Ostbayrische Technische Hochschule Regensburg**
Technologie **NiCr-Au**

Bezeichnung

Produkt	Schichtsystem	Stück
Glasprismen montiert	NiCr 6 nm + Au 49 nm	**10**

Eingangskontrolle

erfolgte nach Ident-Prüfung DIN ISO 2859-1 Prüfniveau II auf folgende Merkmale: Verschmutzungen, Oberflächenfehler

Ausgangskontrolle **Lieferschein-Nr.** **23301171**

Prüfmethode	Prüfgerät
Schichtdickenbestimmung mittels Röntgenfluoreszenz	Fischerscope®XAN 250

Bemerkungen: Die Messung der Schichtdicke erfolgte auf den Substraten als 3-fach Bestimmung. Angegeben sind die jeweiligen Mittelwerte der Messungen.

gemessene Schichtdicken	NiCr	Au
Messposition 1	1,9	49,9
Messposition 2	2,56	47,9

Unterschrift QS

28.03.2023
Datum

Dieses Dokument wurde elektronisch erstellt und ist auch ohne Unterschrift gültig.

C.2 Schott Glass SF2

Data Sheet

SCHOTT

SF2
648339.386

n_d = 1.64769	ν_d = 33.85	$n_F - n_C$ = 0.019135
n_e = 1.65222	ν_e = 33.60	$n_{F'} - n_{C'}$ = 0.019412

Refractive Indices		
	λ [nm]	
$n_{2325.4}$	2325.4	1.61003
$n_{1970.1}$	1970.1	1.61494
$n_{1529.6}$	1529.6	1.62055
$n_{1060.0}$	1060.0	1.62766
n_t	1014.0	1.62861
n_s	852.1	1.63289
n_r	706.5	1.63902
n_C	656.3	1.64210
$n_{C'}$	643.8	1.64297
$n_{632.8}$	632.8	1.64379
n_D	589.3	1.64752
n_d	587.6	1.64769
n_e	546.1	1.65222
n_F	486.1	1.66123
$n_{F'}$	480.0	1.66238
n_g	435.8	1.67249
n_h	404.7	1.68233
n_i	365.0	1.70027
$n_{334.1}$	334.1	
$n_{312.6}$	312.6	
$n_{296.7}$	296.7	
$n_{280.4}$	280.4	
$n_{248.3}$	248.3	

Constants of Dispersion Formula	
B_1	1.40301821
B_2	0.231767504
B_3	0.939056586
C_1	0.01057954660
C_2	0.0493226978
C_3	112.4059550

Constants of Formula for dn/dT	
D_0	1.10E-06
D_1	1.75E-08
D_2	-1.29E-11
E_0	1.08E-06
E_1	1.03E-09
λ_{TK} [µm]	0.249

Internal Transmittance τ_i		
λ [nm]	τ_i [10mm]	τ_i [25mm]
2500	0.830	0.620
2325	0.870	0.710
1970	0.950	0.880
1530	0.994	0.985
1060	0.998	0.996
700	0.998	0.996
660	0.998	0.994
620	0.998	0.995
580	0.998	0.995
546	0.998	0.995
500	0.997	0.993
460	0.995	0.988
436	0.993	0.982
420	0.990	0.975
405	0.985	0.962
400	0.981	0.954
390	0.967	0.920
380	0.950	0.870
370	0.910	0.790
365	0.880	0.720
350	0.670	0.370
334	0.110	
320		
310		
300		
290		
280		
270		
260		
250		

Color Code	
λ_{80} / λ_5	37/33

(*= λ_{70}/λ_5)

Remarks
lead containing glass type

Relative Partial Dispersion	
$P_{s,t}$	0.2233
$P_{C,s}$	0.4813
$P_{d,C}$	0.2923
$P_{e,d}$	0.2367
$P_{g,F}$	0.5886
$P_{i,h}$	0.9376
$P'_{s,t}$	0.2201
$P'_{C',s}$	0.5196
$P'_{d,C'}$	0.2430
$P'_{e,d}$	0.2334
$P'_{g,F'}$	0.5209
$P'_{i,h}$	0.9242

Deviation of Relative Partial Dispersion ΔP from the normal line	
$\Delta P_{C,t}$	-0.0009
$\Delta P_{C,s}$	-0.0005
$\Delta P_{F,e}$	0.0004
$\Delta P_{g,F}$	0.0017
$\Delta P_{i,g}$	0.0112

Other Properties	
$\alpha_{-30/+70°C}$ [10^{-6}/K]	8.4
$\alpha_{+20/+300°C}$ [10^{-6}/K]	9.2
T_g [°C]	441
$T_{10^{13}}$ [°C]	428
$T_{10^{7.6}}$ [°C]	600
c_p [J/(g*K)]	0.498
λ [W/(m•K)]	0.735
ρ [g/cm³]	3.86
E [10^3 N/mm²]	55
µ	0.227
K [10^{-6} mm²/N]	2.62
$HK_{0.1/20}$	410
HG	2
CR	1
FR	0
SR	2
AR	2.3
PR	2

Temperature Coefficients of the Refractive Index						
	$\Delta n_{rel}/\Delta T$ [10^{-6}/K]			$\Delta n_{abs}/\Delta T$ [10^{-6}/K]		
[°C]	**1060.0**	**e**	**g**	**1060.0**	**e**	**g**
-40/-20	2.3	4.0	6.0	0.1	1.8	3.7
+20/+40	2.7	4.6	6.9	1.3	3.2	5.4
+60/+80	3.1	5.2	7.6	2.0	4.1	6.4

As of 01-Feb-2014 , subject to change

C.3 Camera Datasheet

SPECS	BFS-U3-63S4M-C	BFS-U3-63S4C-C
Resolution	3072 x 2048	
Frame Rate*	59.6 FPS	
Megapixels	6.3 MP	
Chroma	Mono	Color
Sensor	Sony IMX178, CMOS, 1/1.8"	
Readout Method	Rolling shutter with global reset	
Pixel Size	2.4 µm	
Lens Mount	C-mount	
ADC	10-bit / 14-bit	
Minimum Frame Rate**	1 FPS	
Gain Range**	0 to 47 dB	
Exposure Range**	8 µs to 30 s	
Acquisition Modes	Continuous, Single Frame, Multi Frame	
Partial Image Modes	Pixel binning, decimation, ROI	
Image Processing	Gamma, lookup table, and sharpness	Color correction matrix, gamma, lookup table, saturation, and sharpness
Sequencer	Up to 8 sets using 5 features, including image size	
Image Buffer	240 MB	
User Sets	2 user configuration sets for custom camera settings	
Flash Memory	6 MB non-volatile memory	
Opto-isolated I/O	1 input, 1 output	
Non-isolated I/O	1 bi-directional, 1 input	
Auxiliary Output	3.3 V, 120 mA maximum	
Interface	USB 3.1 Gen 1	
Power Requirements	8 - 24 V via GPIO or 5 V via USB3 interface	
Power Consumption	3 W maximum	
Dimensions/Mass	29 mm x 29 mm x 30 mm / 36 g	
Machine Vision Standard	USB3 Vision v1.0	
Compliance	CE, FCC, KCC, RoHS, REACH. The ECCN for this product is: EAR099.	
Temperature	Operating: 0°C to 50°C Storage: -30°C to 60°C	
Humidity	Operating: 20% to 80% (no condensation) Storage: 30% to 95% (no condensation)	
Warranty	3 years	

*Frame rates are measured with Device Link Throughput Limit of 380 MBps and Acquisition Frame Rate disabled.

**Values are the same in binning and no binning modes.

CANADA
12051 Riverside Way
Richmond, BC, Canada
V6W 1K7
T: +1 866.765.0827 (toll free)
T: +1 604.242.9937
F: +1 604.242.9938
E: mv-sales@flir.com

USA
T: +1 866.765.0827 (toll free)
E: mv-na-sales@flir.com

www.flir.com/mv

EUROPE
T: +49 7141 488817-0
F: +49 7141 488817-99
E: mv-eusales@flir.com

CHINA
T: +86 10 8215 9938
F: +86 10 8215 9936
E: mv-chinasales@flir.com

ASIA
E: mv-asiasales@flir.com

FLIR | The World's Sixth Sense®

www.flir.com
NASDAQ: FLIR

VN: BFS-U3-63S4-v3

FIND THE BEST BLACKFLY S FOR YOUR NEEDS

C.4 Objective Lens

Edmund optics | worldwide #67-715

Optical

Horizontal Field of View, 1/2" Sensor:	25.4mm - 14.5°
Horizontal Field of View, 2/3" Sensor:	35mm - 19.8°
Horizontal Field of View, 1/3" Sensor:	19mm - 10.9°
Maximum Image Circle (mm):	11.00
Numerical Aperture NA, Object Side:	0.0706
Horizontal Field of View @ Max Sensor Format:	36.5mm - 19.8°
Horizontal Field of View, 1/1.8" Sensor:	29.9mm - 16.2°
Horizontal Field of View, 1/2.5" Sensor:	24.0mm - 13.1°
Focal Length FL (mm):	25.00
Primary Magnification PMAG:	0.243
Maximum Sensor Format:	2/3"
Working Distance (mm):	100 - ∞
Aperture (f/#):	f/1.4 - f/16
Coating Specification:	425 - 1000nm BBAR
Entrance Pupil Position (mm):	17.14
Horizontal Field of View, 1/4" Sensor:	14.9mm - 8.2°
Object Space Principal Plane (mm):	18.74
Image Space Principal Plane (mm):	-12.43
Field of View at Max Sensor Format:	Horizontal: 36.6mm - 19.8° Vertical: 27.4mm - 14.9° Diagonal: 45.9mm - 24.6°
Maximum Distortion (%):	0.22
Exit Pupil Position (mm):	-14.14
Lens Wavelength Range:	VIS-NIR

Mechanical

Iris Option:	Variable
Length (mm):	30.50
Filter Thread:	M25.5 x 0.50 (Female)
Maximum Diameter (mm):	31
Weight (g):	48
Maximum Rear Protrusion (mm):	1.39
Number of Elements (Groups):	7 (6)
Mount:	C-Mount

General

Type:	Fixed Focal Length Lens

C.5 OSRAM LED

LZ1-00R302
DATASHEET

OSRAM

Relative Spectral Emission [4)]

$I_{rel} = f(\lambda)$; I_F = 1000 mA; T_C = 25 °C

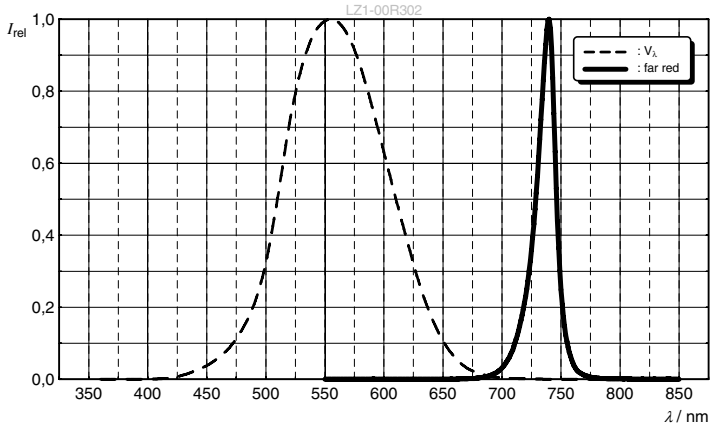

Radiation Characteristics [4)]

$I_{rel} = f(\phi)$; T_C = 25 °C

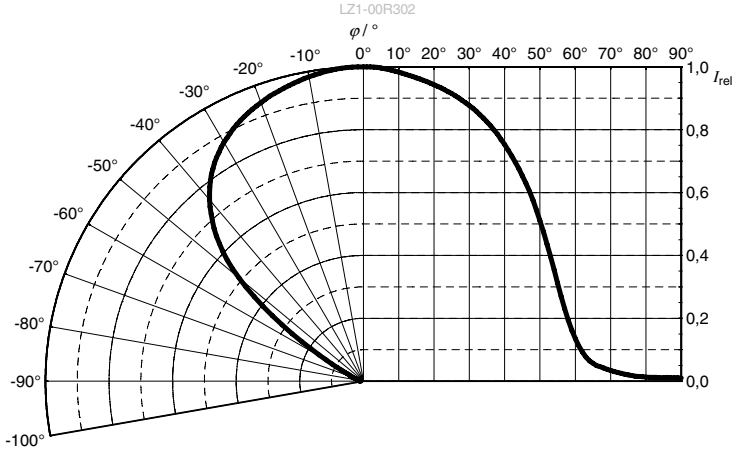

Forward current [4)]

$I_F = f(V_F)$; T_C = 25 °C

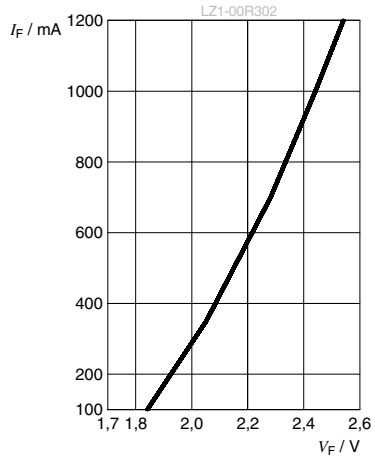

Relative Radiant Power [4), 7)]

$\Phi_E/\Phi_E(1000\ mA) = f(I_F)$; T_C = 25 °C

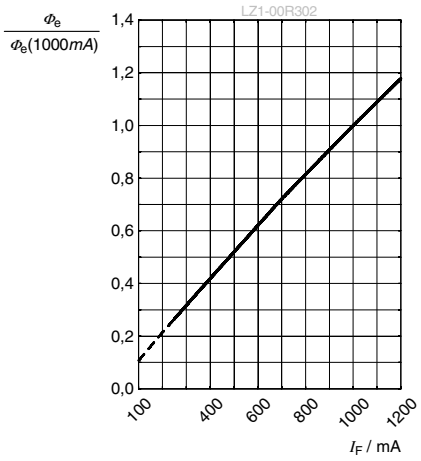

Peak Wavelength [4)]

$\Delta\lambda_{peak} = f(I_F)$; T_C = 25 °C

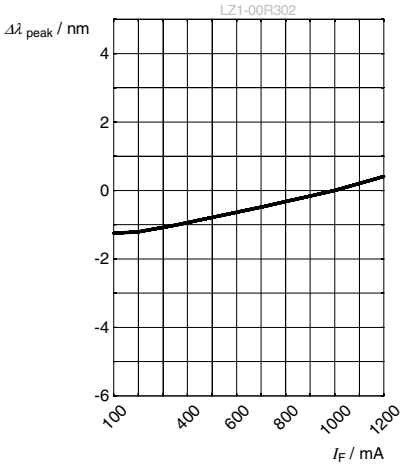

References

[1] M. Born, E. Wolf, *Principles of Optics: Electromagnetic Theory of Propagation, Interference and Diffraction of Light*, 6th corr. ed, Pergamon, Oxford New York Beijing [etc.], **1980** (cit. on p. 108).

[2] M. Cardona, "Fresnel Reflection and Surface Plasmons", *American Journal of Physics* **1971**, *39*, 1277–1277, DOI 10.1119/1.1976627 (cit. on p. 108).

[3] E. Hecht, *Optics*, 5 ed/fifth edition, global edition, Pearson, Boston Columbus Indianapolis New York San Francisco Amsterdam Cape Town Dubai London Madrid Milan Munich, **2017** (cit. on p. 109).

[4] William Riley, David Howe, "Handbook of Frequency Stability Analysis", **2008**, (Ed.: Special Publication (NIST SP), National Institute of Standards and Technology, Gaithersburg, MD) (cit. on p. 111).

[5] L. Wunderlich, P. Hausler, S. Märkl, R. Bierl, T. Hirsch, "Nanoparticle Determination in Water by LED-Excited Surface Plasmon Resonance Imaging", *Chemosensors* **2021**, *9*, 175, DOI 10.3390/chemosensors9070175 (cit. on p. 115).

Erklärung

Ich erkläre hiermit an Eides statt, dass ich die vorliegende Arbeit ohne unzulässige Hilfe Dritter und ohne Benutzung anderer als der angegebenen Hilfsmittel angefertigt habe; die aus anderen Quellen direkt oder indirekt übernommenen Daten und Konzepte sind unter Angabe des Literaturzitats gekennzeichnet.

Andere Personen waren an der inhaltlich-materiellen Herstellung der vorliegenden Arbeit nicht beteiligt. Insbesondere habe ich hierfür nicht die entgeltliche Hilfe eines Promotionsberaters oder anderer Personen in Anspruch genommen. Niemand hat von mir weder unmittelbar noch mittelbar geldwerte Leistungen für Arbeiten erhalten, die im Zusammenhang mit dem Inhalt der vorgelegten Dissertation stehen.

Die Arbeit wurde bisher weder im Inland noch im Ausland in gleicher oder ähnlicher Form einer anderen Prüfungsbehörde vorgelegt.

Regensburg, Simon Jobst